Master Thesis

Design and Analysis of a MEMS Comb Vibratory Gyroscope

Presented to the
Faculty of University of Bridgeport
In Partial Fulfillment of the Requirements
For the Degree of

MASTER OF SCIENCE

In the Department of Electrical Engineering

By

Haifeng Dong
(Student ID: 0732752)

B.S.(ECE), Tongji University, Shanghai, China, June, 2005

04/2009
Thesis Advisor: Dr. Xingguo Xiong
University of Bridgeport, Bridgeport, CT 06604

UNIVERSITY OF BRIDGEPORT

DESIGN AND ANALYSIS OF A MEMS COMB VIBRATORY GYROSCOPE

APPROVED BY
SUPERVISING COMMITTEE:

Supervisor: ______________________
(Xingguo Xiong)

____
(Lawrence Hmurcik)

____
(Linfeng Zhang)

ACKNOWLEDGMENTS

After three years of graduate study, I have learned one thing – I could never have done any of this thesis, without the support and encouragement of a lot of people.

First, I would like to thank my advisor, Dr. Xingguo Xiong. You have been my mentor, but also my friend. You have given so much of yourself to help me succeed. If I do take the academic path, I only hope that I can be half the advisor that you have been to me. Whatever path I do take, I will be prepared because of you.

I would also like to thank the rest of my thesis committee for their support. Dr. Lawrence Hmurcik and Dr. Linfeng Zhang have provided me with invaluable advice and comments on my study and research.

Last but most, I would like to dedicate this work to my family: my farther and my mother. Without your unending support and love from childhood to now, I never would have made it through this process or any of the tough times in my life. Thank you.

ABSTRACT

MEMS (Micro-electro-mechanical Systems) refer to devices or systems integrated with electrical and mechanical components in the scale of microns. Due to its small size, low cost, low power consumption and high efficiency, MEMS technology has been widely used in many fields.

In this research, a novel comb-driving, differential capacitance sensing MEMS vibratory gyroscope based on glass-silicon-glass structure is proposed. The gyroscope is activated to vibrate along X axis by electrostatic comb driving. If an angular velocity along Y axis is experienced, the Coriolis force activates the sensing vibration of the central mass along Z axis. The size of the driving beams and sensing beams are carefully chosen to reduce the frequency mismatch in two directions, thus increasing the gyroscope sensitivity. The device is packaged in a vacuum state to achieve high quality factors.

First, an introduction to MEMS devices and systems, as well as their applications are introduced in Chapter I. Background information regarding the traditional gyroscope, Coriolis effect and several products available in MEMS gyroscope market is given in Chapter II. Design issues of MEMS gyroscopes are discussed in Chapter III, including driving schemes, sensing schemes, resonant frequency, forced vibration and air damping effect. A novel gyroscope design with its dynamic analysis is proposed in Chapter IV based on the study of previous research. In Chapter V, performance of the novel gyroscope is given and ANSYS simulation is used to verify the theoretical calculation results. Fabrication process of this gyroscope is discussed in Chapter VI. Lastly, Conclusions are given in Chapter VII.

From dynamic analysis, this MEMS gyroscope is expected to have a displacement sensitivity of 105.9nm/(º/sec) and a capacitance sensitivity of 13.88fF/(º/sec). It can be very attractive because of its high sensitivity and ease for fabrication. It has a potential use for inertial navigation in many applications, such as automobile, aerospaceship, microsatellite, consumer products, etc.

TABLE OF CONTENTS

LIST OF TABLES

LIST OF FIGURES

CHAPTER I. INTRODUCTION

1.1 What Is MEMS?

MEMS, the acronym of "Micro-Electro-Mechanical Systems", is generally considered as devices and systems integrated with mechanical elements, sensors, actuators, and electronic circuits on a common silicon substrate through microfabrication technology. MEMS are made up of components between 1 to 1000 micrometers in size (i.e. 0.001 to 1 mm) and MEMS devices generally range in size from several micrometers (one millionths of a meter) to several millimeters. They usually consist of a central unit that processes data, the microprocessor and several components that interact with the outside such as microsensors and microactuators.

The technology of MEMS has been developed in the past decades, especially in the last twenty years. In the beginning of 1990s, MEMS emerged with the aid of the development of integrated circuit (IC) fabrication processes, in which sensors, actuators, and control functions are cofabricated in silicon. Since then, remarkable research progresses have been achieved in MEMS under the strong capital promotions from both government and industries. As of the end of 1990s, in addition to the commercialization of some less integrated MEMS devices, such as microaccelerometers, inkjet printer head, micromirrors for projection, etc., the concepts and feasibility of more complex MEMS devices have been proposed and demonstrated for the applications in such varied fields as microfluidics, aerospace, biomedical, chemical analysis, wireless communications, data storage, display, optics, etc. Many manufacturing techniques emerged along with this evolution. MEMS devices with various sensing or actuating mechanisms are fabricated using silicon bulk micromachining, surface micromachining, and lithography, galvanoforming, molding (LIGA) processes.

(a) (b)

Figure 1.1 MEMS systems and devices. (a) A digital propulsion microthruster on a penny to demonstrate how small MEMS systems are. (source http://eed.gsfc.nasa.gov/562/SA_MEMs.htm) (b) An ant having a look at some MEMS devices. (source http:// mems.ie.ntnu.edu.tw/main.htm)

Nowadays, MEMS becomes an interdisciplinary field of study, with the following features:

- It is a portfolio of techniques and processes to design and create miniature systems.
- It is a physical product often specialized and unique to a final application − one can seldom buy a generic MEMS product at the neighborhood electronics store.
- It merges the functions of sensing and actuation with computation and communication to locally control physical parameters at the microscale, yet cause effects at much grander scales.

Because MEMS devices are manufactured using batch fabrication techniques similar to those used for integrated circuits, unprecedented levels of functionality, reliability, and sophistication can be placed on a small silicon chip at a relatively low cost. Due to these benefits, MEMS technology has been widely used in many industry fields.

1.2 MEMS Applications

MEMS promises to revolutionize nearly every product category by bringing together silicon-based microelectronics with micromachining technology, making possible the realization of complete systems-on-a-chip. MEMS is an enabling technology allowing the development of smart products, augmenting the computational ability of microelectronics with the perception and control capabilities of microsensors and microactuators and expanding the space of possible designs and applications. Commercial applications include:

- Inkjet printers, which use piezoelectrics or thermal bubble ejection to deposit ink on paper.
- Accelerometers in modern cars for a large number of purposes including airbag deployment in collisions.
- Accelerometers in consumer electronics devices such as game controllers (Nintendo Wii), personal media players, cell phones (Apple iPhone) and a number of Digital Cameras (various Canon Digital IXUS models). Also used in PCs to park the hard disk head when free-fall is detected, to prevent damage and data loss.
- MEMS gyroscopes used in modern cars and other applications to detect yaw; e.g. to deploy a roll over bar or trigger dynamic stability control.
- Silicon pressure sensors e.g. car tire pressure sensors, and disposable blood pressure sensors.
- Displays e.g. the DMD (Digital Micromirror Device) chip in a projector based on DLP (Digital Light Processing) technology has on its surface several hundred thousand micromirrors.

- Optical switching technology which is used for switching technology and alignment for data communications.

- BioMEMS applications in medical and health related technologies from Lab-On-Chip to Micro-Total-Analysis (biosensor, chemosensor).

- Interferometric modulator display (IMOD) applications in consumer electronics (primarily displays for mobile devices). Used to create interferometric modulation − reflective display technology as found in mirasol displays.

1.2.1 MEMS in Inertial Sensing

Inertial Sensors, such as accelerometers and gyroscopes, are widely used in many applications in the aerospace, military, automotive and marine industries. In the aerospace industry, these devices are used in the basic flight stabilization of aircraft and rockets as well as in navigation. Military applications include the same usages in air to air missiles, air to ground missiles, ground to air missiles, ground to ground missiles, barrage rounds and hypersonic projectiles. Automotive applications include vehicle stability systems and rollover prevention systems. Naval and marine applications include ship stabilization and navigation.

As inertial sensors shrink in size and cost, the number of applications increases exponentially. As the accuracy and stability of these miniatures, low-cost devices increases, higher performance systems are being introduced into lower cost items and consumer goods such as automobiles, thereby enhancing safety and functionality.

Accelerometers are the stars of the MEMS show, with millions bought each year by the automotive industry. Devices with integral electronics offer readout electronics and self-test capability, and cost far less than accelerometers of decades ago. The physical mechanisms underlying MEMS accelerometers include capacitive, piezoresistive, electromagnetic, piezoelectric, ferroelectric, optical, and tunneling. The most successful types are based on capacitive transduction; the reasons are the simplicity of the sensor element itself, no requirement for exotic materials, low power consumption, and good stability over temperature. Although many capacitive transducers have a nonlinear capacitance vs. displacement characteristic, feedback is commonly used to convert the signal to a linear output. The output can be analog, digital, ratiometric to the supply voltage, or any of various types of pulse modulation. Sensors with digital output are convenient when the data must be transmitted without further noise degradation.

Analog Devices, Inc. manufactures a family of surface micromachined accelerometers with polysilicon as the structural and proof mass elements. A comb-like structure suspended from springs forms the inertial mass. Displacements of the mass are measured capacitively with respect to two sets of stationary finger-like electrodes. The 2-micron-thick polysilicon layer is deposited on a sacrificial layer of SiO2 that is removed in a final release step with hydrofluoric acid. One advantage of this technique is that it can be combined with a CMOS or BiMOS process, allowing the entire system (electronics plus sensor) to be inexpensively integrated on one chip. The ADXL50 (see Figure 1.2 and 1.3), a low-cost, low-power (2 µA per axis), 2-axis accelerometer with a range of ±2 g, can measure both dynamic (vibration) and static acceleration (gravity). The outputs are duty cycle modulated signals, with duty cycles proportional to the acceleration in each of the two sensitive axes.

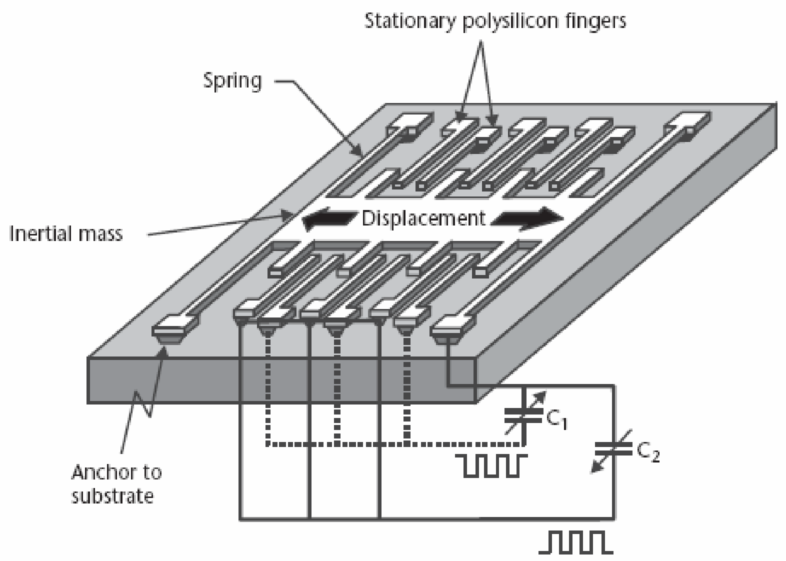

Figure 1.2 Illustration of the basic structure of the ADXL family of surface micromachined accelerometers

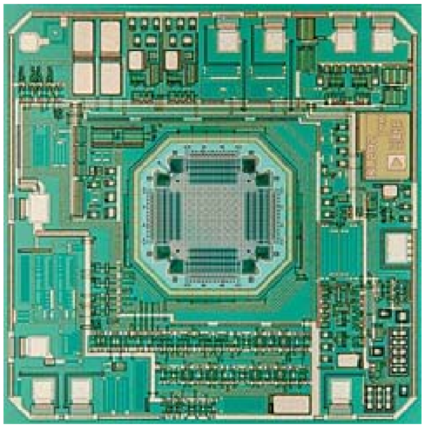

Figure 1.3 Analog Devices ADXL 50 accelerometer. The electronics occupy the majority of the 3 mm 2 chip area. The 2-axis device is not only extremely small, but also modest in power requirements and can measure both static and dynamic acceleration.

Gyroscopes are another category that represents MEMS inertial sensors. Conventional (nonMEMS) spinning wheel gyros are common, but levitation and rotation of a MEMS device with no springs has not yet been commercialized. Many types of MEMS gyroscopes have appeared in the literature, with most falling into the categories of tuning-fork gyroscopes, oscillating wheels, Foucault pendulums, and wine glass resonators.

Tuning fork gyroscopes contain a pair of masses that are driven to oscillate with equal amplitude but in opposite directions. When rotated, the Coriolis force creates an orthogonal vibration that can be sensed by a variety of mechanisms. The gyroscope shown in Figure 1.4 and 1.5 uses comb-type structures to drive the tuning fork into resonance.

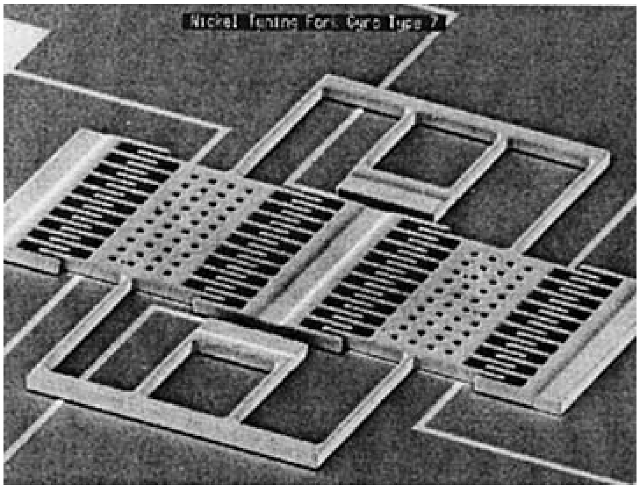

Figure 1.4 SEM (Scanning Electron Microscope) image of a comb drive tuning fork gyroscope designed by Draper Lab in Cambridge, MA

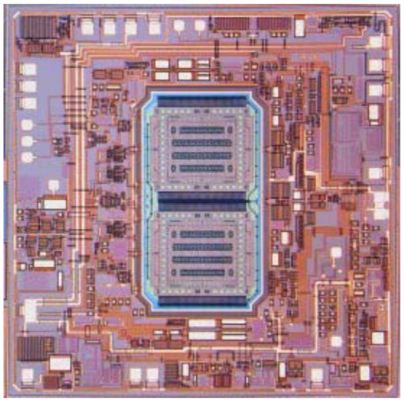

Figure 1.5 Analog Devices iMEMS ADXRS gyroscope. It integrates an angular rate sensor and signal processing electronics onto a single piece of silicon.

Many reports of vibrating-wheel gyros also have been published. In this type of gyro, the wheel is driven to vibrate about its axis of symmetry, and rotation about either in-plane axis results in the wheel's tilting, a change that can be detected with capacitive electrodes under the wheel. It is possible to sense two axes of rotation with a single vibrating wheel. A surface micromachined polysilicon vibrating wheel gyroscope is shown Figure 1.6. The potential for combining the mechanical resonator and sense and drive electronics on a single chip permits extreme miniaturization.

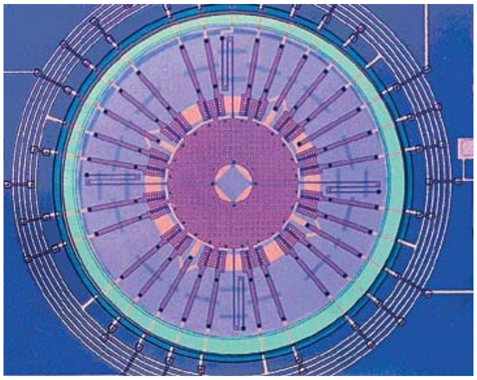

Figure 1.6 The vibrating wheel gyroscope designed at the U.C. Berkeley Sensors and Actuators Center

1.2.2 MEMS in Optical Application

Two notable optical applications which have benefited greatly from MEMS are displays and optical fiber communications. In displays, the Digital Light Processing (DLP) technology from Texas Instruments of Dallas, Texas, has become a standard in small- and large-screen projection of digital images, with the Digital Mirror Device (DMD) at its core. In fiber optical communications, there are a myriad of MEMS-based components in tunable lasers, optical switches, and optical attenuators, all key elements in transmitting data through optical fibers.

The DMD consists of a two-dimensional array of optical switching elements (pixels) on a silicon substrate (see Figure 1.7 and 1.8). Each pixel consists of a reflective micro-mirror supported from a central post. This post is mounted on a lower metal platform - the yoke - itself suspended by thin and compliant torsional hinges from two stationary posts anchored directly to the substrate. Two electrodes positioned underneath the yoke provide electrostatic actuation. A 24-V bias voltage between one of the electrodes and the yoke tilts the mirror towards that electrode. The nonlinear electrostatic and restoring mechanical forces make it impossible to accurately control the tilt angle. Instead, the yoke snaps into a fully deflected position, touching a landing site biased at the same potential to prevent electrical shorting. The angle of tilt is limited by geometry to ±10º (the direction of the sign is defined by the optics). The restoring torque of the hinges returns the micromirror to its initial state once the applied voltage is removed. CMOS static random-access memory (SRAM) cells fabricated underneath the micromirror array control the individual actuation states of each pixel and their duration. The OFF state of the memory cell tilts the mirror by –10º, whereas the ON state tilts it by +10º. In the ON state, off-axis illumination reflects from the micromirror into the pupil of the projection lens, causing this particular pixel to appear bright. In the other two tilt states (0º and –10º), an aperture blocks the reflected light giving the pixel a dark appearance. This beam-steering approach provides high contrast between the bright and dark states.

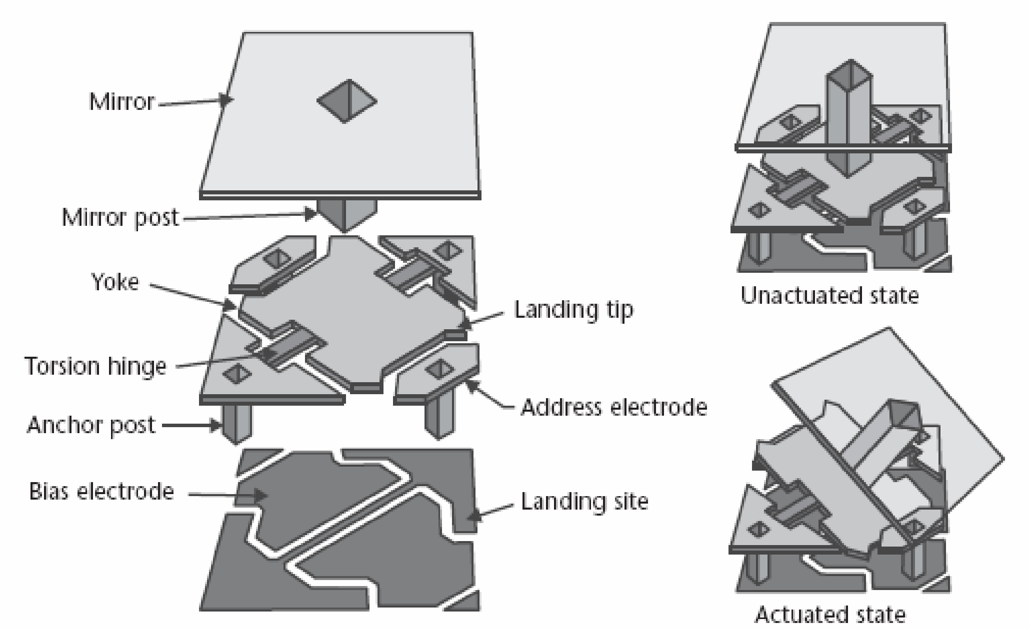

Figure 1.7 Illustration of a single DMD pixel by Texas Instruments of Dallas, Texas

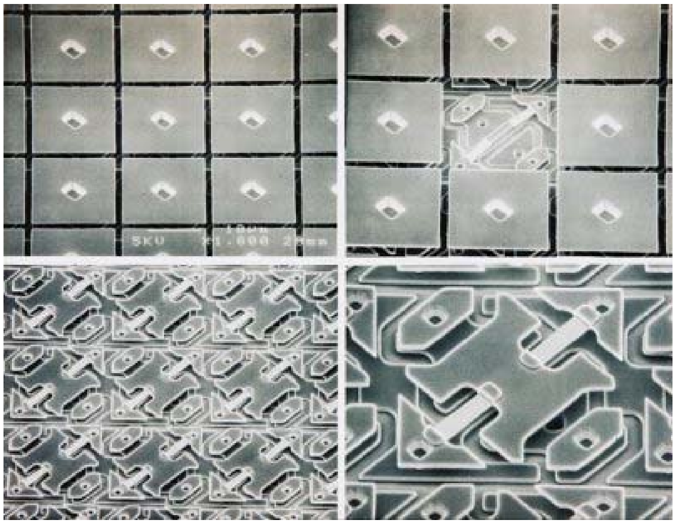

Figure 1.8 SEM photos of DMD units by Texas Instruments of Dallas, Texas

An optical switch to fiber-optical telecommunications and light transmission is like an electrical switch to electronic or microwave signaling. An optical switch redirects an incoming light signal into one of many output fibers. Arrays of optical switches allow the rapid reconfiguration of optical networks in data communications by altering the light path in a system of intersecting fibers. They are also useful components in the addition and deletion of extra channels in optical add/drop multiplexers for WDM (Wavelength-Division Multiplexing).

Figure 1.9 is a 2×2 binary reflective optical switch fabricated using SOI (Silicon On Insulator) wafers and DRIE (Deep Reactive-Ion Etching). An electrostatic comb actuator controls the position of a micromirror. In the cross state, light from an input fiber is deflected by 90º. In the bar state, the light from that fiber travels unobstructed through the switch. Side schematics illustrate the signal path for each state.

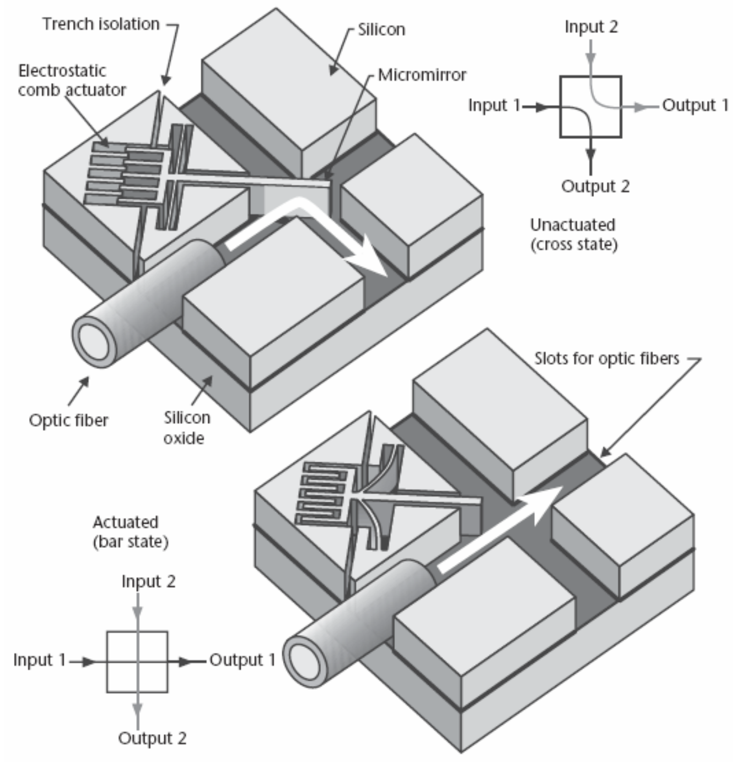

Figure 1.9 Illustration of a 2×2 binary reflective optical switch

Optical switches are commercially available today from such companies as JDS Uniphase of San Jose, California; DiCon Fiberoptics, Inc., of Berkeley, California; and Sercalo Microtechnology, Ltd., of Liechtenstein but are typically 1×2 up to 1×8, or they are 2×2 switches.

1.2.3 MEMS in RF Communication

RF (Radio Frequency) MEMS encompasses several distinct types of devices, including RF switches and relays, resonators, varactors (variable capacitors) and inductors. Applications of RF MEMS include all types of wireless communications, radar, satellites, military radio, instrumentation and test equipment. Compared to conventional RF components, RF MEMS offer significant benefits, including lower power consumption, lower insertion loss, lower cost and smaller form factor. RF MEMS have come to market more recently than other types of MEMS, but the RF MEMS is now growing rapidly.

Most MEMS capacitor implementations have in common a bottom plate residing on an insulated substrate, an air gap, and a flat top plate parallel to the substrate suspended by a spring structure (see Figure 1.10(a)). MEMS inductors are readily fabricated on integrated-circuit chips using standard CMOS or bipolar processes by simply forming a spiral in one layer of metal and a connection to the center of the spiral in another layer of metal (see Figure 1.10(b)). One of the earliest MEMS resonator designs, which is now commonly used in various MEM devices, is the interdigitated-finger comb-drive resonator structure (see Figure 1.10(c)). The most common MEMS switches are electrostatically driven switches which have a membrane or a cantilever containing one contact, which is suspended over the substrate supporting another contact (see Figure 1.10(d)).

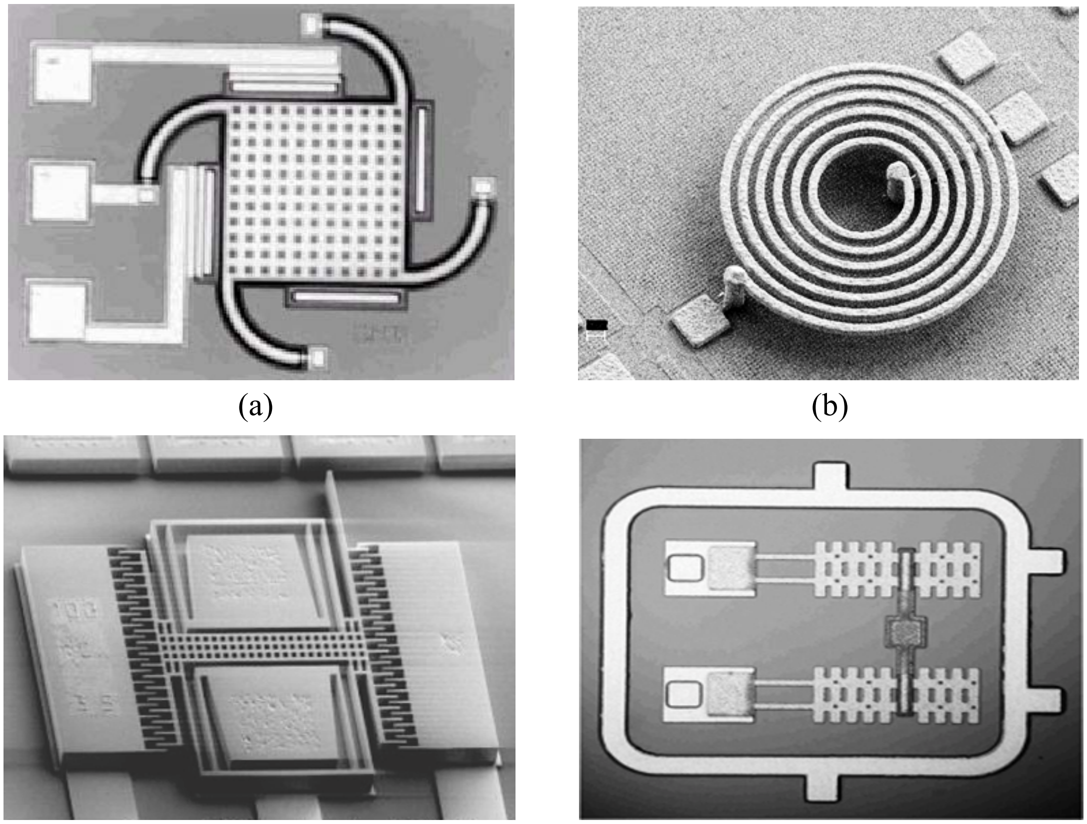
(a) (b)

(c) (d)

Figure 1.10 MEMS application in RF communication. (a) A MEM capacitor. (b) A MEMS inductor. (c) A MEMS resonator. (d) A MEMS switch.

1.2.4 MEMS in Life Science

MEMS is being applied to biomedical applications and life science research, becoming a new field of research unto itself, known as BioMEMS. It is an enabling technology for ever-greater functionality and cost reduction in smaller devices for improved medical diagnostics and therapies.

Today, dozens of companies are involved in biochemical analysis at the microscale, with a concentration of them involved in genomics, proteomics, and pharmacogenics. Their successes have already had a positive impact on the health of the population; examples include faster analysis of pathogens responsible for illness and of agricultural products as well as more rapid sequencing of the human genome. Systems expected in the near future will detect airborne pathogens responsible for illness (such as Legionnaire's disease or anthrax in a terrorist attack) with a portable unit, give on-demand genetic diagnostics for the selection of drug therapies, be able to test for food pathogens such as E. coli on site, and more rapidly test for bloodborne pathogens.

A very popular subset of BioMEMS devices is called Lab-on-a-chip (LOC). This technology utilizes a network of channels and wells that are etched onto glass or polymer chips to build minilabs. Pressure or electro-kinetic forces move pico liter volumes in finely controlled manner through the channels. Lab-on-a-chip enables sample handling, mixing, dilution, electrophoresis and chromatographic separation, staining and detection on single integrated systems. The main advantages of Lab-on-a-chip are ease-of-use, speed of analysis, low sample and reagent consumption and high reproducibility due to standardization and automation.

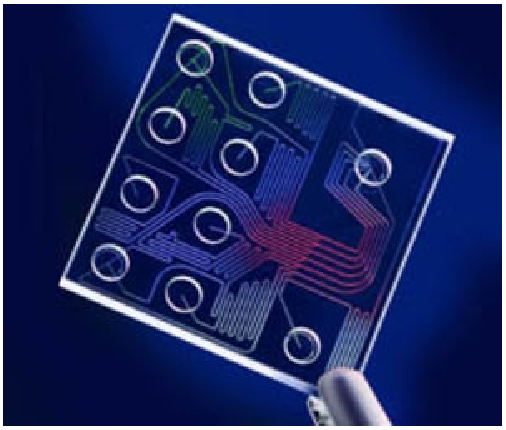

Figure 1.11 A Lab-on-a-chip for microfluidics

1.3 MEMS Market

Companies with strong MEMS programs come in many sizes. The larger firms specialize in manufacturing high volume inexpensive components or packaged solutions for end markets such as automobiles, biomedical, and electronics. The successful small firms provide value in innovative solutions and absorb the expense of custom fabrication with high sales margins. In addition, both large and small companies work in R&D to explore MEMS technology. A number of companies are already marketing MEMS devices and systems for commercial use. These companies include a broad range of manufacturers of sensors, industrial and residential control systems, electronic components, automotive and aerospace electronics, analytic instruments, and biomedical products.

According to IEEE (Institute of Electrical and Electronics Engineers) Spectrum [1], MEMS global market grew from $3.9–billion in 2002 to $8.3-billion in 2007 as shown in Table 1.1. That tells us that the MEMS technology is growing very rapidly. From Table 1.2, we can see that majority of MEMS production facilities are settled in North America, Europe and Japan.

Table 1.1 Growth of the world MEMS market (in million of U.S. dollars)

Product	***2002***	***2007***
	($000,000)	($000,000)
Microfluidics	1,404	2,241
Optical MEMS	702	1,126
RF MEMS	39	249
Other actuators	117	415
Inertial sensors	819	1,126
Pressure sensors	546	913
Other sensors	273	830
Total	**3,900**	**8,300**

Table 1.2 Geographical distribution of the world MEMS production facilities

Region	***Number of Fabs***
North America	139
Germany	34
France	20
United Kingdom	14
Benelux	17
Scandinavia	20
Switzerland	14
Rest of Europe	10
Japan	41
Rest of Asia	31

According to iSuppli [2], MEMS are making major inroads in the consumer- and mobile-electronics worlds. As a result, shipment of MEMS for consumer and mobile electronics is expected to grow from $1.1 billion (2006) to $2.6 billion (2012). STMicroelectronics ranked first in the global consumer/mobile MEMS market in 2008. Texas Instruments, which was first, now ranks second. In 2008, STMicroelectronics more than doubled its revenue from accelerometers, gyroscopes and pressure sensors for consumer and mobile applications, exceeding $200 million in 2008. Other MEMS suppliers include Epson Toyocom, which experienced an 75% increase in MEMS sales due to its new-generation gyroscope for gaming and navigation applications. Bosch Sensortec's revenue exploded by 167.3% in 2008, driven by strong sales in mobile handsets. Kionix, whose sales grew by 29.9% in 2008, has now expanded to 120 employees. Finally, startup Invensense only began shipping its MEMS products in 2007 and already exceeded $40 million in revenue in 2008.

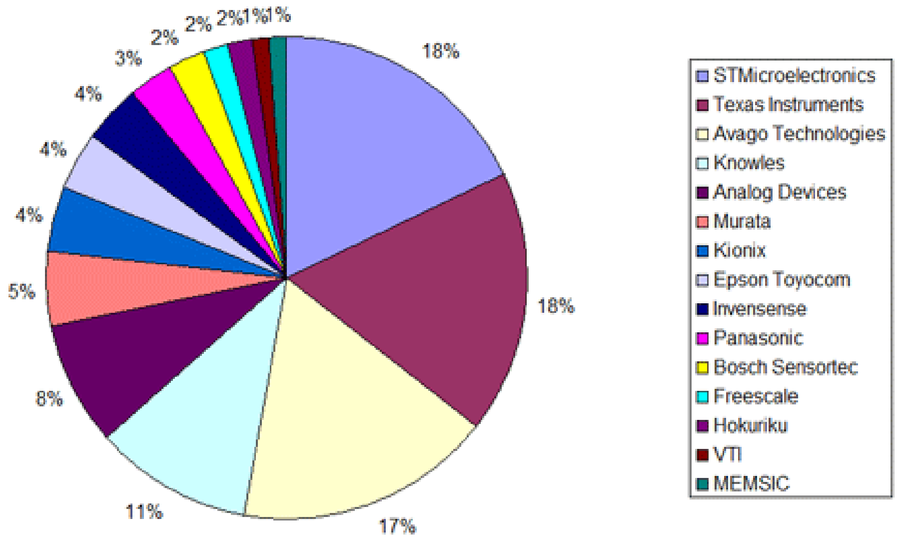

Figure 1.12 Global market share suppliers of MEMS for consumer and mobile applications

Based on iSuppli's analysis, the following three fields of MEMS industry are expected to have promising profit:

- Consumer Electronics Devices: Shipment revenue for MEMS in consumer electronics devices will increase to $1.1 billion in 2012, up from $699.9 million in 2006. Products in this segment consist of game controllers, digital still cameras, camcorders, MP3 players, personal navigation devices, remote controllers, rear-projection televisions, mini stand alone projectors, sports equipment, white goods, toys, headsets, and USB sticks.

- Mobile Handsets: Suppli predicts mobile handsets will remain the market's main driver until 2012, not only for accelerometers but also for other devices like Radio Frequency (RF) MEMS filters, actuators for zoom and autofocus, radio frequency MEMS switches, pressure sensors, gyroscopes, and pico projectors. Global revenue from shipments of all types of MEMS for mobile handsets and smart phones will increase to $1.3 billion by the end of 2012, rising at a Compound Annual Growth Rate (CAGR) of 34.4% from $296.8 million in 2007.

- Notebooks: Looking at another type of popular product, notebook PCs, MEMS accelerometers are increasingly being employed to detect freefall and quickly park the heads of the Hard Disk Drive (HDD) to protect it from damage. Until this year, such systems mainly were used in professional notebooks. However, the system is being employed in consumer systems starting in 2009. iSuppli predicts the market for notebook PC MEMS — also including microphones and pressure sensors — will rise to $185.9 million in 2012, up from $37.6 million in 2006.

While estimates for MEMS markets vary considerably, they all show significant present and future growth, reaching total volumes in the many billions of dollars by 2010. The expected growth stems from technical innovations and acceptance of the technology by an increasing number of end users and customers and especially after taking into the consideration that MEMS technology emphasis in the next few years on the "systems" not only the components and subsystems.

According to I-Micronews [3], they have done a MEMS market analysis the units forecasts, applications and growth rate levels. This has revealed interesting facts besides the only growth of the MEMS market global value. The MEMS 2007-2012 market forecast expects almost a US$14B market value by 2012 (at the chip level). This means the MEMS market is expected to double from the 2007 market value of US$7.1B. It represents a CAGR (Compound Annual Growth Rate) of 14% for the 2007-2012 period. The 2007-2010 growth will be however quite modest (11%) but a strong growth is expected after 2010. The year 2007 was indeed the time when new MEMS devices are hitting the market: auto-focus, oscillators and dual-axis gyroscopes to name a few.

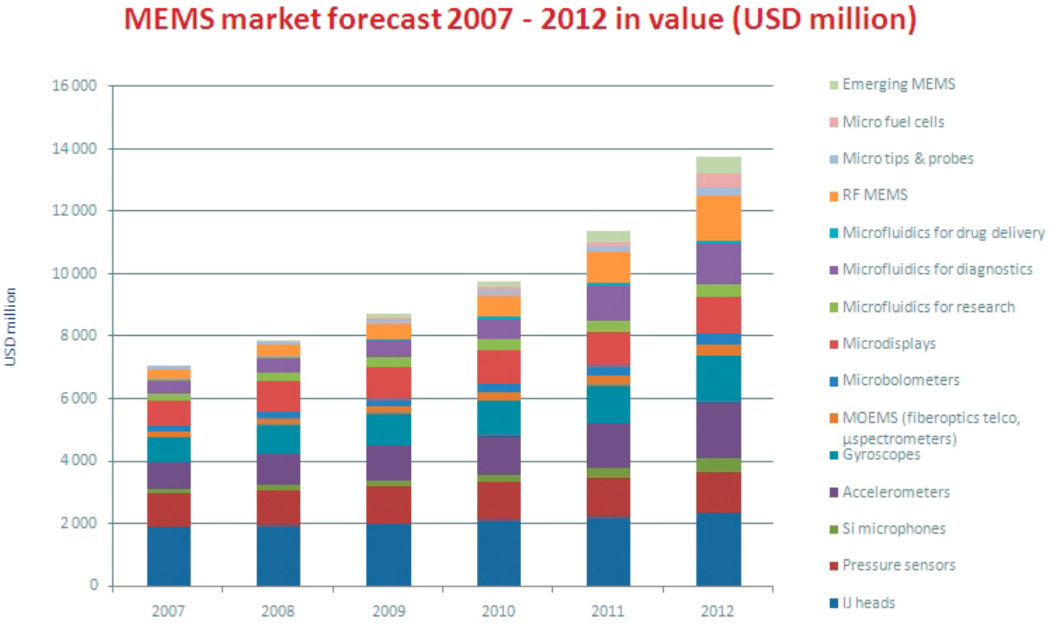

Figure 1.13 MEMS market forecast 2007-2012 in value (USD million)

They also realized a 2007-2012 forecast in number of units. In 2007, 2 billion MEMS units have been produced and 2.5 billion will be produced this year. But by 2012, it is 6.7 billion of MEMS devices which will be shipped worldwide. An interesting fact is that, despite the large 2007/2008 increase in units for MEMS (25%), the market value growth is "only" 9%. This effect is justified by a strong price pressure MEMS devices are currently subject to. After 2009, RF

MEMS and Si microphones will both contribute to the largest number of MEMS devices (over 45%).

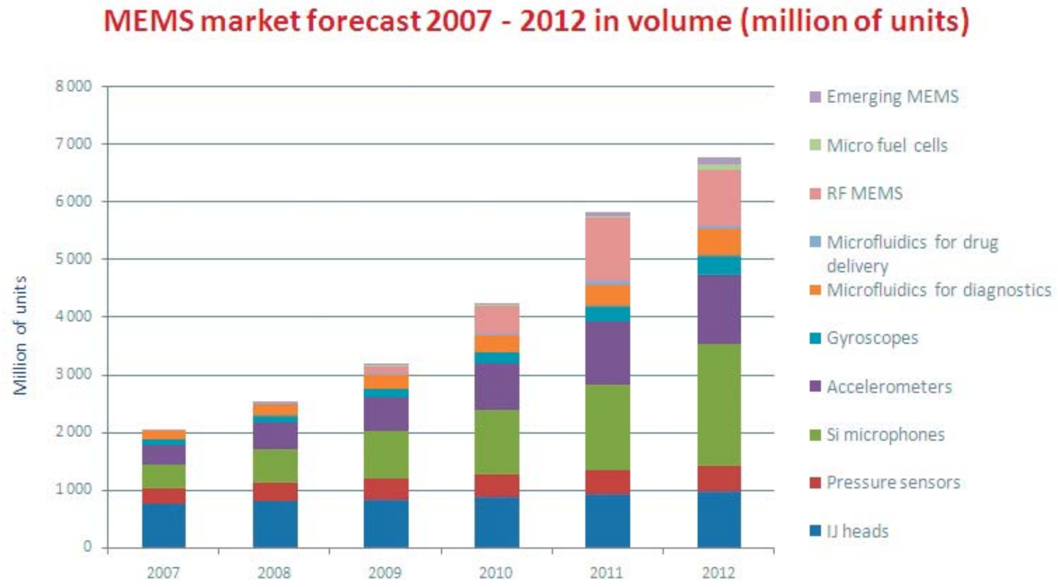

Figure 1.14 MEMS market forecast 2007-2012 in volume (million of units)

From this survey, it is clear that MEMS-related industries have a promising future. The acceleration in development in MEMS technology gives us great hope that the results of this development will be reflected in the market, leading to rapid market growth.

CHAPTER II. BACKGROUND INFORMATION

2.1 History of Gyroscopes

The earliest known gyroscope was made by Johann Bohnenberger in 1817, although he called it simply the "Machine." The French mathematician Pierre-Simon Laplace, working at the École Polytechnique in Paris, recommended the machine for use as a teaching aid, and thus it came to the attention of Léon Foucault. In 1852, Foucault used it in an experiment involving the rotation of the Earth. It was Foucault who gave the device its modern name – "Gyroscope", in an experiment to see the Earth's rotation, although the experiment was unsuccessful due to friction, which effectively limited each trial to 8 to 10 minutes, too short a time to observe significant movement.

In the 1860s, electric motors made the concept feasible, leading to the first prototype gyrocompasses; the first functional marine gyrocompass was developed between 1905 and 1908 by German inventor Hermann Anschütz-Kaempfe. The American Elmer Sperry followed with his own design in 1910, and other nations soon realized the military importance of the invention − in an age in which naval might was the most significant measure of military power − and created their own gyroscope industries. The Sperry Gyroscope Company quickly expanded to provide aircraft and naval stabilizers as well, and other gyroscope developers followed suit.

In 1917, the Chandler Company of Indianapolis, Indiana created the "Chandler gyroscope", a toy gyroscope with a pull string and pedestal. It has been in continuous production ever since and is considered a classic American toy.

MEMS gyroscopes take the idea of the Foucault pendulum and use a vibrating element in microscales, known as MEMS (Micro Electro-Mechanical System). The MEMS-based gyro was initially made practical and produceable by Systron Donner Inertial (SDI). Today, SDI is a large manufacturer of MEMS gyroscopes.

In the first several decades of the 20th century, other inventors attempted (unsuccessfully) to use gyroscopes as the basis for early black box navigational systems by creating a stable platform from which accurate acceleration measurements could be performed (in order to bypass the need for star sightings to calculate position). Similar principles were later employed in the development of inertial guidance systems for ballistic missiles.

2.2 Traditional Gyroscope

A gyroscope is a device for measuring or maintaining orientation, based on the principles of angular momentum. The device is a spinning wheel or disk whose axle is free to take any orientation. This orientation changes much less in response to a given external torque than it would without the large angular momentum associated with the gyroscope's high rate of spin. Since external torque is minimized by mounting the device in gimbals, its orientation remains nearly fixed, regardless of any motion of the platform on which it is mounted. Figure 2.1 is a traditional gyroscope. Figure 2.2 shows the three rotational degrees of freedom it can measure.

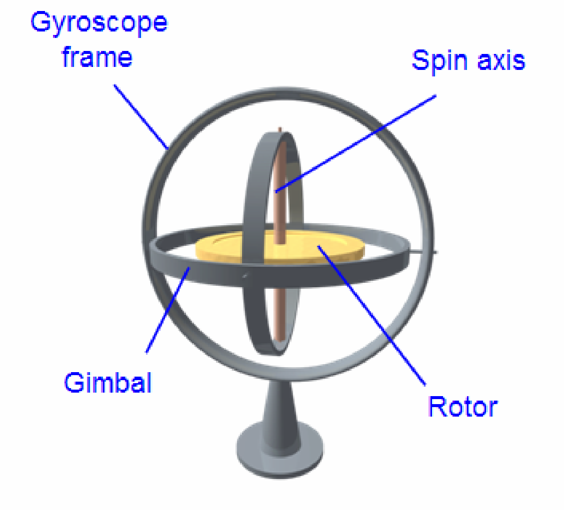

Figure 2.1 A traditional gyroscope

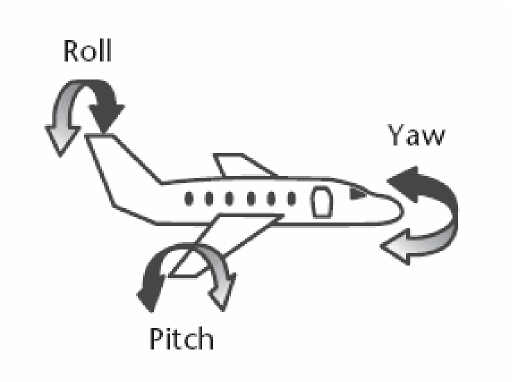

Figure 2.2 Three rotational degrees of freedom of the traditional gyroscope

Within mechanical systems or devices, a conventional gyroscope is a mechanism comprising a rotor journaled to spin about one axis, the journals of the rotor being mounted in an inner gimbal or ring, the inner gimbal being journaled for oscillation in an outer gimbal which in turn is journaled for oscillation relative to a support. The outer gimbal or ring is mounted so as to pivot about an axis in its own plane determined by the support. The outer gimbal possesses one degree of rotational freedom and its axis possesses none. The inner gimbal is mounted in the outer gimbal so as to pivot about an axis in its own plane, which axis is always perpendicular to the pivotal axis of the outer gimbal.

The axle of the spinning wheel defines the spin axis. The inner gimbal possesses two degrees of rotational freedom and its axis possesses one. The rotor is journaled to spin about an axis which is always perpendicular to the axis of the inner gimbal. So, the rotor possesses three degrees of rotational freedom and its axis possesses two. The wheel responds to a force applied about the input axis by a reaction force about the output axis. This is shown in Figure 2.2.

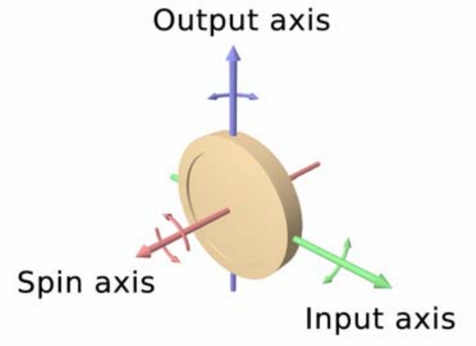

Figure 2.3 Diagram of a gyroscope wheel

The behavior of a gyroscope can be most easily appreciated by consideration of the front wheel of a bicycle. If the wheel is leaned away from the vertical so that the top of the wheel moves to the left, the forward rim of the wheel also turns to the left. In other words, rotation on one axis of the turning wheel produces rotation of the third axis.

A gyroscope flywheel will roll or resist about the output axis depending upon whether the output gimbals are of a free- or fixed- configuration. Examples of some free-output-gimbal devices would be the attitude reference gyroscopes used to sense or measure the pitch, roll and yaw attitude angles in a spacecraft or aircraft.

The center of gravity of the rotor can be in a fixed position. The rotor simultaneously spins about one axis and is capable of oscillating about the two other axes, and thus, except for its inherent resistance due to rotor spin, it is free to turn in any direction about the fixed point. Some gyroscopes have mechanical equivalents substituted for one or more of the elements, e.g., the spinning rotor may be suspended in a fluid, instead of being pivotally mounted in gimbals. A control moment gyroscope (CMG) is an example of a fixed-output-gimbal device that is used on spacecraft to hold or maintain a desired attitude angle or pointing direction using the gyroscopic resistance force.

In some special cases, the outer gimbal (or its equivalent) may be omitted so that the rotor has only two degrees of freedom. In other cases, the center of gravity of the rotor may be offset from the axis of oscillation, and thus the center of gravity of the rotor and the center of suspension of the rotor may not coincide.

The traditional gyroscope derives its precision from the large angular momentum that is proportional to the heavy mass of the flywheel, its substantial size, and its high rate of spin. This, in itself, precludes the use of miniature devices for useful gyroscopic action; the angular momentum of a miniature flywheel is miniscule. Therefore, micromachined sensors that detect angular rotation utilize the Coriolis effect instead of angular momentum.

2.3 Coriolis Effect

2.3.1 Phenomenon

The Coriolis effect, named after the French physicist Gaspard Coriolis, manifests itself in numerous weather phenomena, including hurricanes and tornadoes, and is a direct consequence of a body's motion in a rotating frame of reference. Figure 2.4 illustrates the Coriolis acceleration on an object moving with a velocity vector **v** on the surface of Earth from either pole towards the equator. The Coriolis acceleration deflects the object in a counterclockwise manner in the northern hemisphere and a clockwise direction in the southern hemisphere. The vector Ω represents the rotation of the planet.

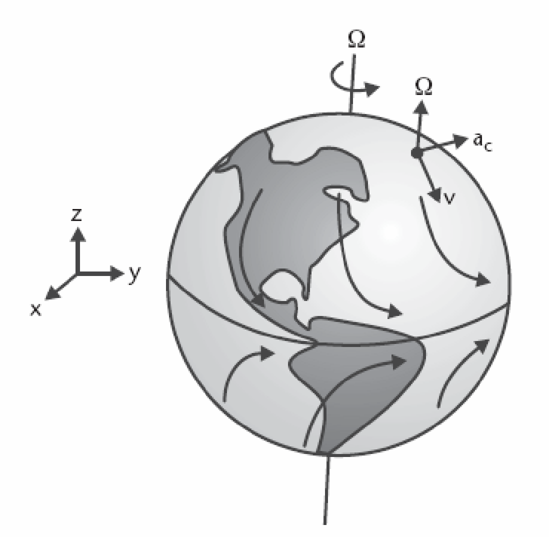

Figure 2.4 Coriolis force on the surface of the earth

To understand it, let us imagine an automobile driving from Seattle, Washington (lat. 48º N), to Los Angeles, California (lat. 34º N). At the beginning of its journey, the car in Seattle is actually moving eastward with the rotation of Earth (the rotating frame of reference) at about 1120 km/h1. At the end of its journey in Los Angeles, its eastward velocity is 1,385 km/h. As the car moves south across latitudes, its eastward velocity must increase from 1,120 to 1,385 km/h; otherwise, it will continuously slip and never reach its destination. The road − effectively the rotating surface − imparts an eastward acceleration to maintain the vehicle on its course. This is the Coriolis acceleration. In general, the Coriolis acceleration is the acceleration that must be applied in order to maintain the heading of a body moving on a rotating surface [5].

All micromachined angular rate sensors have a vibrating element at their core − this is the moving body. In a fixed frame of reference, a point on this element oscillates with a velocity vector **v**. If the frame of reference begins to rotate at a rate Ω, this point is then subject to a Coriolis force and a corresponding acceleration $\mathbf{a_c}$ [6]. The vector cross operation implies that the Coriolis acceleration and the resulting displacement at that point are perpendicular to the oscillation. This, in effect, sets up an energy transfer process from a primary mode of oscillation into a secondary mode that can be measured. It is this excitation of a secondary resonance mode that forms the basis of detection using the Coriolis effect. In beam structures, these two frequencies are distinct with orthogonal displacements. But for highly symmetrical elements, such as rings, cylinders, or disks, the resonant frequency is degenerate, meaning there are two distinct modes of resonance sharing the same oscillation frequency. This degeneracy causes the temporal excitation signal (primary mode) to be in phase quadrature with the sense signal (secondary mode), thus minimizing coupling between these two modes and improving sensitivity and accuracy [7]. Additionally, the degeneracy tends to minimize the device’s sensitivity to thermal errors, aging, and long-term frequency drifts.

2.3.2 Definition

In nonvector terms: at a given rate of rotation of the observer, the magnitude of the Coriolis acceleration of the object is proportional to the velocity of the object and also to the sine of the angle between the direction of movement of the object and the axis of rotation.

The vector formula for the magnitude and direction the Coriolis acceleration is

$$\vec{a}_c = -2\vec{\Omega} \times \vec{v}\ , \tag{2.1}$$

where $\vec{v}$ is the velocity of the particle in the rotating system, and $\vec{\Omega}$ is the angular velocity vector which has magnitude equal to the rotation rate ω and is directed along the axis of rotation of the rotating reference frame, and the × symbol represents the cross product operator. The formula implies that the Coriolis acceleration is perpendicular both to the direction of the velocity of the moving mass and to the frame's rotation axis.

The equation may be multiplied by the mass of the relevant object to produce the Coriolis force:

$$\vec{F}_C = -2m\vec{\Omega} \times \vec{v}\ . \tag{2.2}$$

2.3.3 Tuning Fork Structure

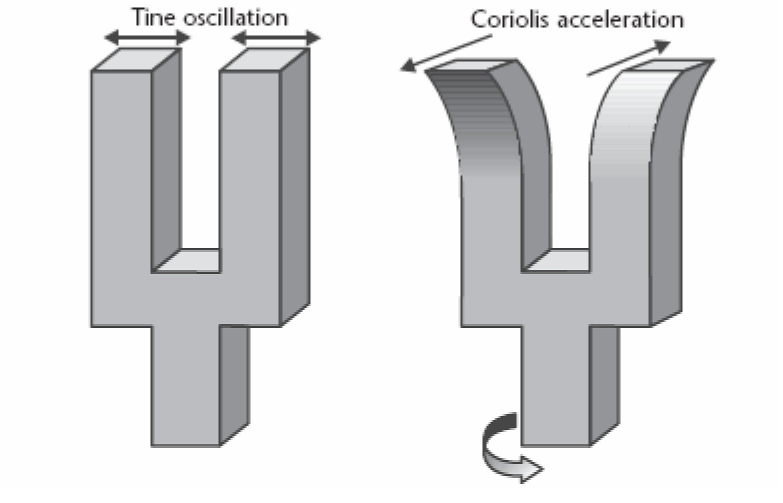

Figure 2.5 Tuning fork structure for angular-rate sensing

A simple and common implementation of Coriolis effect is the tuning-fork structure (see Figure 2.5). The two tines of the fork normally vibrate in opposite directions in the plane of the fork (flexural mode). The Coriolis acceleration subjects the tips to a displacement perpendicular to the primary mode of oscillation, forcing each tip to describe an elliptical path. Rotation, hence, excites a secondary vibration torsional mode around the stem with energy transferred from the primary flexural vibration of the tines.

2.4 MEMS Gyroscopes

Virtually all micromachined gyroscopes rely on a mechanical structure that is driven into resonance and excites a secondary oscillation in either the same structure or in a second one, due to the Coriolis force. Figure 2.6 provides a summary of various design choices can be made for design of a vibrating gyroscope, with over 2500 potential combinations.

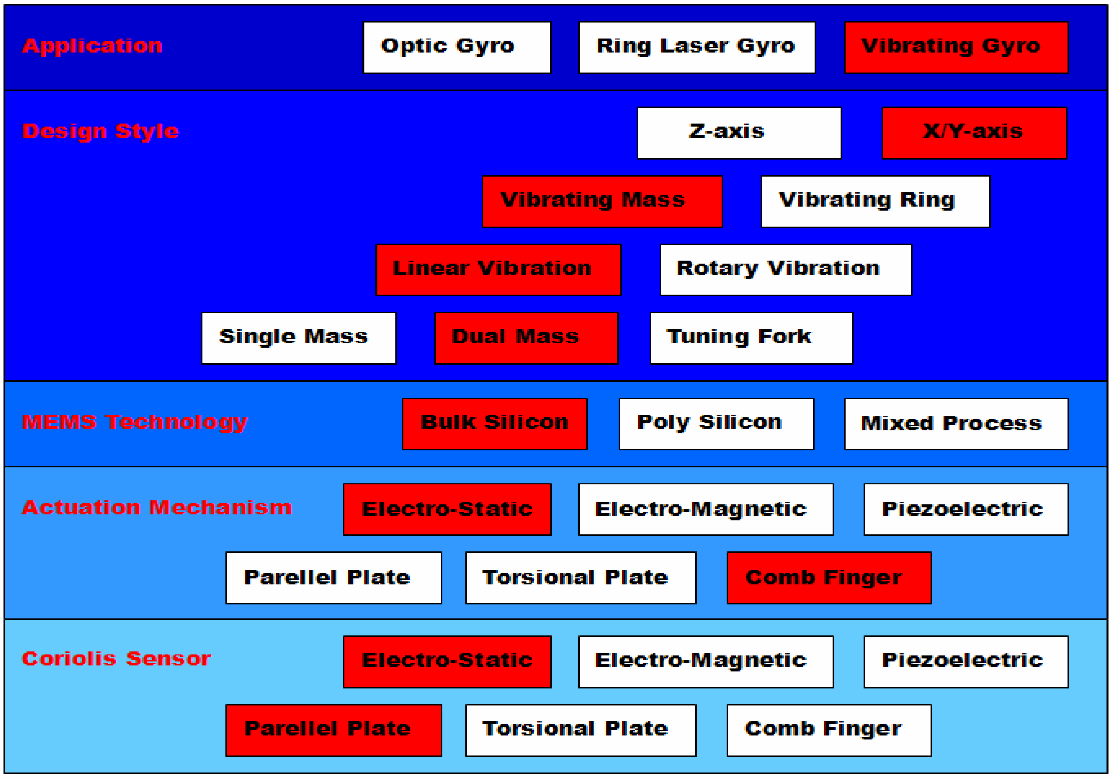

Figure 2.6 Various options that could be used for designing a gyroscope

Early micromachined gyroscopes were based on double-ended tuning forks. Two tines, which are joined at a junction bar, are excited to resonate in antiphase along one axis. Rotation causes the tines to resonate along the perpendicular axis. Different actuation mechanisms can be used to excite the primary or driven oscillation mode. Electromagnetic actuation has the advantage that large oscillation amplitudes are easily achievable. A severe disadvantage, however, is that it requires a permanent magnet to be mounted in close proximity to the sensing element, thereby making the fabrication process not completely compatible with that of batch processing. Piezoelectric excitation has also been reported, who realized a double-ended tuning fork structure with the oscillation direction perpendicular to the wafer surface using bulk micromachining. The prevailing approach for prototype gyroscopes, however, is to use electrostatic forces to excite the primary oscillation. For detecting the secondary or sense oscillation, different position measurement techniques have been used such as piezoresistive, tunneling current, optical, and capacitive, the latter being by far the predominant method.

The sensors from Delphi Delco Electronics Systems, Robert Bosch GmbH, Daimler Benz AG, and Silicon Sensing Systems illustrate four vibratory-type angular-rate sensors distinct in their str ucture as well as excitation and sense methods.

2.4.1 Gyroscope from Delphi Delco Electronics Systems

The sensor from Delphi Delco Electronics Systems of Kokomo, Indiana [8], a division of Delphi Corporation of Troy, Michigan, includes at its core a vibrating ring shell based on the principle of the ringing wine glass discovered in 1890 by G. H. Bryan. He observed that the standing-wave pattern of the wine glass did not remain stationary in inertial space but participated in the motion as the glass rotated about its stem.

The complete theory of vibrating-ring angular-rate sensors is well developed [9]. The ring shell, anchored at its center to the substrate, deforms as it vibrates through a full cycle from a circle to an ellipse, back to a circle, then to an ellipse rotated at right angles to the first ellipse, then back to the original circle (see Figure 2.7). The points on the shell that remain stationary are called nodes, whereas the points that undergo maximal deflection are called antinodes. The nodes and antinodes form a vibration pattern (or standing-wave pattern) around the ring. The pattern is characteristic of the resonance mode. Because of symmetry, a ring shell possesses two frequency-degenerate resonant modes with their vibration patterns offset by 45º with respect to each other. Hence, the nodes of the first mode coincide with the antinodes of the second mode. The external control electronics excite only one of the two modes − the primary mode. But under rotation, the Coriolis effect excites the second resonance mode, and energy transfer occurs between the two modes. Consequently, the deflection amplitude builds up at the antinodes of the second mode − also, the nodes of the first mode. The overall vibration becomes a linear combination of the two modes with a new set of nodes and antinodes forming a vibration pattern rotated with respect to the pattern of the primary mode. It is this lag that Bryan heard in his spinning wine glass. In an open-loop configuration, the deflection amplitude at the nodes and antinodes is a measure of the angular rate of rotation. Alternatively, the angular shift of the vibration pattern is another measure. In a closed-loop configuration, electrostatic actuation by a feedback voltage applied to the excitation electrodes nulls the secondary mode and maintains a stationary vibration pattern. The angular rate becomes directly proportional to this feedback voltage.

A total of 32 electrodes positioned around the suspended ring shell provide the electrostatic excitation drive and sense functions. Of this set, eight electrodes strategically positioned at 45º intervals (at the nodes and antinode) capacitively sense the deformation of the ring shell. Appropriate electronic circuits complete the system control functions, including feedback. A phased-locked loop (PLL) drives the ring into resonance through the electrostatic drive electrodes and maintains a lock on the frequency. Feedback is useful to electronically compensate for the mechanical poles and increase the closed-loop bandwidth of the sensor.

Additionally, a high mechanical quality factor increases the closed-loop system gain and sensitivity.

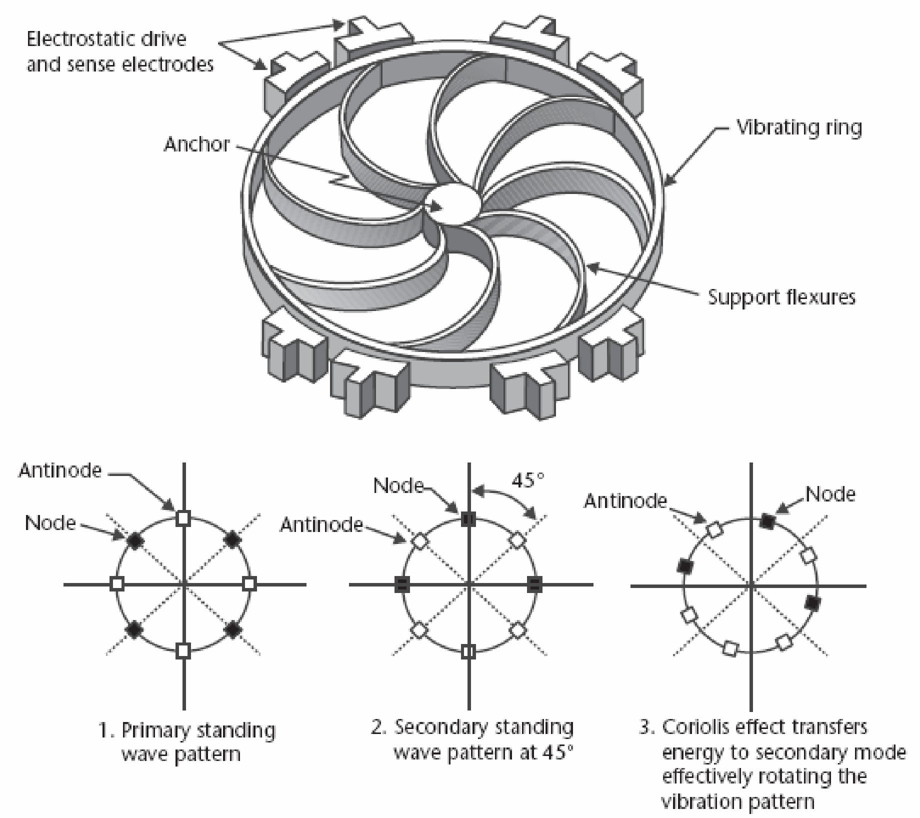

Figure 2.7 Delphi Delco angular-rate sensor and the corresponding standing-wave pattern

Researchers at the University of Michigan demonstrated a polysilicon version of the sensor with improved overall performance. The demonstrated specifications of the Delphi Delco sensor over the temperature range of –40° to +125ºC include a resolution of 0.5º/s over a bandwidth of 25 Hz, limited by noise in the electronic circuitry. The nonlinearity in a rate range of ±100 º/s is less than 0.2º/s. The sensor survives the standard automotive shock test: a drop from a height of one meter. The specifications are adequate for most automotive and consumer applications.

2.4.2 Gyroscope from Silicon Sensing Systems

The CRS family of yaw-rate sensors from Silicon Sensing Systems, a joint venture between BAE Systems of Plymouth, Devon, England, and Sumitomo Precision Products Company of Japan, is aimed at commercial and automotive applications. It also uses a vibratory ring shell similar to the sensor from Delphi Delco but differs on the excitation and sense methods. Electric current loops in a magnetic field, instead of electrostatic electrodes, excite the primary mode of resonance. These same loops provide the sense signal to detect the angular position of the vibration pattern (see Figure 2.8).

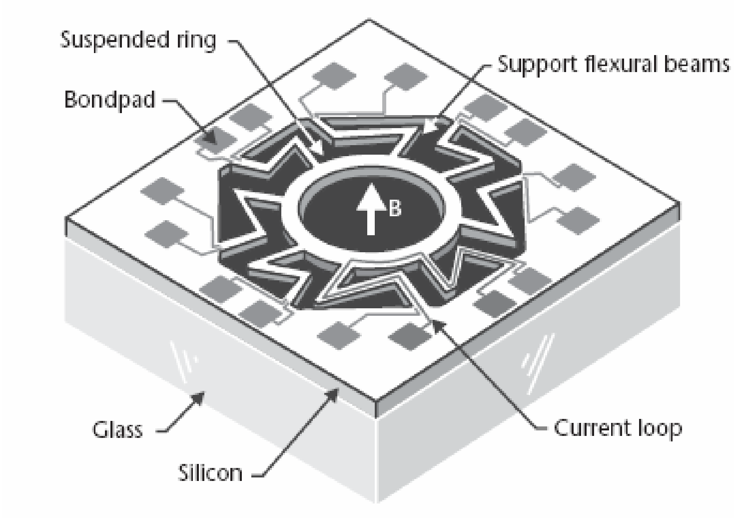

Figure 2.8 CRS angular-rate sensor from Silicon Sensing Systems

The ring, 6 mm in diameter, is suspended by eight flexural beams anchored to a 10-mm-square frame. Eight equivalent current loops span every two adjacent support beams. A current loop starts at a bond pad on the frame, traces a support beam to the ring, continues on the ring for one eighth of the circumference, then moves onto the next adjacent support beam, before ending on a second bond pad. Under this scheme, each support beam carries two conductors. A Samarium-Cobalt permanent magnet mounted inside the package provides a magnetic field perpendicular to the beams. Electromagnetic interaction between current in a loop and the magnetic field induces a Lorentz force. Its radial component is responsible for the oscillation of the ring in the plane of the die at approximately 14.5 kHz − the mechanical resonant frequency of the ring. The sensing mechanism measures the voltage induced around one or more loops in accordance with Faraday's law: As the ring oscillates, the area of the current loop in the magnetic flux changes, generating a voltage. Two diametrically opposite loops perform a differential voltage measurement. One can simplistically view an actuating and a sensing loop as the primary and secondary windings of a transformer; the electromagnetic coupling between them depends on the ring vibration pattern and thus on the angular rate of rotation.

Closed-loop feedback improves the overall performance by increasing the bandwidth and reducing the system's sensitivity to physical errors. Two separate feedback loops with automatic gain control circuits maintain a constant oscillation amplitude for the primary mode of resonance and a zero amplitude for the secondary resonance mode. The feedback voltage required to null the secondary mode is a direct measure of the rate of rotation.

The specification sheet of the CRS03-02 gives an output scale factor of 20 mV/(º/s) with a variation of ±3% over a temperature range from –40° to +85ºC. The noise is less than 1 mV rms from 3 to 10 Hz. The nonlinearity in a rate range of ±100 º/s is less than 0.5 º/s. The operating current is a relatively large 50 mA at a nominal 5-V supply.

2.4.3 Gyroscope from Daimler Benz

The sensor from Daimler Benz AG of Stuttgart, Germany [10], is a strict implementation of a tuning fork using micromachining technology (see Figure 2.9). The tines of the silicon tuning fork vibrate out of the plane of the die, driven by a thin-film piezoelectric aluminum nitride actuator on top of one of the tines. The Coriolis forces on the tines produce a torquing moment around the stem of the tuning fork, giving rise to shear stresses that can be sensed with diffused piezoresistive elements. The shear stress is maximal on the center line of the stem and corresponds with the optimal location for the piezoresistive sense elements.

The high precision of micromachining is not sufficient to ensure the balancing of the two tines and the tuning of the two resonant frequencies − the vibration modes of a tuning fork are not degenerate. An imbalance in the tines produces undesirable coupling between the excitation and sense resonant modes, which degrades the resolution of the device. A laser ablation step precisely removes tine material and provides calibration of the tuning fork. For this particular design, all resonant modes of the fork are at frequencies above 10 kHz. To minimize coupling to higher orders, the primary and secondary modes are separated by at least 10 kHz from all other remaining modes. The choice of crystalline silicon for tine material allows achieving a high quality factor (~ 7,000) at pressures below 10^{-5} bar.

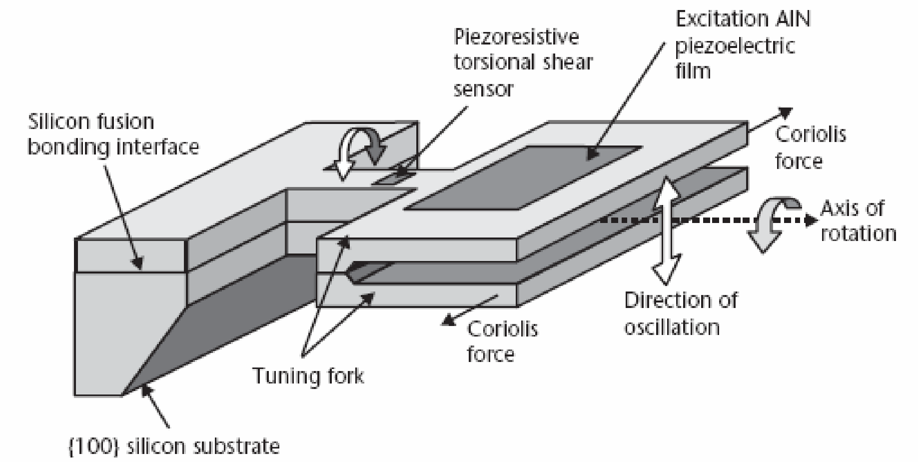

Figure 2.9 Angular-rate sensor from Daimler Benz

The measured frequency of the primary, flexural mode (excitation mode) was 32.2 kHz, whereas the torsional secondary mode (sense mode) was 245 Hz lower. Typical of tuning forks, the frequencies exhibited a temperature dependence. For this particular technology, the temperature coefficient of frequency is –0.85 Hz/ºC.

2.4.4 Gyroscope from Robert Bosch

This sensor from Robert Bosch GmbH of Stuttgart, Germany, is unique in its implementation of a mechanical resonant structure equivalent to a tuning fork [11]. An oscillator system consists of two identical masses coupled to each other by a spring and suspended from an outer frame by two other springs (see Figure 2.10).

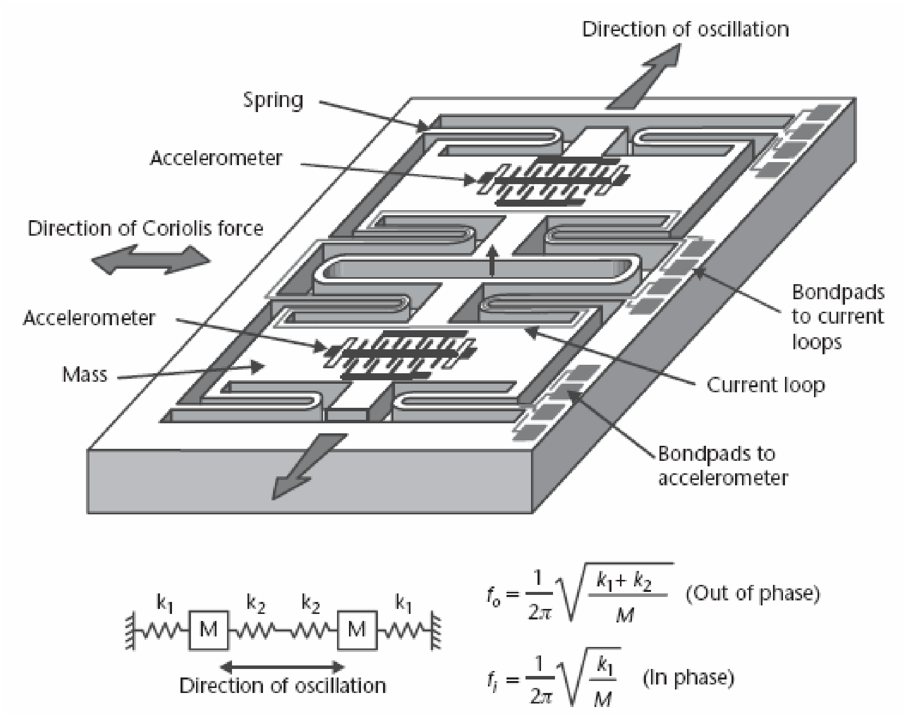

Figure 2.10 Yaw-rate sensor from Robert Bosch GmbH and the simplified mechanical model

Such a coupled system has two resonant frequencies: in phase, and out of phase. In the inphase oscillation mode, the instantaneous displacements of the two masses are in the same direction. In the out-of-phase mode, the masses are moving, at any instant, in opposite directions. A careful selection of the coupling spring provides sufficient separation between the in-phase and out-of-phase resonant frequencies. Lorentz forces generated by an electric current loop within a permanent magnetic field excite only the out-of-phase mode. The oscillation electromagnetically induces a voltage in a second current loop that provides a feedback signal proportional to the velocity of the masses. The resulting Coriolis forces on the two masses are in opposite directions but orthogonal to the direction of oscillation. Two polysilicon surface-micromachined accelerometers with capacitive comb structures (similar in their basic operation to the ADXL family of sensors) measure the Coriolis accelerations for each of the masses. The difference between the two accelerations is a direct measure of the angular yaw rate, whereas their sum is proportional to the linear acceleration along the accelerometer's sensitive axis. Electronic circuits perform the addition and subtraction functions to filter out the linear acceleration signal.

For the Bosch sensor, the out-of-phase resonant frequency is 2 kHz, and the maximum oscillation amplitude at this frequency is 50 μm. The measured quality factor of the oscillator at atmospheric pressure is 1,200, sufficiently large to excite resonance with small Lorentz forces. The stimulated oscillation subjects the masses to large accelerations reaching approximately 800G. Though they are theoretically perpendicular to the sensitive axis of the accelerometers, in practice, some coupling remains, which threatens the signal integrity. However, because the two temporal signals are in phase quadrature, adopting synchronous demodulation methodsallows the circuits to filter the spurious coupled signal with a rejection ratio exceeding 78 dB. This is indeed a large rejection ratio but insufficient to meet the requirements of inertial navigation.

The peak Coriolis acceleration for a yaw rate of 100º/s is only 200 mG. This requires extremely sensitive accelerometers with compliant springs. The small Coriolis acceleration further emphasizes the need for perfect orthogonality between the sense and excitation axes. Closed-loop position feedback of the acceleration sense element compensates for the mechanical poles and increases the bandwidth of the accelerometers to over 10 kHz.

The sensitivity of the device is 18 mV/(º/s) in the range of ±100 º/s over 40° to +85ºC. The temperature dependence of the uncompensated sensor causes an offset amplitude of 0.5 º/s over the specified temperature range, but signal conditioning circuits reduce this dependence by implementing appropriate electronic temperature compensation schemes.

2.5 Application

MEMS gyroscopes have a various implementations, including:

- Spacecraft Orientation: The oscillation can also be induced and controlled in the vibrating structure gyroscope for the positioning of spacecraft such as Cassini-Huygens. These small Hemispherical Resonator Gyroscopes made of quartz operate in vacuum. They provide accurate 3 axis positioning of the spacecraft and are highly reliable over the years as they don't have any moving parts.

- Automotive: Automotive yaw sensors can be built around vibrating structure gyroscopes. These are used to detect error states in yaw compared to a predicted response when connected as an input to electronic stability control systems in conjunction with a steering wheel sensor. Advanced systems could conceivably offer rollover detection based on a second VSG (Vibrating Structure Gyroscope) but it is cheaper to add longitudinal and vertical accelerometers to the existing lateral one to this end.

- Entertainment: The Nintendo Game Boy Advance game WarioWare: Twisted! uses a piezoelectric gyroscope to detect rotational movement. The Nintendo Wii MotionPlus accessory uses multi-axis MEMS gyroscopes to augment the motion sensing capabilities of the Wii Remote.

- Photography: Many Image stabilization systems on video and still cameras employ vibrating structure gyroscopes.

- Hobbies: Vibrating structure gyroscopes are commonly used in radio-controlled helicopters to help control the helicopter's tail rotor or in radio-controlled airplanes to help keep the tail steady during take-off or hand (especially with discus launched gliders) launch.

- Other: The Segway Human Transporter employs a vibrating structure gyroscope made by Silicon Sensing Systems to maintain stability of the operator platform.

CHAPTER III. GYROSCOPE DESIGN

3.1 Working Principle

MEMS mechanical gyroscopes developed so far are exclusively vibratory gyroscopes. A typical vibratory gyroscope can be expressed as a mass suspended by springs along two perpendicular directions, as shown in Figure 3.1.

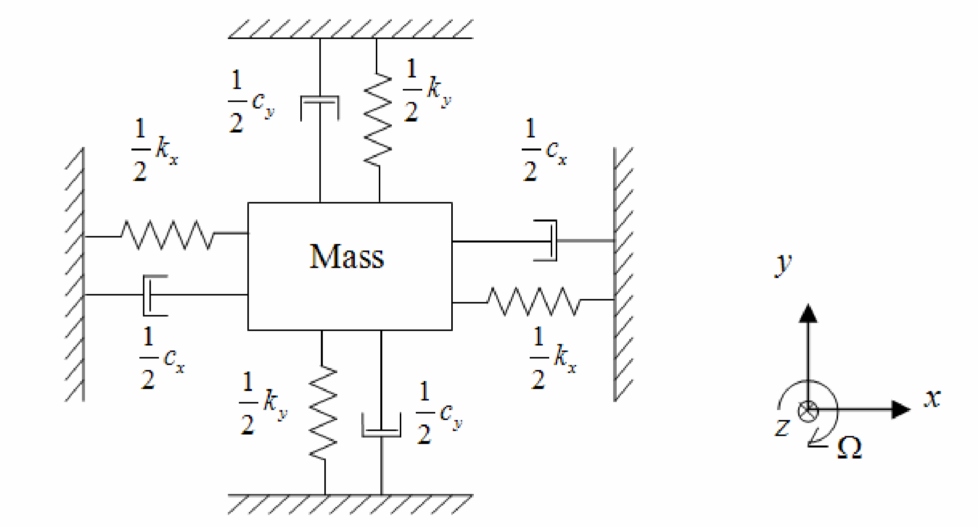

Figure 3.1 Working principle of a MEMS vibratory gyroscope

The system is a two dimensional vibration system with two orthogonal vibration modes. One vibration mode corresponds to the vibration of the mass in the x-direction. The vibration frequency of the first vibration mode is w_x. The other vibration mode corresponds to the vibration of the mass in the y-direction with a frequency of w_y.

For operation, the central movable mass is activated by electrostatic driving force $\vec{F}_d(t)$ along x-direction (driving mode). Assume $\vec{F}_0$ is a constant driving force and w_d is the driving frequency, the electrostatic driving force is in a sinusoidal format:

$$\vec{F}_d(t) = \vec{F}_0 \cos w_d t \,. \tag{3.1}$$

Then, if the system rotates around the z-axis (normal to the paper plane) with an angular velocity of $\vec{\Omega}$, an alternating force in the y-direction is induced by Coriolis effect. Thus, the system is driven into vibration in the y-direction with a frequency of w_y. According to the previous discussion, a mass m with velocity $\vec{v}(t)$ along x-direction, which is in a reference frame with an angular velocity $\vec{\Omega}$ along z-direction, will experience a Coriolis force $\vec{F}_c(t)$ along y-direction:

$$\vec{F}_c(t) = 2m\vec{v}(t)\times\vec{\Omega}\,. \tag{3.2}$$

By using some sensing schemes to measure the vibration amplitude in sensing mode, we can know the value of the angular velocity.

As the Coriolis force is usually extremely weak, it is important to make full use of the amplification effect of mechanical resonance and to keep the noise level low in the signal bandwidth. Therefore, the driving frequency, w_d, and the two resonant frequencies, w_x and w_y, have to be designed carefully, and sophisticated electronic circuits have to be used.

For a practical gyroscope device, the design, fabrication, packaging and signal conditioning circuitry are quite complicated. The design is related to driving schemes, damping control and sensing schemes. The fabrication is difficult as the requirement for the resonant frequencies of the structure is strict and, quite often, the structure has to be encapsulated in a vacuum. The signal detection is difficult because of the extremely weak signal and phase differences among the electrical driving signals, driving vibration and detection vibration cased by mechanical reasons and the air damping effect.

The brief description of MEMS gyroscope working principle above has shown that the design and analysis of these devices are based on much background theory, including driving schemes, sensing schemes, vibration frequency of a beam-mass structure, forced vibration of a micro mechanical structure, air damping effect on vibration. We need to solve all these issues in MEMS gyroscopes design. Electrostatic driving techniques will be discussed in Section 3.2; capacitive sensing techniques will be discussed in Section 3.3; vibration frequency of a mechanical structure will be discussed in Section 3.4; forced vibration amplitude will be discussed in Section 3.5; air damping and its effects will be discussed in Section 3.6.

3.2 Electrostatic Driving

There are many kinds of MEMS actuation techniques: electrostatic actuation, piezoelectric actuation, thermal actuation, magnetic actuation, even phase recovery actuation using shape memory alloy. Among them, electrostatic actuation is the most popular one.

Conventional mechanical actuators are rarely driven by an electrostatic force because the force is usually too small to displace or lift mechanical parts unless the voltage used is extremely high. With the miniaturization of mechanical structures, the electrostatic force becomes relatively large. Therefore, electrostatic driving has found wide applications in micro mechanical actuation.

Electrostatic actuation relies on electrostatic attractive forces on plates with opposite polarities, and can be classified into perpendicular driving and lateral driving. Electrostatic driving is widely used MEMS technology because of its unique advantage in application. For example, it is easy for implementation, compatible with CMOS CLSI circuits, etc.

3.2.1 Electrostatic Force

From basic physics knowledge, we know that there are two kinds of electrical charge − "positive" and "negative". Charges of the same kind repel each other while charges of opposite kind attract each other. This force is called electrostatic force (see Figure 3.2).

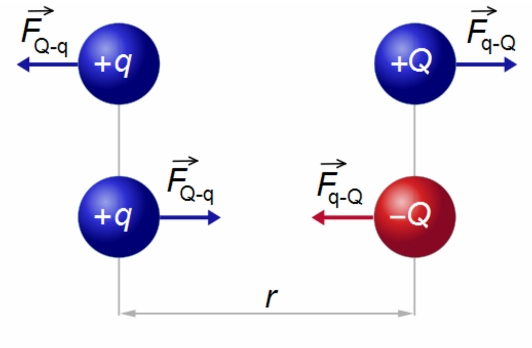

Figure 3.2 Electrostatic force

The fundamental equation of electrostatic force is Coulomb's law, which describes the force between two point charges. The magnitude of the electrostatic force between two point electric charges is directly proportional to the product of the magnitudes of each charge, q_1 and q_2, and inversely proportional to the square of the distance between the charges, r:

$$F = \frac{q_1 q_2}{4\pi\varepsilon_0 r^2}, \tag{3.3}$$

where ε_0 is the electric constant, or the permittivity of a vacuum, a defined value:

$$\varepsilon_0 = 8.854 \times 10^{-12} F/m. \tag{3.4}$$

3.2.2 Perpendicular Driving

Consider an electrostatic actuator consisting of a battery and a capacitor of parallel plate as shown in Figure 3.3. The two plates of the parallel-plate capacitor are movable in the normal direction.

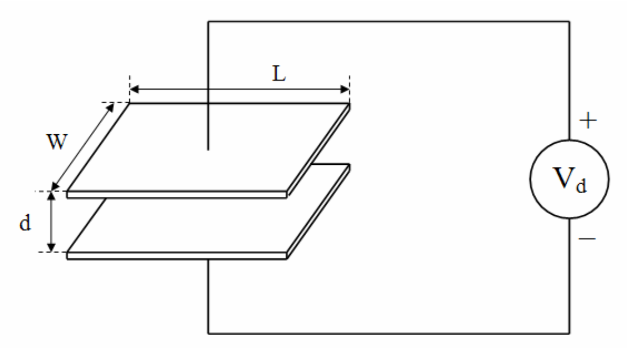

Figure 3.3 The electrostatic perpendicular driving force on the plates

The capacitance of the parallel plate actuator is:

$$C(x) = \frac{\varepsilon_0 WL}{x}, \tag{3.5}$$

where W and L are the width and length of the parallel plates; x is the distance between two plates (when there is no voltage applied, x equals to the original gap distance d); ε_0 is the permittivity of a vacuum (the permittivity of air is approximately equal to the permittivity of a vacuum). For convenience, we assume that the energy of the battery in the original state is E_0 and the energy of the capacitor is zero.

If we assume the voltage of the battery is V_d, the electric charge stored in the capacitor is

$$Q_C = C(x)V_d. \tag{3.6}$$

The energy stored in the capacitor is

$$E_C = \frac{1}{2}C(x){V_d}^2. \tag{3.7}$$

Due to the charging to the capacitor, the energy of the battery is reduced to

$$E_B = E_0 - Q_C V_d = E_0 - C(x){V_d}^2. \tag{3.8}$$

Therefore, the energy of the capacitor-battery system becomes

$$E(x) = E_B + E_C = E_0 - \frac{1}{2}C(x){V_d}^2 = E_0 - \frac{\varepsilon_0 WL}{2x}{V_d}^2. \tag{3.9}$$

From Equation (3.9), the normal electrostatic force applied on the movable plate of the capacitor is

$$F_{en} = -\frac{\partial E(x)}{\partial x} = -\frac{\varepsilon_0 WL}{2x^2}{V_d}^2. \tag{3.10}$$

The negative sign of the force indicated that the force is attractive.

According to Equation (3.10), the attractive perpendicular force between the two parallel plates keeps constant when the dimensions of the plates and the gap distance are scaled down with the same factor. This is one of the favorable features of electrostatic force in micromachining application.

However, perpendicular electrostatic driving also has its limitations. First, the driving force is not a constant, depending on the gap distance. Second, pull-in effect may occur if the gap distant is too small or the electrostatic force is too large.

What is pull-in effect? Let us consider a parallel-plate actuator with a mass supported by elastic beams on both sides so that it can move only in its normal direction as shown in Figure 3.4(a). The mass is used as a movable electrode and the fixed electrode is under the mass with an original gap distance of d. When the electrodes are supplied with a voltage difference, V_d, an electrostatic force is applied to the mass, pulling it towards the fixed electrode as shown in Figure 3.4(b). Once the mass is displaced, an elastic recovery force by the beams tends to pull the mass back towards its original position. The balanced position of the mass is simply determined by the condition of force balance. However, the problem is not straightforward due to the nonlinear nature of the electrostatic force, which may cause instability problem in some conditions.

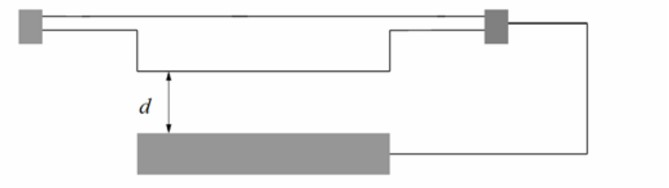

(a)

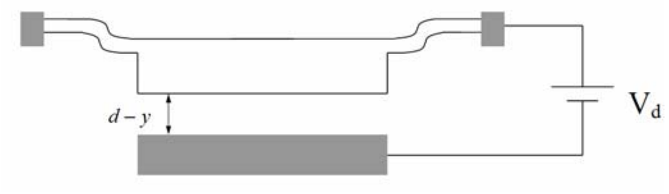

(b)

Figure 3.4 A mass suspended by elastic beams (a) without electrostatic force; (b) with electrostatic force

Suppose that the displacement of the mass is y . Due to the joint action of the electrostatic force and the elastic force, the condition of force balance is

$$F = F_{en} + F_k = 0 . \tag{3.11}$$

where F_{en} is the electrostatic force and F_k is the elastic recovery force. The balanced displacement is determined by

$$\frac{\varepsilon_0 WL{V_d}^2}{2(d-y)^2} - ky = 0 . \tag{3.12}$$

Equation (3.12) is investigated using a graphic method. The curves of F_{en} and $|F_k|$ as functions of displacement, y , are shown in figure 3.5. The curve for F_{en} is a hyperbola while the curve for $|F_k|$ is a straight line starting from the origin of the coordinates. If $|F_k|$ is large enough, the two curves intersect at points a and b as shown in the figure.

We can see that the solution corresponding to point b is not a stable state. If a small disturbance moves the mass back a little, the recovery force F_k will be larger than the electrostatic attractive force in quantity and move it back further until it falls to point a. On the other hand, if a disturbance moves the mass a little farther from point b, the electrostatic force will always be larger than the elastic recovery force and the mass will move forward continuously until falling into contact with fixed electrode. However, the solution corresponding to point a is a stable one as the mass will always return to the balanced position after a disturbance force moving it away from the point.

From the mathematic condition for a stable state $\partial F / \partial y < 0$, we have

$$\frac{\varepsilon_0 WL{V_d}^2}{(d-y)^3} - k < 0 . \tag{3.13}$$

From Equation (3.12) and (3.13), we have

$$y < \frac{1}{3} d . \tag{3.14}$$

This means that the balanced displacement is stable when the balanced position of the plate is less than one third of its original distance from the fixed electrode.

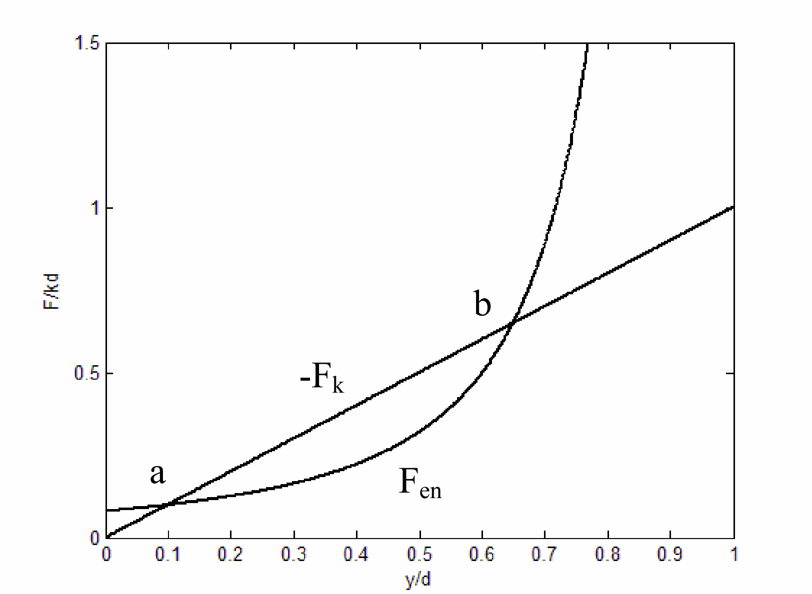

Figure 3.5 The dependence of electrostatic force F_{en} and elastic force $|F_k|$ on displacement

For a specific mechanical structure, k is a constant. From Figure 3.5, we can see that the curve for F_{en} moves up with voltage V_d. Therefore, the points a and b move closer with the increased V_d. It is conceivable that, for a critical voltage V_{po}, point a and b merge. For any voltage larger than V_{po}, there will be no intersection between the two curves. As, in this case, F_{en} is always larger than $|F_k|$ for $V_d > V_{po}$, the mass will always move towards the fixed electrode and falls into contact with fixed electrode finally. This phenomenon is called the pull-in effect and V_{po} is referred to as a pull-in voltage.

The pull-in voltage V_{po} can be found from Equation (3.12) directly. However, for generalization, further discussion will be made using the following dimensionless notations:

$$\tilde{y} = \frac{y}{d} \text{ and } p = \frac{F_{eo}}{kd} . \tag{3.15}$$

Thus, Equation (3.12) can be written as

$$\tilde{y}(1-\tilde{y})^2 = p . \tag{3.16}$$

The maximum of $\tilde{y}(1-\tilde{y})^2$ in the region of 0 to 1 is 4/27 at $\tilde{y} = 1/3$. Therefore, the condition for a stable solution is $p \leq 4/7$. The pull-in voltage is thus found to be

$$V_{po} = \sqrt{\frac{8kd^3}{27\varepsilon_0 WL}}. \tag{3.17}$$

For a voltage V_d smaller than V_{po}, the displacement of the mass can be found from Equation (3.16) by iterated calculation. If p is small, $\tilde{y}$ increases with p quite linearly. However, $\tilde{y}$ increases abruptly with p when p reaches 4/27 (i.e., V_d reaches the pull-in voltage V_{po}). Once the mass in pulled-in, it would not be released until the voltage is taken away completely (i.e., $V_d = 0$).

In MEMS gyroscope design, we should always try to eliminate pull-in effect in perpendicular electrostatic driving.

3.2.3 Lateral Driving

Consider a system consisting of a battery and a capacitor of parallel plate. But now the two parallel plates are separated by a constant gap distance d, and are movable in their plane as shown in Figure 3.6. Suppose that there is a misalignment between parallel plates, and the overlapping distance, x, is much larger than the gap distance, d.

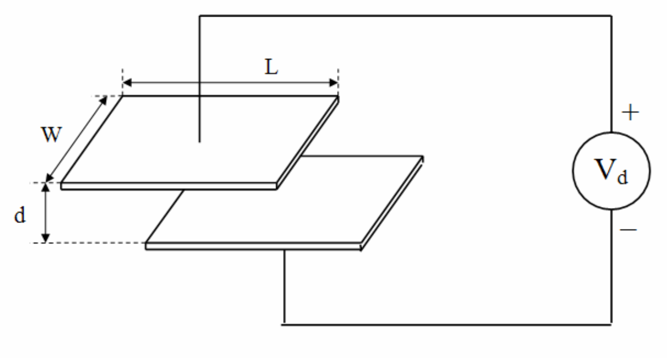

Figure 3.6 The electrostatic lateral driving force on the plates

The capacitance between the tow plates is:

$$C(x) = \frac{\varepsilon_0 Wx}{d}. \tag{3.18}$$

Again, the energy of the battery is supposed to be E_0 before the capacitor is connected to the battery. Once the capacitor is connected to the battery, the electric charge stored in the capacitor is

$$Q_C = C(x)V_d, \tag{3.19}$$

and the energy stored in the capacitor is

$$E_C = \frac{1}{2}C(x)V_d^{\,2}. \tag{3.20}$$

Due to the charging to the capacitor, the energy of the battery is reduced to

$$E_B = E_0 - Q_C V_d = E_0 - C(x) V_d^{\ 2} . \tag{3.21}$$

Therefore, the energy of the capacitor-battery system becomes

$$E(x) = E_B + E_C = E_0 - \frac{1}{2} C(x) V_d^{\ 2} = E_0 - \frac{\varepsilon_0 W x}{2d} V_d^{\ 2} . \tag{3.22}$$

From Equation (3.22), the lateral electrostatic force applied on the movable plate of the capacitor is

$$F_{el} = -\frac{\partial E(x)}{\partial x} = \frac{\varepsilon_0 W}{2d} V_d^{\ 2} . \tag{3.23}$$

The negative sign of the force indicated that the lateral force applied on the movable plate pulls the plates for more overlapping area and eliminate the misalignment.

Also we can see from Equation (3.23) that the force is independent of the overlapping distance x, so that the force is constant with the movement of the plate, and the lateral electrostatic force keeps constant when width, W, of the plates is scaled down with the distance, d.

By comparing the lateral electrostatic force F_{el} with the normal electrostatic force F_{en}, we have $|F_{en}| / |F_{el}| = L / d$. Typically, F_{en} is larger than F_{el}, as L is usually larger than d.

3.2.4 Comb Driving

Lateral electrostatic driving has its advantage over perpendicular driving: there is no pull-in effect to be worried about; and the electrostatic driving force is independent of the displacement of plates. However, lateral driving force is relatively small compared with perpendicular driving. Therefore, we use comb finger structure to increase the driving force. A comb actuator is shown in Figure 3.7.

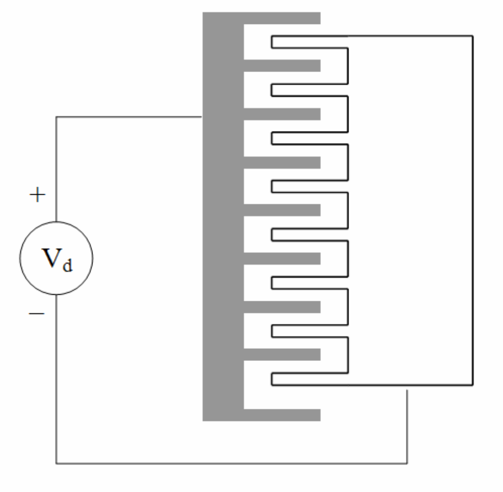

Figure 3.7 A basic comb actuator

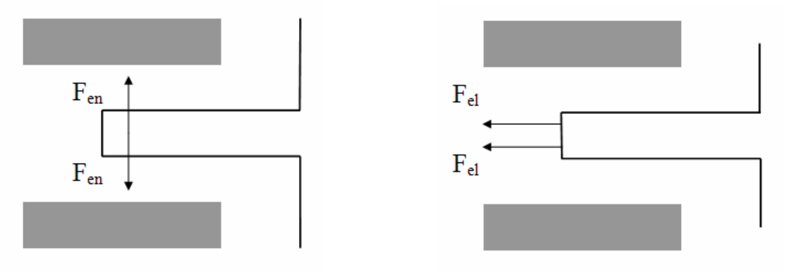

(a) (b)

Figure 3.8 Electrostatic driving force on one comb finger: (a) perpendicular force; (b) lateral force

Comb driving actuators make use of lateral electrostatic driving force to activate the movable mass, so we need to eliminate the effect of normal force. Stationary electrodes are arranged symmetrically on both sides of each movable comb finger, so that the normal driving forces from both sides which are equal in magnitude and opposite in direction, cancel out each other. The net electrostatic force in vertical direction is zero, as shown in Figure 3.8(a). There is no vertical movement.

However, the lateral driving forces from both side electrodes, which are equal in magnitude and same in direction, will not cancel out. Therefore, the net electrostatic force in horizontal direction is not zero, as shown in Figure 3.8(b). The movable fingers are activated towards left in horizontal direction.

From the previous discussion, the lateral electrostatic driving force can be expressed as:

$$F_{el} = \frac{\varepsilon_0 t V_d^{\ 2}}{2d}. \tag{3.24}$$

Here, we replace the plate width W with thickness of the comb finger t, because the comb finger can be treated as a vertical plate. Then, for each comb finger, the total lateral force is sum of lateral force from both top and bottom electrodes, which is $2F_{el}$. Finally, for a comb driving actuator having N finger groups, the total lateral force is

$$F_{el\_total} = 2NF_{el} = \frac{N\varepsilon_0 t V_d^{\ 2}}{d}. \tag{3.25}$$

We can see that the lateral electrostatic force increased by $2N$ in a comb driving actuator.

3.2.5 Push-pull Driving

For a structure forced can be applied on the movable mass from both sides, a push-pull driving scheme is often considered as the best solution for driving. The comb resonator, shown in Figure 3.9, is a typical structure suitable for push-pull driving.

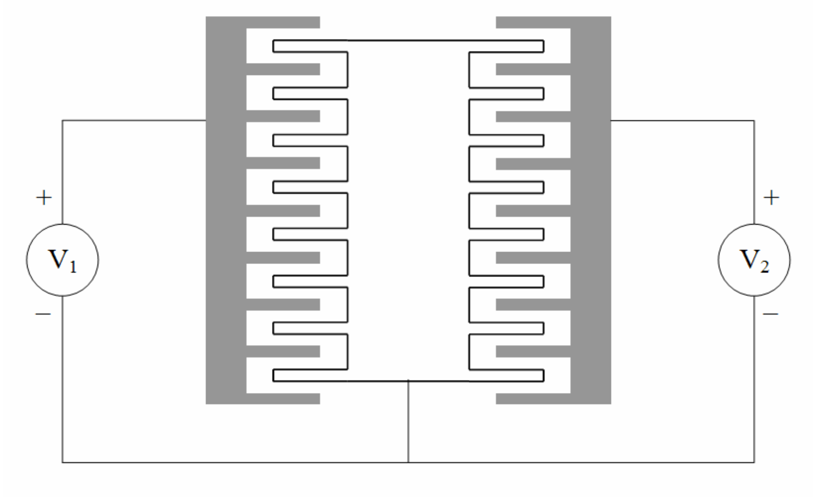

Figure 3.9 A push-pull comb actuator

The driving voltage on the left side, V_1, and the right side, V_2, are given below:

$$V_1 = V_d + V_0 \cos wt\,,$$
$$V_2 = V_d - V_0 \cos wt\,. \tag{3.26}$$

According to Equation (3.25), the driving force towards left, F_1, and the driving force towards right, F_2, are

$$F_1 = \frac{N\varepsilon_0 t V_1^2}{d}\,,$$
$$F_2 = \frac{N\varepsilon_0 t V_2^2}{d}\,. \tag{3.27}$$

Therefore, the total driving force towards left is

$$\begin{aligned} F_{total} = F_1 - F_2 &= \frac{N\varepsilon_0 t}{d}(V_1^2 - V_2^{\,2}) \\ &= \frac{N\varepsilon_0 t}{d}((V_d + V_0 \cos wt)_1^{\,2} - (V_d - V_0 \cos wt)^2) \\ &= \frac{4N\varepsilon_0 t}{d} V_d V_0 \cos wt\,. \end{aligned} \tag{3.28}$$

From Equation (3.28), we can see that the total driving force has no DC component, but only AC component, and is in a sinusoidal format. Therefore, the movable mass vibrates around the equilibrium point, forming an actuator. The driving force and the vibration amplitude can be adjusted by changing either V_d or V_0. The push-pull comb driving technique has been widely used in MEMS gyroscope design.

3.3 Capacitive Sensing

There are many kinds of MEMS sensing techniques: capacitive sensing, piezoresistive sensing and electromagnetic sensing, etc. Among them, capacitive sensing is the most popular one.

Although capacitive sensing suffers from high electromagnetic interference and increased complexity of the measurement electronics for miniaturized structure, capacitive sensing has some successful applications in MEMS industry. It has many attractive features for MEMS: in most micromachining technologies, minimal additional process is needed, capacitors operate both as sensors and actuators, excellent sensitivity has been demonstrated, the transduction mechanism is intrinsically insensitive to temperature, the sensitivity of the sensor keeps constant with the scale-down of the structure, etc. Thanks to the rapid progress in sensing techniques and the integration of micro mechanical structures with microelectronics, capacitive sensing has gained its dominating position in MEMS.

3.3.1 Parallel-plate Capacitive Sensing

Capacitive sensors use the electrical property of "capacitance" to make measurements. Capacitance is a property that exists between any two conductive surfaces within some reasonable proximity (see Figure 3.10).

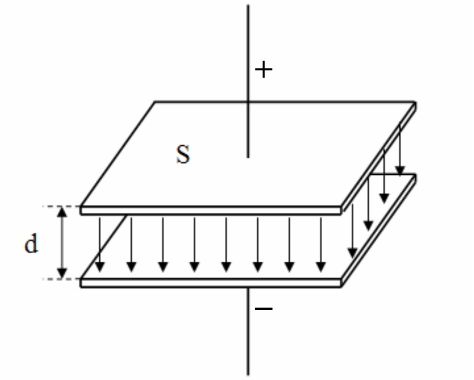

Figure 3.10 A capacitor form by two conductive surfaces

The capacitance can be expressed as:

$$C = \frac{\varepsilon S}{d}, \tag{3.29}$$

where d is the gap distance between the two surfaces; S is the overlapped area of the two surfaces; and ε is the electric constant. A change in gap distance d, or a change in the overlapped area S will cause a change in capacitance. By measuring this capacitance change, we know the value of the physical stimulus.

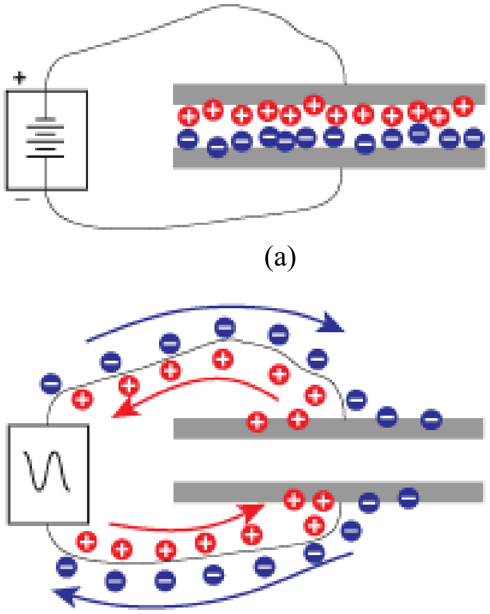

(a)

(b)

Figure 3.11 Applying AC voltage on a capacitor

When a voltage is applied to the conductors, an electric field is created between them causing positive and negative charges to collect on each object (see Figure 3.11(a)). If the polarity of the voltage is reversed, the charges will also reverse.

Then an alternating voltage is applied which causes the charges to continually reverse their positions. The moving of the charges creates an alternating electric current which is detected by the sensor (see Figure 3.11(b)). The amount of current flow is determined by the capacitance, and the capacitance is determined by the area and proximity of the conductive objects. This is basically how the capacitance is measured.

Capacitive sensing gained its popularity in MEMS design, because it is simple for fabrication, having low cost and very low power consumption. It is not susceptible to temperature change, thus having relative high stability. When used with electrostatic actuation, capacitive sensing may form a possible close-loop feedback.

However, it also has disadvantages. Capacitive sensing usually requires high resolution circuit, because capacitance in MEMS is normally very small (static capacitance is in the scale of pF(10^{-12}F), and capacitance change is in the scale of fF(10^{-15}F)). Capacitive sensing is vulnerable to parasitic capacitances, therefore glass substrate (SOI) is recommended. Capacitive sensing is also vulnerable to EMI (Electro-Magnetic Influence).

3.3.2 Differential Capacitive Sensing

Differential capacitive sensing technique is developed to eliminate the noise introduced by environment. A differential capacitor sensor consists of central movable plate with independent fixed electrodes on both top and bottom, as shown in Figure 3.12.

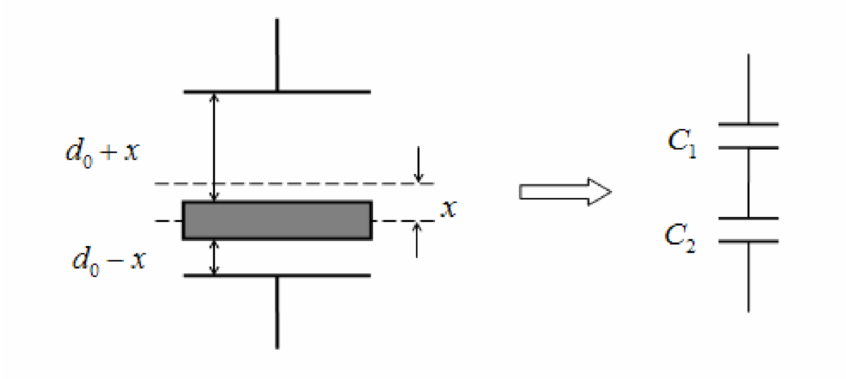

Figure 3.12 A differential capacitance pair

The static sensing capacitance of the differential capacitive sensor is

$$C_0=\frac{\varepsilon S}{d_0}, \tag{3.30}$$

where ε is the dielectric constant of air; S is the overlapped area of middle movable plate and the electrodes; d_0 is the static capacitance gap between central mass and electrode.

If there is no external force applied to the central movable plate, the plate stays in the middle of the two electrodes, and therefore the top capacitance, C_1, and bottom capacitance, C_2, are

$$C_1=C_2=C_0. \tag{3.31}$$

If there is an external force making the central mass move downward by x, as shown in Figure 3.12. The top capacitance, C_1, and bottom capacitance, C_2, are changed to

$$\begin{aligned} C_1&=\frac{\varepsilon S}{d_0+x},\\ C_2&=\frac{\varepsilon S}{d_0-x}. \end{aligned} \tag{3.32}$$

Under small deflection approximation $x \ll d_0$,

$$\begin{aligned} C_1&=\frac{\varepsilon S}{d_0+x}=\frac{\varepsilon S}{d_0\left(1+x/d_0\right)}\approx\frac{\varepsilon S}{d_0}\left(1-\frac{x}{d_0}\right),\\ C_2&=\frac{\varepsilon S}{d_0-x}=\frac{\varepsilon S}{d_0\left(1-x/d_0\right)}\approx\frac{\varepsilon S}{d_0}\left(1+\frac{x}{d_0}\right). \end{aligned} \tag{3.33}$$

The differential capacitance change ΔC is

$$\Delta C=C_2-C_1=\frac{\varepsilon S}{d_0}\cdot\frac{2x}{d_0}=\frac{2x}{d_0}C_0. \tag{3.34}$$

From Equation (3.34), we can see that for small deflection approximation, differential capacitance change is in direct proportion to the displacement of the movable plate. That means we can use differential capacitance change to measure the displacement of the movable plate.

3.3.3 Differential Capacitive Sensing Circuit

With a differential sensing structure, the displacement of the movable plate can be measured using a opposite excitation circuit as shown if Figure 3.13.

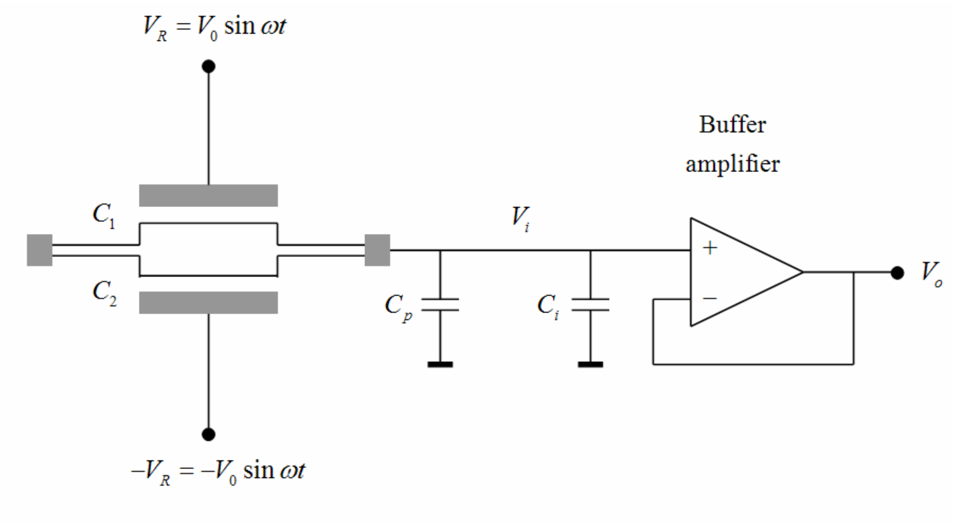

Figure 3.13 A differential capacitive sensing circuit

In Figure 3.13, C_1 is the capacitance between movable plate and the top electrode; C_2 is the capacitance between movable plate and the bottom electrode; C_p is the parasitic capacitance and C_i is the input capacitance of the buffer amplifier.

The measurement of capacitance is made by the two equal amplitude, out-of-phase sinusoidal excitation signals, $+V_R$ and $-V_R$, with the same frequency ω. When C_1 and C_2 are exactly the same, the input voltage of the amplifier is zero. When C_1 and C_2 are different, the input voltage, $-V_R$, of the buffer amplifier can be found by the condition of zero input current of the amplifier:

$$(V_R - V_i) \cdot C_1 = (V_R + V_i) \cdot C_2 + V_i (C_p + C_i) . \tag{3.35}$$

Thus, the signal voltage on the movable plate is

$$V_i = \frac{C_1 - C_2}{C_1 + C_2 + C_p + C_i} V_R . \tag{3.36}$$

For small displacement x, we have

$$V_i = \frac{2 C_0 V_R \tilde{x}}{2C_0 + (C_p + C_i)(1 - \tilde{x}^2)} . \tag{3.37}$$

Here, we use $\tilde{x} = x / d$ for convenience.

As V_i is dependent on C_p and C_i, the accuracy and stability of the measurement deteriorates. To alleviate this problem, a feedback scheme can be used as shown in Figure 3.14.

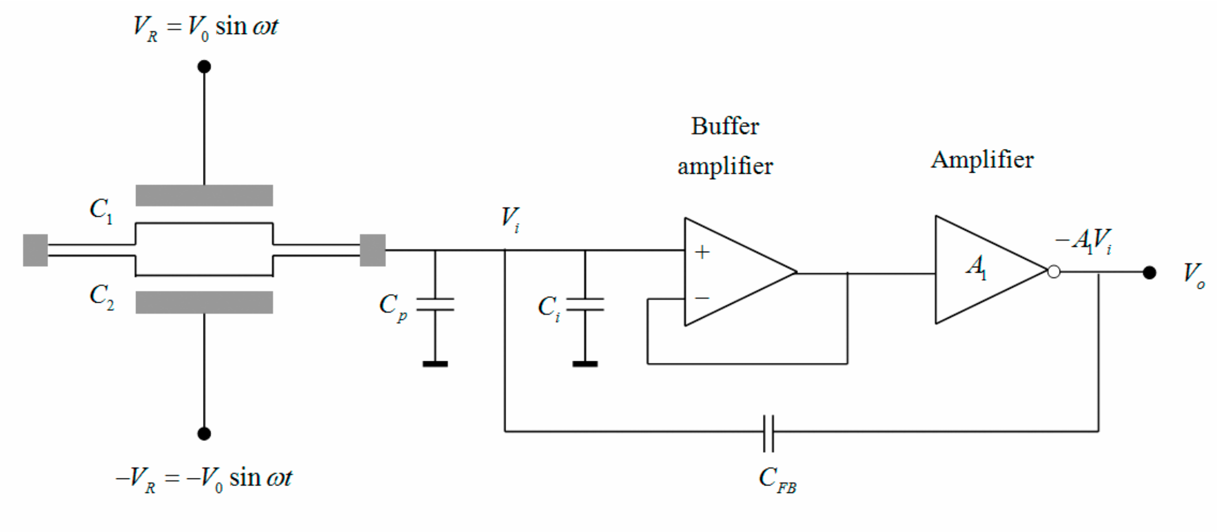

Figure 3.14 A differential capacitive sensing circuit with capacitive feedback

In Figure 3.14, C_{FB} is a feedback capacitor. By using the condition of current balance as before, we have

$$(V_R - V_i)\cdot C_1 = (V_R + V_i)\cdot C_2 + V_i(C_p + C_i) + (V_i + A_1V_i)\cdot C_{FB}\,. \tag{3.38}$$

Thus, the signal voltage on the movable plate is

$$V_i = \frac{(C_1 - C_2)\cdot V_R}{C_1 + C_2 + C_p + C_i + (1 + A_1)\cdot C_{FB}}\,. \tag{3.39}$$

where A_1 is the open-loop gain of the amplifier A_1. The output of the circuit is

$$V_o = -A_1V_i = \frac{-A_1(C_1 - C_2)\cdot V_R}{C_1 + C_2 + C_p + C_i + (1 + A_1)\cdot C_{FB}}\,. \tag{3.40}$$

If A_1 is large enough, we have the approximate result

$$V_o = -\frac{C_1 - C_2}{C_{FB}}V_R \approx -\frac{2C_0\tilde{x}}{C_{FB}(1-\tilde{x}^2)}V_R\,. \tag{3.41}$$

The output V_o is linearly dependent on the differential capacitance, $C_1 - C_2$, but not dependent on the parasitic capacitance C_p.

Here, we need to mention that the two excitation signals, $+V_R$ and $-V_R$, which are connected to the top and bottom electrodes are sinusoidal signals, where

$$V_R = V_0 \sin\omega t\,. \tag{3.42}$$

So the two input signals are equal in amplitude, opposite in phase. As a consequence, the output voltage V_o is also a sinusoidal signal (see Figure 3.15). The AC signal is used instead of DC voltage here, because AC signal is easy for detection than DC signal, especially, in our case, output signal is relatively small.

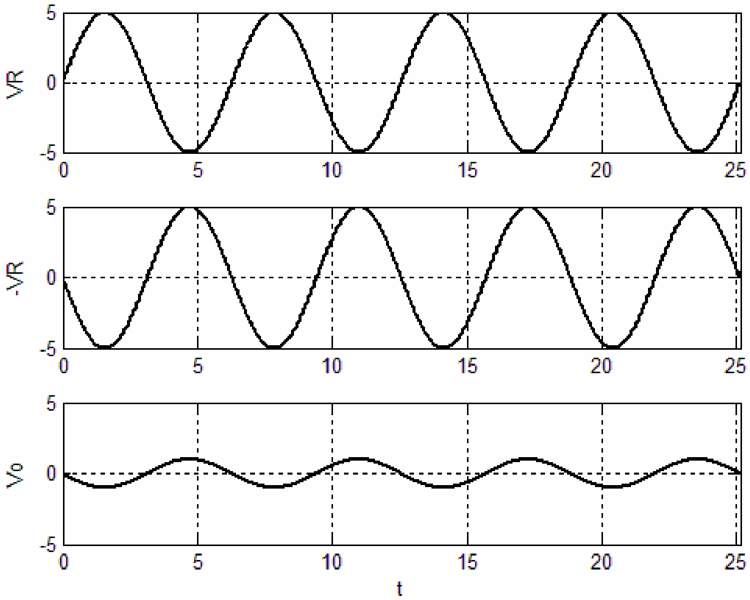

Figure 3.15 Input and output voltage of the differential capacitive sensing circuit

3.4 Resonant Frequency

Silicon mechanical structures with a mass and beams are the most commonly used parts for MEMS gyroscopes. Mechanics of beam and mass structures will be studied in this section according to the theory of elasticity. The most important parameters in the beam and mass structure are spring constant and resonant frequency.

3.4.1 Spring-mass Model

Most MEMS beam-mass structures can be simplified as a spring-mass model as shown in Figure 3.16.

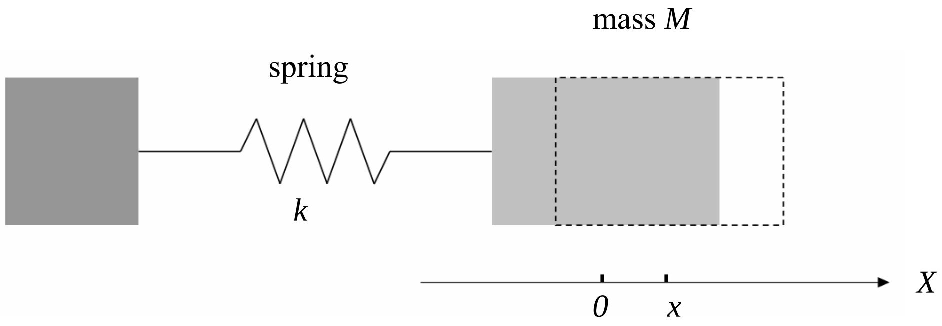

Figure 3.16 A spring-mass model

The origin of the x-axis is at the balance position of the mass center. A displacement of the mass from its balance position, x, causes a recovery force acting on the mass by the spring. According to Hook's law,

$$F = -kx\,, \tag{3.43}$$

where k is the elastic constant of the spring. The negative sign implies that the force is pointing back to the origin of the x-axis. If there is no other force acting on the mass, the differential equation for the mass movement is

$$M\dot{x} = -kx\,. \tag{3.44}$$

Let $\omega^2 = k / M$, we have

$$\dot{x} + \omega^2 x = 0\,. \tag{3.45}$$

The general solution to Equation (3.44) is a sinusoidal vibration of the mass

$$x = A\sin(\omega t + \alpha)\,, \tag{3.46}$$

where ω is the radial frequency of the vibration; A is the amplitude of the vibration; and α is a phase lag angle. The radial frequency ω is only decided by the structure parameter k and M :

$$\omega = \sqrt{\frac{k}{M}}\,. \tag{3.47}$$

The amplitude A and the phase lag α can be decide by the initial conditions of the system. For example, for $x = x_0$ and $\dot{x} = v_0$ at $t = 0$, we have

$$\begin{aligned} A &= \sqrt{{x_0}^2 + \left(\frac{v_0}{\omega}\right)^2}\,, \\ \alpha &= \arctan\left(\frac{x_0\omega}{v_0}\right). \end{aligned} \tag{3.48}$$

The vibration frequency, ω, can also be found by the general principle of energy conservation of the system. As the vibration of the spring-mass system can be described by Equation (3.46), the potential energy of the system is

$$E_P = \frac{1}{2}kx^2 = \frac{1}{2}A^2 k\sin^2\left(\omega t + \alpha\right), \tag{3.49}$$

and the kinetic energy of the system is

$$E_K = \frac{1}{2}M\dot{x}^2 = \frac{1}{2}A^2\omega^2 M\cos^2\left(\omega t + \alpha\right). \tag{3.50}$$

The total energy, E, of the system is

$$E = E_P + E_K\,. \tag{3.51}$$

When $\omega t + \alpha = 0$, we have $E = E_{K,\max} = MA^2\omega^2 / 2$; and when $\omega t + \alpha = \pi / 2$, we have $E = E_{P,\max} = kA^2 / 2$. According to the principle of energy conservation, $E_{K,\max} = E_{P,\max} = E$, we have

$$\frac{1}{2}MA^2\omega^2 = \frac{1}{2}kA^2\,. \tag{3.52}$$

This leads to the same result as that given by Equation (3.47).

A spring-mass system containing more than one spring is similar to the basic model above. If two springs connected in series to a mass as shown in Figure 3.17, the total spring constant of the spring-mass system is

$$k_{total} = \frac{k_1 k_2}{k_1 + k_2}. \tag{3.53}$$

If two springs connected in parallel to a mass as shown in Figure 3.18, the total spring constant of the spring-mass system is

$$k_{total} = k_1 + k_2. \tag{3.54}$$

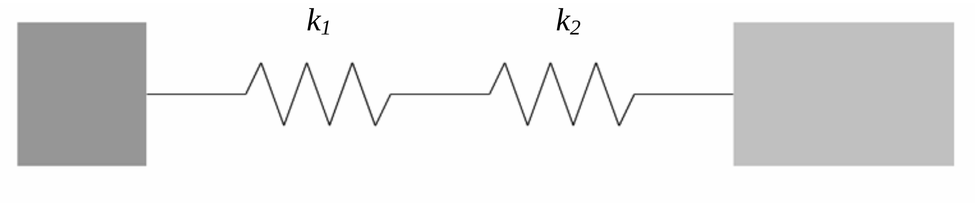

Figure 3.17 Two springs connected in series

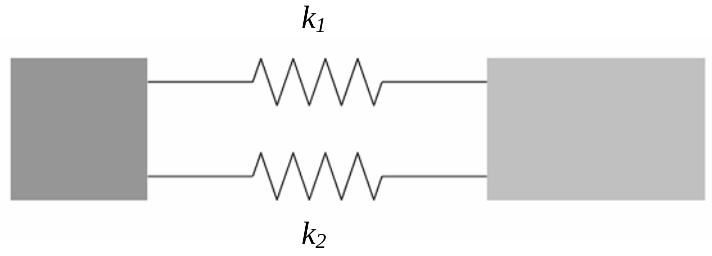

Figure 3.18 Two springs connected in parallel

3.4.2 Young's Modulus and Moment of Inertia

There are two very important parameters in study of spring-mass structure in MEMS. They are Young's modulus and moment of inertia.

Young's modulus is a term shows the elastic properties of a material, determining how much it will compress under a given amount of external pressure. The ratio of the change in pressure to the fractional volume compression is called the Young's modulus of the material.

A representative value of Young's modulus for silicon is

$$E = 170GPa. \tag{3.55}$$

Young's modulus is the ratio of stress, which has units of pressure, to strain, which is dimensionless; therefore Young's modulus itself has a unit of pressure.

The Moment of Inertia is a term used to describe the capacity of a cross-section to resist bending. The Moment of Inertia is an important value which is used to determine the state of stress in a section, to calculate the resistance to buckling, and to determine the amount of deflection in a beam. For example, if a designer is given a certain set of constraints on a structural problem (i.e., loads, spans and end conditions) a required value of the moment of inertia can be determined. Then, any structural element which has at least that specific moment of inertia will be able to be utilized in the design. Another example could be in the inverse were true: a specific element is given in a design. Then the load bearing capacity of the element could be determined.

Calculus is ordinarily used to find the moment of inertia of an irregular section. However, a simple formula has been derived for a rectangular section which will be mostly used in gyroscope design.

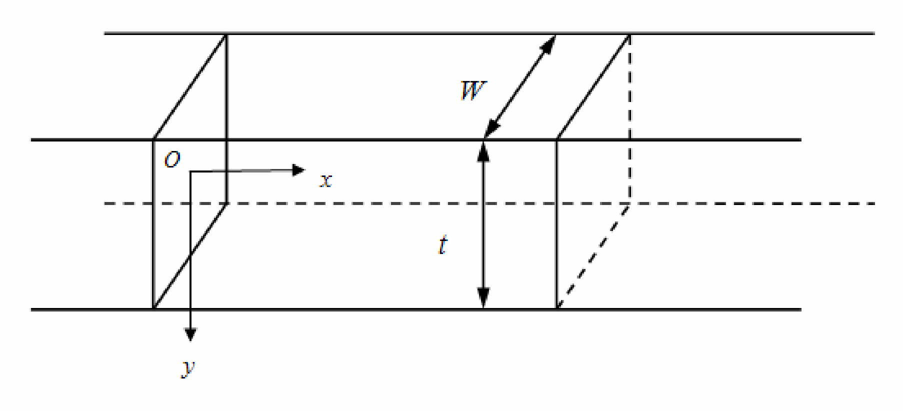

Figure 3.19 An element section of a beam

Consider a thin straight beam with a rectangular cross section of width W and thickness t. The length of the beam L is much larger than W and t. If the beam is bent along z-direction, the moment of inertia can be expressed as

$$I = \frac{1}{12} W t^3 . \tag{3.56}$$

From equation (3.56), we can see that $I \propto W$ and $I \propto t^3$. The moment of inertia depends more on the thickness of the beam, less on the width of the beam.

Inside a bent beam, there exist internal forces across its cross sections. This internal moment of the forces across a cross section of the beam is called bending moment. With young's modulus of material and moment of inertia of the beam, bending moment is defined as

$$M(x) = \pm E I y''(x) . \tag{3.57}$$

Bending moment is positive in sign if the beam is bent up; and it is negative if the beam is bent down.

There is also a stress or strain inside a bent beam. The stress at position (x, y) is defined as

$$T(x, y) = -E y y''(x) . \tag{3.58}$$

For the bending-up beam, we have $y''(x) < 0$. At any position $y > 0$, the stress is positive, i.e., the layer is stretched; and vice versa.

3.4.3 Cantilever Beam Structure

Consider a rectangular cantilever beam with a concentrated end loading, as shown in Figure 3.20.

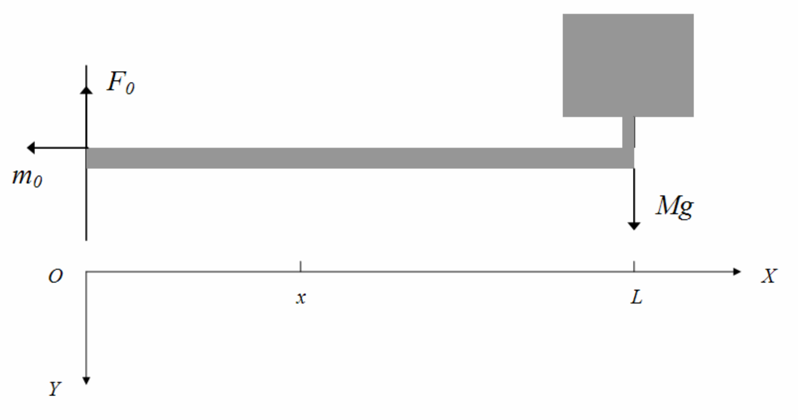

Figure 3.20 Cantilever beam with a concentrated end loading

The length, the width and the thickness of the beam are L, W and t, respectively. Let F be the loading force caused by a mass, M, attached to the free end of the beam and the gravitational acceleration, i.e., $F = Mg$. Also assume that the end mass, M, is much larger than the beam mass, so that the gravitational force of the beam can be neglected. To balance the loading force, F, there must be a supporting force, F_0, acting on the beam at the clamped end. The force balance in the y-direction requires that $F_0 = F$. In the meantime, there must be a restrictive bending moment, m_0, at the clamped end of the beam to balance the bending moment caused by the loading force, F.

The force moment produced by the loading force against the clamped end is FL, in a clockwise direction. For the balance of bending moments, the restrictive bending moment, m_0, must be equal to FL, in a counter-clockwise direction. Generally, m_0 has to be found using equation solving.

Looking at position x as shown in Figure 3.20, the bending moment on the left is $(-m_0 + F_0 x)$, and the bending moment on the right side is $-F(L-x)$. As a matter of fact, the bending moment on the left is equal to that on the right, i.e., $M(x) = -F(L-x)$. Therefore, the differential equation for $y(x)$ is

$$-EIy''(x) = -F(L-x)\,. \tag{3.59}$$

The boundary conditions for the problem are

$$y(0) = 0\,,\ y'(0) = 0\,,\ y''(L) = 0\,. \tag{3.60}$$

The solution to Equation (3.58) and (3.59) is

$$y(x) = \frac{F(3L-x)x^2}{6EI} = \frac{2Mg(3L-x)x^2}{EWt^3}\,. \tag{3.61}$$

The maximum displacement at the free end (i.e., at $x = L$) is

$$y_{\max} = y(L) = \frac{FL^3}{3EI} = \frac{4MgL^3}{EWt^3}. \tag{3.62}$$

If the beam is considered as a spring, its spring constant is

$$k = \frac{EWt^3}{4L^3}. \tag{3.63}$$

The stress on the top surface of the beam (at $y = -t/2$) is

$$T(x, y) = -E\left(-\frac{t}{2}\right)y''(x) = \frac{Ft(L-x)}{2I} = \frac{6Mg(L-x)}{Wt^2}. \tag{3.64}$$

The stress has a maximum at $x = 0$ and decreases linearly to zero at $x = L$. From Equation (3.64), the maximum stress at $x = 0$ is

$$T_{\max} = \frac{FtL}{2I} = \frac{6MgL}{Wt^2}. \tag{3.65}$$

By substituting Equation (3.63) into the Equation (3.47), the radial frequency of the cantilever beam structure is

$$\omega = \sqrt{\frac{EWt^3}{4L^3M}}. \tag{3.66}$$

Therefore, the vibration frequency of the beam-mass system is

$$f = \frac{1}{4\pi}\sqrt{\frac{EWt^3}{L^3M}}. \tag{3.67}$$

Note that the vibration frequency is only a function of structural parameters.

3.4.4 Double-clamped Beam Structure

The structure of two clamped beams supporting a central mass is often used for inertial sensors (such as accelerometers and gyroscopes), resonators and mechanical actuators (such as switches). A double-clamped beam with a central mass is shown in Figure 3.21.

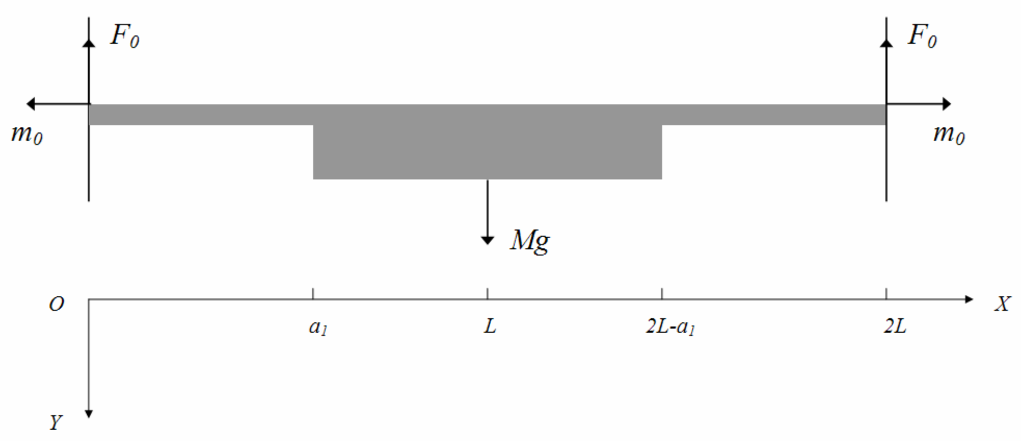

Figure 3.21 Double-clamped beam with a central mass

As a typical condition, the central mass is much wider and thicker than the beams so that the bending of the mass can be neglected. If the loading of the beam-mass structure is its own weight in the y-direction, the displacement of the mass is piston-like due to the symmetry of the structure in x-direction. Therefore, only a half of the structure has to be considered. Under the condition that the mass of the beams is much smaller that that of the central mass, or the left beam, the displacement is

$$-EIy''(x) = \frac{Mg}{2}x - m_0 . \tag{3.68}$$

where m_0 is the restrictive bending moment to be determined and m_0 is the total mass of the beam-mass structure. The boundary conditions for the equation are

$$y(0) = 0 ,\ y'(0) = 0 ,\ y'(a_1) = 0 ,\ y''(\frac{1}{2}a_1) = 0 . \tag{3.69}$$

From Equation (3.68) and (3.69), we have $m_0 = \frac{1}{4}Mga_1$. Therefore, the displacement of the left beam is

$$y(x) = \frac{Mg}{EWt^3}x^2\left(\frac{3}{2}a_1 - x\right). \tag{3.70}$$

The displacement of the central mass is

$$y(a_1) = \frac{Mga_1^3}{2EWt^3} . \tag{3.71}$$

If the beam is considered as a spring, its spring constant is

$$k = \frac{2EWt^3}{a_1^3} . \tag{3.72}$$

The stress on the top surface of the beam is

$$T(x) = \frac{3Mg}{Wt^2}\left(\frac{1}{2}a_1 - x\right). \tag{3.73}$$

The stress has a positive maximum at $x = 0$ and decreases linearly to a negative maximum at $x = a_1$. The values for both the positive and negative maximums are the same. From Equation (3.73), the maximum stress at $x = 0$ is

$$T_{\max} = \frac{3Mga_1}{2Wt^2} . \tag{3.74}$$

By substituting Equation (3.72) into the Equation (3.47), the radial frequency of the double-clamped beam structure is

$$\omega = \sqrt{\frac{2EWt^3}{Ma_1^3}} . \tag{3.75}$$

Therefore, the vibration frequency of the beam-mass system is

$$f = \frac{1}{2\pi}\sqrt{\frac{2EWt^3}{Ma_1^3}} . \tag{3.76}$$

3.4.5 Complex Beam Structures

In some designs, we use folded-beam structure to increase the sensitivity of the device (see Figure 3.22). A folded-beam structure is equivalent to N beam sections connected in series. Therefore, the total spring constant of the folded-beam is

$$k_{total} = \frac{k}{N}, \tag{3.77}$$

where k is the spring constant of one beam section.

Figure 3.22 Folded-beam structure

In some other designs, we use parallel-beam structure to increase the stability of the device (see Figure 3.23). A parallel-beam structure is equivalent to N beam sections connected in parallel. Therefore, the total spring constant of the folded-beam is

$$k_{total} = Nk, \tag{3.78}$$

where k is the spring constant of one beam section.

Figure 3.23 Parallel-beam structure

3.4.6 Rayleigh-Ritz Method

According to the previous discussion, the vibration frequency of the system with a concentrated mass and a spring can be calculated easily. However, the simple relations can not be used to calculate the vibration frequency for a system with a distributed mass. Based on the general principle of energy conservation, a more general method called the Rayleigh-Ritz method has been developed for calculating the vibration frequency of systems with distributed masses. Here we will establish the Rayleigh-Ritz method for a uniform beam with a rectangular cross section. The result is applicable to many micro structures including MEMS gyroscopes.

First, we consider the energy stored in an elemental section, dx, at position x on the beam as shown in Figure 3.24. The coordinate system is taken as before with the x-axis along the length direction of the beam and the y-axis in the thickness direction. The displacement of the beam in the y-direction is a function of x, $y(x,T)$. Note here we use T as a time variable to distinguish it form beam thickness t.

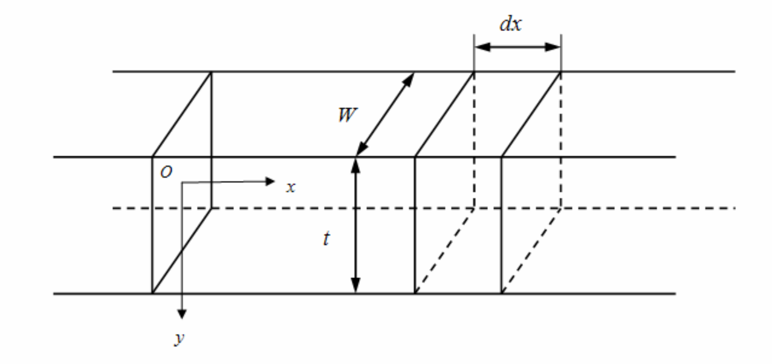

Figure 3.24 Analysis of potential energy in a beam

For a thin layer of thickness dy in the section, the areas on its front and rear ends are Wdy (where W is the width of the beam) and the normal forces on both ends are

$$df = -Eyy''(x,T)Wdy\,. \tag{3.79}$$

The elongation of the layer in the x-direction due to the forces is

$$\Delta(dx) = -yy''(x,T)dx\,. \tag{3.80}$$

The potential energy stored in the layer of dy caused by the bending deformation is

$$\Delta(dE_P) = \frac{1}{2} df\,\Delta(dx)\,. \tag{3.81}$$

From Equation (3.80), the potential energy in the layer of dy is

$$\Delta(dE_P) = \frac{1}{2} Ey^2 y''^2(x,T)Wdxdy\,. \tag{3.82}$$

The potential energy stored in the section, dy, of the beam is

$$dE_P = \frac{1}{2} Ey''^2(x,T)\left(\int_{-t/2}^{t/2} Wy^2 dy\right)dx = \frac{1}{2} Ey''^2(x,T)Idx\,. \tag{3.83}$$

For the whole beam with a length L, the total potential energy caused by the bending is

$$E_P = \frac{1}{2}\int_0^L EIy''^2(x,T)dx\,. \tag{3.84}$$

The kinetic energy of the elemental section dx is

$$dE_K = \frac{1}{2}\rho W t dx \left(\frac{dy}{dT} \right)^2 . \tag{3.85}$$

And, the kinetic energy of the whole beam is

$$E_K = \int_0^L \frac{1}{2}\rho W t \left(\frac{dy}{dT} \right)^2 dx . \tag{3.86}$$

In general, the vibration of a beam structure can be described by

$$y(x,T) = \sum_{n=0}^{\infty} c_n Y_n(x,T) , \tag{3.87}$$

where $Y_n(x,T)$ is the wave function of the nth vibration mode with a sinusoidal vibration of radial frequency ω_n and a shape function $Y_n(x)$:

$$Y_n(x,T) = Y_n(x)\sin(\omega_n T + \alpha_n) . \tag{3.88}$$

For the vibration mode designated by subscript n, the potential energy is

$$E_P = \frac{1}{2}c_n{}^2 \int_0^L EI[Y_n''(x)]^2 \sin^2(\omega_n T + \alpha_n) dx , \tag{3.89}$$

And the kinetic energy of the mode is

$$E_K = \frac{1}{2}c_n{}^2 \int_0^L \rho W t Y_n{}^2(x)\omega_n{}^2 \cos^2(\omega_n T + \alpha_n) dx . \tag{3.90}$$

By the principle of energy conservation, i.e., $E_{P\max} = E_{K\max} = E$, the vibration frequency of the mode can be found by the equation below:

$$\omega_n{}^2 = \frac{\int_0^L EI Y_n''^2(x) dx}{\int_0^L \rho W t Y_n{}^2(x) dx} . \tag{3.91}$$

Equation (3.91) can be used for a beam with non-uniform cross section if the area of the cross section $A(x)$ is used to substitute for Wt in the denominator.

$$\omega_n{}^2 = \frac{\int_0^L EI Y_n''^2(x) dx}{\int_0^L \rho A(x) Y_n{}^2(x) dx} . \tag{3.92}$$

This is the well-known Rayleigh's quotient and the method for the vibration frequency is referred to as Rayleigh-Ritz method.

With Rayleigh's quotient, the vibration frequency of a specific vibration mode can be found if the shape function of the vibration mode is known. The problem is that it is generally quite difficult to find the shape functions for a structure. However, the vibration frequency for the fundamental vibration mode (with the lowest vibration frequency) can be found by Rayleigh's quotient with high accuracy when a static displacement function $y(x)$ is used as an approximation for the shape function. In most cases, the basic vibration mode plays an important role and the effect of the higher vibration modes can be neglected as their frequencies are much higher than that of the basic vibration mode.

For some higher vibration modes, if a proper approximation of shape function $Y_n(x)$ can be found (based on the information on boundary conditions, nodes, etc.), the vibration frequencies can also be found by Rayleigh's quotient with a reasonably high accuracy.

As the shape function $Y_n(x)$ used for the vibration frequency calculation by Rayleigh's quotient is an approximation of the real eigenfunction, the result is always higher than the actual eigenvalue of the corresponding eigenfunction. However, the approximation is usually very good for the fundamental vibration frequency. The results for the first and second higher harmonics can also be quite good approximations if reasonable shape functions are assumed.

3.5 Damped and Forced Vibration

For the free vibration as described in last section, there is no need for the system to do work against resistive forces so that its total energy remains constant at any time. In practice, the vibration of a real system is always resisted by dissipative forces, such as air viscosity, friction, acoustic transmission, internal dissipation, etc. The system thus does positive work. The energy for the work is subtracted from the vibration energy and is usually converted into thermal energy. Therefore, damping is the process whereby energy is taken from the vibration system.

Generally, damping is inevitable in any system. For example, the internal friction in a spring (or flexure) is always dissipative and transforms part of the vibration energy into thermal energy in each cycle. Another common cause of damping is the viscosity of the surrounding fluid such as air. The fluid exerts viscous forces on the moving object and opposes its movement through the fluid.

As a first order approximation, a damping force, F_d, is proportional to the speed of the movement: $F_d = -c\dot{x}$, where c is called the coefficient of damping force and the negative sign indicates that the force is opposite to the moving direction. A vibration system with damping is usually modeled in Figure 3.25. The damping effect is represented by a damper.

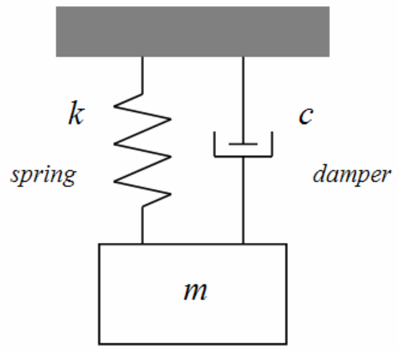

Figure 3.25 A simplified model for a vibration system with damping

Damping is a destructive factor in maintaining a vibration. In many cases, such as the MEMS gyroscope design, measures are taken to reduce damping so that the vibration can be maintained with a minimum energy supplement per cycle.

3.5.1 Vibration with Damping

For a damped vibration system as shown in Figure 3.25, the differential equation for the movement is the second-order differential equation

$$m\ddot{x} = -kx - c\dot{x}, \tag{3.93}$$

where m is the mass; k is the spring constant; and c is the coefficient of damping force. Or, we have

$$\ddot{x} + \frac{c}{m}\dot{x} + \frac{k}{m}x = 0. \tag{3.94}$$

Using ${\omega_0}^2 = \dfrac{k}{m}$ and $n = \dfrac{c}{2m}$, we have

$$\ddot{x} + 2n\dot{x} + {\omega_0}^2 x = 0. \tag{3.95}$$

where ω_0 is the radial frequency of the vibration system if there is no damping (i.e., a free vibration) and n is called the coefficient of damping. By letting $x = Ae^{\lambda t}$, we have

$$\lambda^2 + 2n\lambda + {\omega_0}^2 = 0. \tag{3.96}$$

The solutions to the equation are

$$\lambda_{1,2} = -n \pm \sqrt{n^2 - {\omega_0}^2}. \tag{3.97}$$

The performance of the system can be discussed according to the ratio between n and ω_0. The ratio $\zeta = n/\omega_0$ is known as the damping ratio of the system.

(1) Slight Damping (Under-damping)

If $n < \omega_0$, i.e., $\zeta < 1$, we have

$$\lambda_{1,2} = -n \pm i\sqrt{{\omega_0}^2 - n^2}. \tag{3.98}$$

The solution to Equation (3.95) is

$$x = Ae^{-nt}\sin(\sqrt{{\omega_0}^2 - n^2}\,t + \alpha). \tag{3.99}$$

Equation (3.99) indicates that the system will have an oscillation, but it differs from the free vibration in that: The vibration frequency is $\omega_d = \sqrt{{\omega_0}^2 - n^2} = \omega_0\sqrt{1^2 - \zeta^2}$, which is smaller than the free vibration frequency ω_0; and the amplitude of the vibration decays exponentially with time.

(2) Heavy Damping (Over-damping)

If $n > \omega_0$, i.e., $\zeta > 1$, we have

$$\lambda_{1,2} = -n \pm \sqrt{n^2 - {\omega_0}^2}, \tag{3.100}$$

and

$$x = e^{-nt}(c_1 e^{\sqrt{n^2 - {\omega_0}^2}t} + c_2 e^{-\sqrt{n^2 - {\omega_0}^2}t}). \tag{3.101}$$

Equation (3.101) indicates that there is no oscillation of the displacement; and the mass returns to its balanced position slowly.

(3) Critical Damping

If $n = \omega_0$, i.e., $\zeta = 1$, we have

$$\lambda_1 = \lambda_2 = -n = -\omega_0 , \tag{3.102}$$

And the special solution to Equation (3.95) is $x_1(t) = c_1 e^{-nt}$. Assuming a general solution of $x = A(t) x_1(t)$ and substituting it into Equation (3.95), we have $d^2 A / dt^2 = 0$. Therefore, the general solution to Equation (3.95) is

$$x = c_1 e^{-nt} (c_2 t + c_3) . \tag{3.103}$$

Equation (3.103) indicates that there is no oscillation in case of critical damping; but the time taken for the displacement to become virtually zero is a minimum.

Figure 3.26 shows the $x(t)$ for the three different damping conditions.

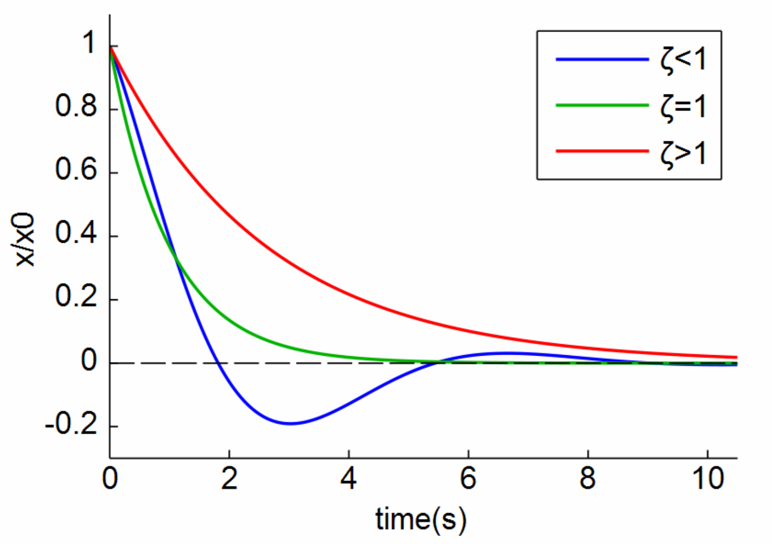

Figure 3.26 Amplitude attenuation of systems with different damping ratio

3.5.2 Vibration Driven by Step Force

For a spring-mass system, balanced position of the mass is taken as $x = 0$. With a constant force F_0 on the mass, the balanced position is $x_0 = F_0 / k$.

Now let us consider the time response of the system to a step force F_0. When the force is applied on the mass at $t = 0$, the mass moves from its original position, $x = 0$, towards its new balanced position, $x_0 = F_0 / k$. If the damping effect is negligible, the system will possess a total energy of $E = F_0 x_0$ when the mass arrives at x_0 due to the work done by the force. As the potential energy in this condition is $kx_0^2 / 2 = F_0 x_0 / 2$, the mass must have a kinetic energy $F_0 x_0 / 2$ at x_0. This means that the mass will move on after passing through x_0 until it reaches x', where the work done by the applied force equals the elastic potential energy

$$F_0 x' = \frac{1}{2} k x'^2 . \tag{3.104}$$

As $x' = 2x_0$ is not a balanced position, the mass will move back toward $x = 0$. In this way, the mass oscillates between 0 and $2x_0$. When the effect of damping is considered, the oscillation will die down and the mass will finally settle at $x = x_0$ when the excessive energy is completely consumed by the damping. Therefore, the response of the system to a step force is strongly dependent on the damping.

The process can be described by equation

$$m\ddot{x} + c\dot{x} + kx = F_0 . \tag{3.105}$$

As $F_0 = kx_0$, we have

$$m\ddot{x} + c\dot{x} + k(x - x_0) = 0 . \tag{3.106}$$

By letting $x_1 = x - x_0$, we have the differential equation for x_1

$$m\ddot{x}_1 + c\dot{x}_1 + kx_1 = 0 , \tag{3.107}$$

with the initial conditions

$$x_1\big|_{t=0} = -x_0 , \ \dot{x}_1\big|_{t=0} = 0 . \tag{3.108}$$

Therefore, the solutions to Equation (3.95) are applicable to Equation (3.107) and the initial conditions shown in Equation (3.108) can be used to determine the constants in the solutions. The analysis gives the following results:

(1) The Under-damping Conditions

In this condition, the system oscillates before it settles down. The expression for $x(t)$ is

$$x = x_0 \left(1 - \frac{e^{-\zeta\omega_0 t}}{\sqrt{1-\zeta^2}} \sin(\sqrt{1-\zeta^2}\,\omega_0 t + \alpha) \right), \tag{3.109}$$

where $\omega_0 = \sqrt{\frac{k}{m}}$ and $\alpha = \sin^{-1}\sqrt{1-\zeta^2}$.

(2) The Over-damping Conditions

In this condition, the system reaches its new balance position very slowly. The expression for $x(t)$ is

$$x = x_0 \left(1 - \frac{\zeta + \sqrt{\zeta^2 - 1}}{2\sqrt{\zeta^2 - 1}} e^{(-\zeta + \sqrt{\zeta^2 - 1})\omega_0 t} + \frac{\zeta - \sqrt{\zeta^2 - 1}}{2\sqrt{\zeta^2 - 1}} e^{(-\zeta - \sqrt{\zeta^2 - 1})\omega_0 t} \right), \tag{3.110}$$

(3) The Critical Damping Conditions

In this condition, the system moves to its new balanced position without oscillation, but faster than over-damping condition. The dependence of x on time is

$$x = x_0\left(1-(1+\omega_0 t)e^{-\omega_0 t}\right), \tag{3.111}$$

For example, curves for the different damping conditions are shown in Figure 3.27.

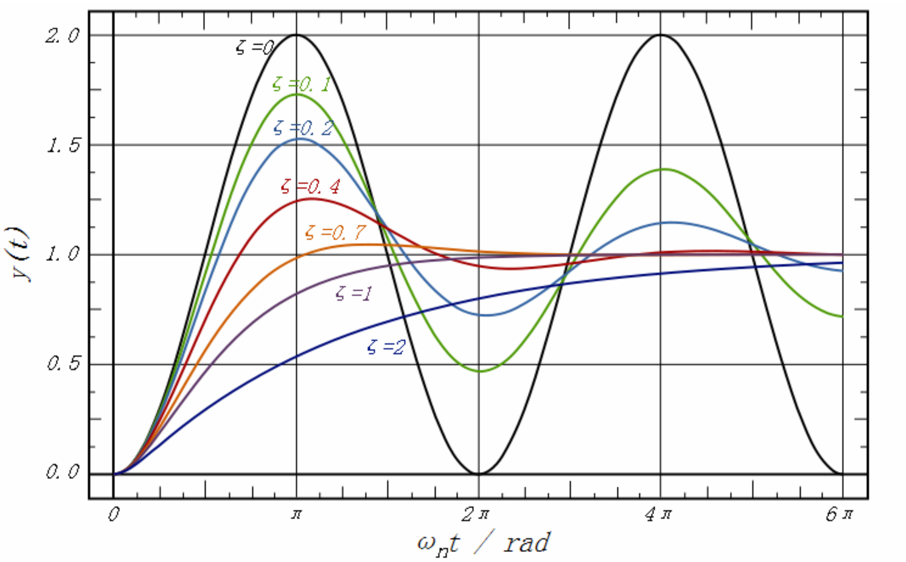

Figure 3.27 Response to a step force for different damping ratios

3.5.3 Vibration Driven by Periodic Force

Suppose that a spring-mass system is set to contiuous oscillation by a perioid driving force acitng on the mass. If the force is a sinusoidal one with a frequency of ω and an amplitude of F_0,

$$F = F_0 \sin(\omega t), \tag{3.112}$$

the differential equation for the system is

$$m\ddot{x} = -kx - c\dot{x} + F_0 \sin(\omega t). \tag{3.113}$$

The solution to Equation (3.113) takes form

$$x = x_1 + x_2. \tag{3.114}$$

where x_2 is a specific solution to Equation (3.113) and x_1 is a general solution to the homogeneous differential equation of the damped system, i.e., the equation for x_1 is

$$m\ddot{x}_1 + c\dot{x}_1 + kx_1 = 0. \tag{3.115}$$

The solution to Equation (3.115) is known to be a damped oscillation (for $n < \omega_0$)

$$x_1 = Ae^{-nt}\sin(\sqrt{\omega_0{}^2 - n^2}t + \alpha)\,. \tag{3.116}$$

We assume that x_2 is a stable oscillation

$$x_2 = B\sin(\omega t - \varphi)\,, \tag{3.117}$$

where B is the amplitude of the resulting vibration and φ is the phase lag of the vibration against the sinusoidal force. By substituting Equation (3.117) into Equation (3.113), we have

$$[B(\omega_0{}^2 - \omega^2) - f\cos\varphi]\sin(\omega t - \varphi) + (2nB\omega - f\sin\varphi)\cos(\omega t - \varphi) = 0\,, \tag{3.118}$$

where $f = F_0 / m$. To satisfy this equation, we have

$$\begin{gathered} B(\omega_0{}^2 - \omega^2) - f\cos\varphi = 0\,, \\ 2nB\omega - f\sin\varphi = 0\,. \end{gathered} \tag{3.119}$$

Therefore, the amplitude B and the phase lag φ are found to be

$$B = \frac{f}{\sqrt{(\omega_0{}^2 - \omega^2)^2 + 4n^2\omega^2}}\,, \tag{3.120}$$

$$\varphi = \arctan\frac{2n\omega}{\omega_0{}^2 - \omega^2}\,. \tag{3.121}$$

Thus, the solution to Equation (3.112) is

$$x = Ae^{-nt}\sin(\sqrt{\omega_0{}^2 - n^2}t + \alpha) + B\sin(\omega t - \varphi)\,. \tag{3.122}$$

The solution given in Equation (3.122) indicates that, in the early stages, beats occur due to forced vibration and damped vibration, giving rise to transient oscillations, which are usually short-lived and can be ignored in most cases. We will only consider what happens when conditions are steady.

(1) Vibration Frequency

The frequency of the steady vibration is the same as the frequency of the driving force. However, there is a phase lag that is a function of the free vibration frequency ω_0, the driving frequency ω and the damping coefficient n, as is shown by Equation (3.121).

(2) Amplitude

The amplitude of the steady vibration is given by Equation (3.120). It can be written as

$$B = \frac{B_0}{\sqrt{(1 - \frac{\omega^2}{\omega_0{}^2})^2 + 4\left(\frac{n}{\omega_0{}^2}\right)^2\left(\frac{\omega}{\omega_0{}^2}\right)^2}}\,, \tag{3.123}$$

where $B_0 = F_0 / k$ is the static displacement of the mass caused by a constant force F_0. If ω / ω_0 is designated as λ and a relative amplitude $\beta = B / B_0$ is introduced, we have

$$\beta = \frac{1}{\sqrt{(1 - \lambda^2)^2 + 4\zeta^2\lambda^2}}\,. \tag{3.124}$$

For a constant force amplitude F_0, the dependence of β on the driving frequency is:

(a) Low Driving Frequencies

In this case, $\omega \ll \omega_0$, or $\lambda \ll 1$, which makes $\beta \approx 1$. This means that the amplitude is the same as the displacement caused by the static force F_0.

(b) Medium Driving Frequencies

In this case, $\omega \approx \omega_0$, or $\lambda \approx 1$. The amplitude has a maximum at $\omega = \omega_0\sqrt{1-2\zeta^2}$. If the damping is light ($\zeta < 0.7$), ω is very close to ω_0, and β is approximately equal to $1/2\zeta$, which can be very large for small ζ. The resonance peak disappears at $\zeta \geq 0.7$. In this case, the curve for $\beta \sim \omega$ relation has the largest flat region (i.e., the largest bandwidth). Therefore, $\zeta = 0.7$ is often referred to as an optimum damping condition.

(c) High Driving Frequencies

In this case, $\omega \gg \omega_0$, or $\lambda \gg 1$, which makes $\beta \approx 1/\lambda^2$. This means that the amplitude decreases very fast with frequency.

Example curves showing the frequency dependence of the relative amplitude are given in Figure 3.28. It indicates that the amplitude of a forced vibration is a function of driving frequency and damping ratio.

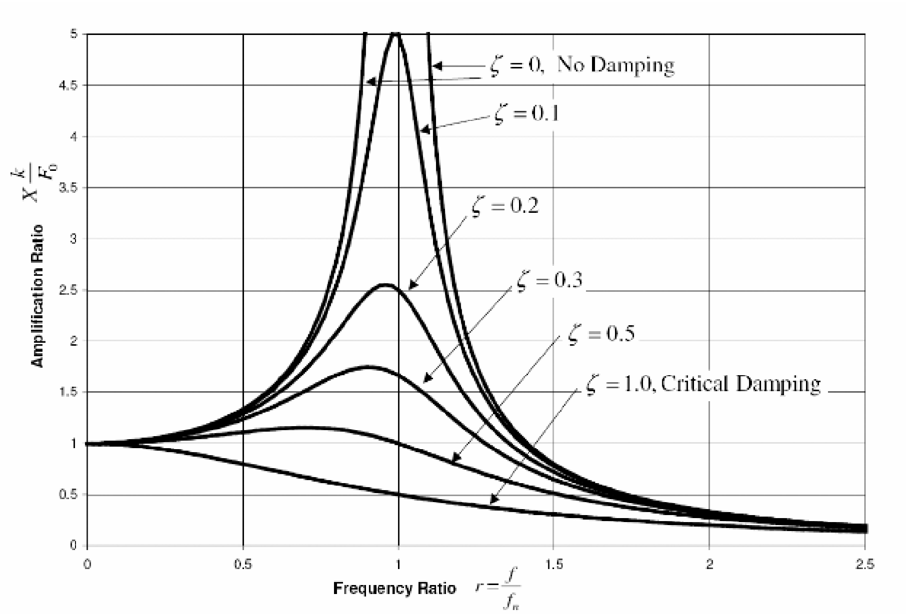

Figure 3.28 Amplitude-frequency relations for different damping ratios

(3) Phase Lag

The forced vibration takes on the frequency of the driving force, but it has a phase lag as shown in Equation (3.121). For very small ω, φ is close to zero. φ increases with ω, passes $\pi/2$ at the natural frequencies of the system and approaches π at very high frequency, as shown in Figure 3.29.

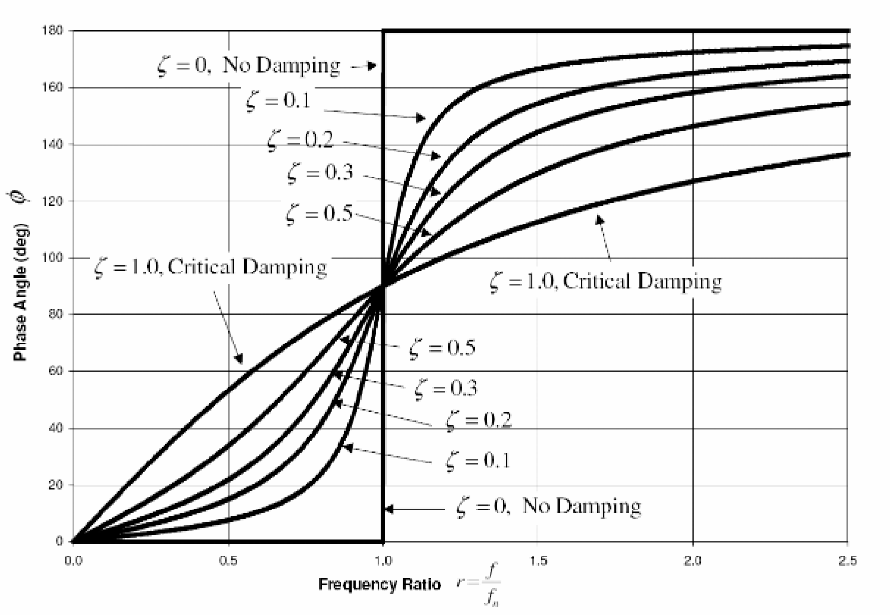

Figure 3.29 Phase lag for different damping ratios

3.5.4 Resonance

According to Equation (3.124) or Figure 3.28, for slight damping, the amplitude has a maximum at a frequency near the free vibration frequency. This phenomenon is known as resonance and the corresponding frequency is called resonant frequency. Using the condition of $d\beta / d\lambda = 0$, we find that the resonant frequency of a forced vibration is at $\lambda_r = \sqrt{1-2\zeta^2}$ or $\omega_r = \omega_0\sqrt{1-2\zeta^2}$. As the natural vibration frequency (without damping) of the system is ω_0, and the damped vibration frequency of the system is $\omega_d = \omega_0\sqrt{1-\zeta^2}$, we find that, for slight damping, ω_0, ω_d and ω_r are all close to each other.

At resonant frequency, the relative amplitude reaches a maximum value

$$\beta_r = \frac{1}{2\zeta\sqrt{1-\zeta^2}}. \tag{3.125}$$

For slight damping, we have the amplitude at resonance: $\beta_r = 1/2\zeta$.

By substituting ω_r into Equation (3.121), we have the phase lag at resonance

$$\varphi_r = \arctan \frac{\sqrt{1-2\zeta^2}}{\zeta}. \tag{3.126}$$

For slight damping, $\varphi_r = \arctan(1/\zeta) \approx \pi/2$ or $\zeta = 1/\tan\varphi_r$.

3.5.5 Quality Factor

For many sensor applications, the sharpness of the resonant peak is important for high resolution or high accuracy of measurement. The parameter to indicate the sharpness of a resonance curve is the quality factor of Q-factor of the system.

Quality factor is mathematically defined as the peak value of the relative amplitude at resonant frequency, i.e.,

$$Q = \beta_r = \frac{1}{2\zeta\sqrt{1-\zeta^2}}. \tag{3.127}$$

It is reasonable to find that Q is related to the damping ratio ζ. The smaller the damping ratio is, the larger the quality factor.

For silicon micro resonators in air, the Q value is usually of the order of 10^2. It may go up to over 10^5 in a vacuum.

3.6 Air Damping

For conventional mechanical machine, the damping caused by the surrounding air can generally be ignored. This is because the energy dissipated by air damping is much smaller than the energy dissipated by other mechanisms.

As air damping is related to the surface area of the moving parts, air damping may become very important for micro mechanical devices and systems in determining their dynamic performance due to the large surface area to volume ratio of the movable parts. For some micro mechanical devices, the energy consumed by air damping must be minimized so that the motion of mechanical parts can be maximized with a limited energy supply. Therefore, estimating the damping effect of the system is one of the most important steps in the analysis and design process of MEMS gyroscopes.

3.6.1 Viscosity of a Fluid

Viscous force appears to oppose the relative motion between different layers of the fluid. Viscosity is thus an internal friction between adjacent layers moving with different velocities. The mechanism of viscosity is shown in Figure 3.30. Assume a fluid moves to the right, the upper layer of the fluid moves faster than the lower layer. The molecules in the upper layer exert a force to the right on the lower layer, which tends to speed up the lower layer; on the other hand, the molecules in the lower layer exert a force to the left on the upper layer, which tends to slow down the upper layer.

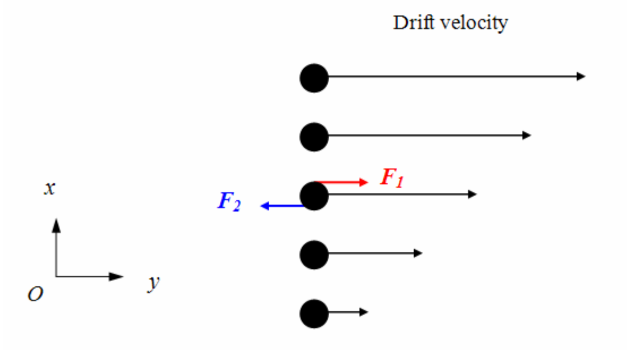

Figure 3.30 Mechanism of viscosity in fluid

The internal shear force in a steady flow of a viscous fluid is proportional to the velocity gradient. If the flow is in the x-direction and the speed of the flow is distributed in the y-direction, i.e., the flow velocity in the x-direction, u is a function of y, the shear force τ_{yx} is

$$\tau_{yx} = \mu \frac{du(y)}{dy}, \tag{3.128}$$

where μ is the coefficient of viscosity of the fluid. If the coefficient of viscosity of a fluid is a constant for a steady flow, the fluid is called a Newtonian fluid.

According to Equation (3.128), the coefficient of viscosity μ has a unit of Pa.sec. The definition of μ at temperature is given by an empirical relation known as Sutherland equation:

$$\mu = \mu_0 \frac{1+T_s/T_0}{1+T_s/T}\sqrt{\frac{T}{T_0}}, \tag{3.129}$$

where $T_0 = 273.16K$; μ_0 is the coefficient of viscosity at temperature T_0; T_s is a constant. μ_0 and T_s are dependent on the specific gas considered. μ_0 and T_s for some gases are listed in Table 3.1. From Table 3.1, we can see that, in the air condition, $\mu_0 = 17.2\times10^{-6}$ Pa·sec and $T_s = 124K$.

Table 3.1 μ_0 and T_s for some gases

gas	air	N_2	H_2	CO_2
$\mu_0/10^{-6}$(Pa.sec)	17.2	16.6	8.40	13.8
$T_s/^\circ K$	124	104	71	254

Usually, the coefficient of viscosity of liquid is much more sensitive to temperature than that of gas. The data for the coefficient of water and air at one atmospheric pressure are listed in Table 3.2. From Table 3.2, we can see that, in room temperature, $\mu = 18.2\times10^{-6}$ Pa·sec.

Table 3.2 Temperature dependence of coefficient of viscosity for water and air (in 10^{-3} Pa.sec for water and in 10^{-6} Pa.sec for water)

t/°C	0	10	20	30	40	50	60	70	80	90	100
H_2O	1.79	1.30	1.02	0.80	0.65	0.55	0.47	0.41	0.36	0.32	0.28
air	17.2	17.8	18.1	18.7	19.2	19.6	20.1	20.4	21.0	21.6	21.8

3.6.2 Slide-film Air Damping

MEMS resonators, actuators, accelerometers, and gyroscopes usually contain movable plates suspended by flexible beams. As the dimensions of the moving plates are usually much larger than their thickness and the gap distance, the viscous damping by the ambient air plays a major role in energy dissipation of the dynamic system. The air film behaves as a slide-film damper to the moving structure. Damping in vibration caused by this air film is called slide-film air damping.

To investigate the basic features of slide-film damping, a mechanical model is considered: a rectangular plate, immersed in an incompressible viscous fluid, moving in a lateral direction at a constant distance from the substrate (see Figure 3.31).

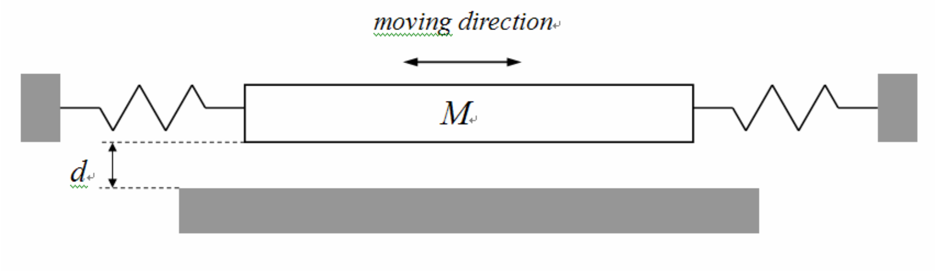

Figure 3.31 Slide-film air damping model

The general differential equation for the steady flow of an incompressible fluid is the well known Navier-Stokes equation:

$$\rho\left[\frac{\partial\vec{v}}{\partial t}+(\vec{v}\cdot\nabla)\vec{v}\right]=\vec{F}-\nabla p+\mu\nabla^2\vec{v}\ , \tag{3.130}$$

where ρ is the density of the fluid; $\vec{F}$ is the force applied; p is the pressure in the fluid; μ is the coefficient of viscosity; and $\vec{v}$ is the velocity of the fluid

$$\vec{v}=u\vec{i}+v\vec{j}+w\vec{k}\ . \tag{3.131}$$

The notations ∇ and ∇^2 are gradient and Laplace operators, respectively,

$$\nabla=\vec{i}\,\frac{\partial}{dx}+\vec{j}\,\frac{\partial}{dy}+\vec{k}\,\frac{\partial}{dz}\text{, and }\nabla^2=\frac{\partial^2}{dx^2}+\frac{\partial^2}{dy^2}+\frac{\partial^2}{dz^2}\ . \tag{3.132}$$

Because of the complexity of Equation (3.130), so far, there is no way to solve the differential equation by using integration. We can only get the approximated solution under some specific situation.

Suppose that the plate is in the x-y plane of the coordinate system, and infinite in dimensions. If the movement of the plate is in the x-direction, and there is no external force or pressure gradient in fluid, we have $u \gg v, w$ and $\frac{\partial^2 u}{\partial z^2} \gg \frac{\partial^2 u}{\partial x^2}, \frac{\partial^2 u}{\partial y^2}$. Thus, Equation (3.130) reduces to

$$\frac{\partial u}{\partial t} + u\frac{\partial u}{\partial x} = \frac{\mu}{\rho}\frac{\partial^2 u}{\partial z^2}. \tag{3.133}$$

For an infinite plate, (i.e., the dimension of the plate is much larger than the gap distance between the plate and the substrate and its oscillation amplitude), the second term on left side of Equation (3.133) may be neglected, resulting in

$$\frac{\partial u}{\partial t} = \frac{\mu}{\rho}\frac{\partial^2 u}{\partial z^2}. \tag{3.134}$$

The non-slippage boundary conditions for the equation are: u equals to zero at the substrate surface and u equals the velocity of the moving plate on the surface of the plate.

We define a characteristic "effective decay distance" as

$$\delta = \sqrt{\frac{2\mu}{\rho\omega}}. \tag{3.135}$$

Based on the relationship of effective decay distance δ and the gap distance d, two damping models can be derived:

(1) Couette-flow Model

When frequency ω and the distance d are small, and δ is much larger (i.e., $\delta \gg d$), the flow pattern of the air around the plate is called a Couette-flow.

In the condition of $(\mu/\rho)(\partial^2 u/\partial z^2) \gg (\partial u/\partial t)$, i.e., $\delta \gg d$, Equation (3.134) can be further simplified as

$$\frac{\partial^2 u}{\partial z^2} = 0. \tag{3.136}$$

Then solve Equation (3.136) with non-slippage boundary conditions

$$u(0) = u_0 \cos\omega t,\ u(d) = 0, \tag{3.137}$$

and we can get the velocity distribution of the fluid

$$u(z) = u(0)(1 - \frac{z}{d}), \tag{3.138}$$

where $u(0)$ is the velocity of the moving plate. The resistive shearing force applied to the plate is

$$F = -\frac{\mu A}{d}u(0), \tag{3.139}$$

where A is the area of the plate.

(2) Stokes-flow Model

In coquette-flow model, the effective decay distance, δ, is much larger than the gap distance d. Therefore, the velocity profile between the plate and the substrate is linear. The model becomes invalid when the gap distance is large.

If the effective decay distance, δ, is not much larger than d, Equation (3.134) has to be used with the non-slippage boundary conditions given in Equation (3.137). By solving the equations, the velocity profile of the fluid is

$$u = u_0 \frac{-e^{-\tilde{d}+\tilde{z}}\cos(\omega t+\tilde{z}-\tilde{d}-\theta)+e^{\tilde{d}-\tilde{z}}\cos(\omega t-\tilde{z}+\tilde{d}-\theta)}{\sqrt{e^{2\tilde{d}}+e^{-2\tilde{d}}-2\cos(2\tilde{d})}}, \tag{3.140}$$

where $\tilde{d} \equiv d/\delta$, $\tilde{z} \equiv z/\delta$, and θ is a phase lag against the oscillation of plate ($u(0) = u_0 \cos \omega t$). The expression for θ is

$$\theta = \arctan \frac{(e^{\tilde{d}}+e^{-\tilde{d}})\sin\tilde{d}}{(e^{\tilde{d}}-e^{-\tilde{d}})\cos\tilde{d}}. \tag{3.141}$$

Thus the damping force on the plate is

$$\begin{aligned} F = A\mu \left.\frac{\partial u}{\partial z}\right|_{z=0} &= \frac{A\mu u_0}{\delta\sqrt{e^{2\tilde{d}}+e^{-2\tilde{d}}-2\cos(2\tilde{d})}}\Big(-e^{-\tilde{d}}\cos(\omega t-\tilde{d}-\theta) \\ &\quad +e^{-\tilde{d}}\sin(\omega t-\tilde{d}-\theta)-e^{\tilde{d}}\cos(\omega t+\tilde{d}-\theta)+e^{\tilde{d}}\sin(\omega t+\tilde{d}-\theta)\Big). \end{aligned} \tag{3.142}$$

For an extreme condition of $\delta \ll d$, from Equation (3.140), we have

$$u = u_0 e^{-\tilde{z}}\cos(\omega t+\tilde{d}-\theta). \tag{3.143}$$

This shows that the fluid around the plate oscillates with the same frequency as the plate, but the oscillation amplitude in the fluid decays exponentially away from the plate. δ is the distance over which the amplitude decreases by a factor of e (=2.718).

We conclude that the damping force now is

$$F = -\frac{\mu A}{\delta}u(0). \tag{3.144}$$

In most of MEMS gyroscopes, gap distance meets the requirement of $d \gg \delta$, so the slide-film air damping can be analyzed with Couette model. The damping coefficient is

$$c = -\frac{\mu A}{d}. \tag{3.145}$$

3.6.3 Squeeze-film Air Damping

When a plate is paced in parallel to a wall and moving towards the wall, the air film between the plate and the wall is squeezed so that some of the air flows out of the gap as shown in Figure 3.32. Therefore, an additional pressure Δp develops in the gap due to the viscous flow of the air. On the contrary, when the plate is moving away from the wall, the pressure in the gap is reduced to keep the air flowing into the gap.

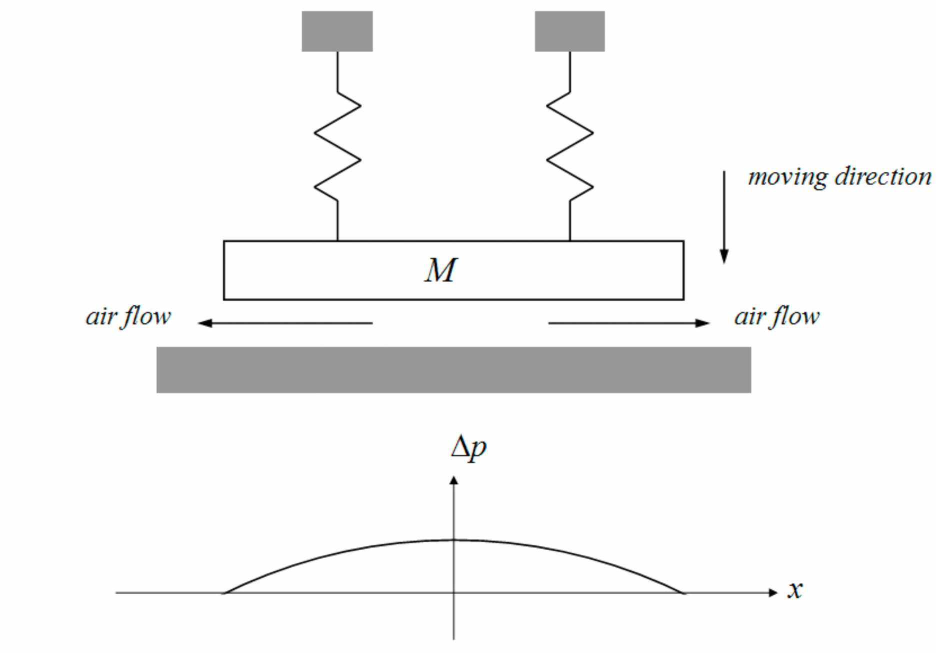

Figure 3.32 Squeeze-film air damping mode

In both moving directions of the plate, the forces on the plate caused by the built-up pressure are always against the movement of the plate. The work done by the plate is consumed by viscous flow of the air and transformed into heat. In other words, the air film acts as a damper and the damping is called squeeze-film air damping.

Obviously, the damping force of squeeze-film air damping is dependent on the gap distance; the smaller the gap, the larger the damping force. When the plate is very far away from the wall, the pressure build-up is negligible.

The squeeze-film air damping has significant effects on the dynamic behavior of microstructures, such as the MEMS parallel-plate capacitive sensors.

Suppose we have a rectangular plate in x-y plane as shown in Figure 3.33. If the side lengths in the x- and y-directions of the plate are $B = 2a$ and $L = 2b$, respectively, and a and b are comparable. The dimensions of the plate B and L are much lager than the gap distance, h, so that the gap flow between the plates caused by the relative motion of the plate is lateral.

The differential equation for pressure in the air film is given by

$$\frac{\partial}{\partial x}\left(\rho\frac{h^3}{\mu}\frac{\partial P}{\partial x}\right)+\frac{\partial}{\partial y}\left(\rho\frac{h^3}{\mu}\frac{\partial P}{\partial y}\right)=12\frac{\partial(h\rho)}{\partial t}. \tag{3.146}$$

Equation (3.146) is referred to as Reynold's equation. Equation (3.146) can be derived from the much more complicated Navier-Stokes equation under the condition that the Modified Reynold's Number for a squeeze film, R_s, is much smaller than unity, i.e. the condition of

$$R_s = \frac{\omega h^2 \rho}{\mu} \ll 1, \tag{3.147}$$

where ω is the radial frequency of the oscillating plate. This condition is satisfied for typical silicon microstructures.

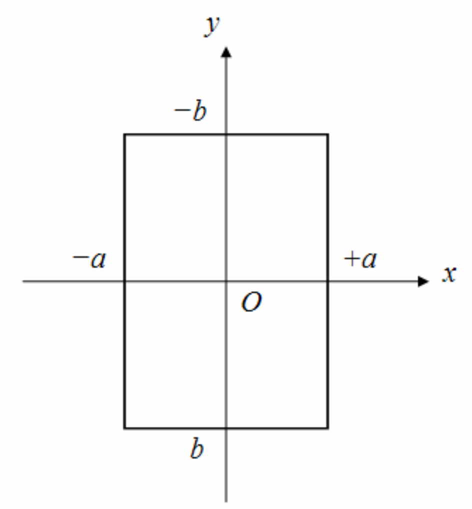

Figure 3.33 Rectangular plate in squeeze-film air damping

As h is assumed to be uniform both in the x- and y-directions, we have

$$\frac{\partial}{\partial x}\left(\rho\frac{\partial P}{\partial x}\right)+\frac{\partial}{\partial y}\left(\rho\frac{\partial P}{\partial y}\right)=\frac{12\mu}{h^3}\frac{\partial(h\rho)}{\partial t}. \tag{3.148}$$

For an isothermal film, the air density, ρ, is proportional to pressure, P, i.e., $\rho=\frac{P}{P_0}\rho_0$. The above equation can be written as

$$\frac{\partial}{\partial x}\left(P\frac{\partial P}{\partial x}\right)+\frac{\partial}{\partial y}\left(P\frac{\partial P}{\partial y}\right)=\frac{12\mu}{h^3}\frac{\partial(h\rho)}{\partial t}. \tag{3.149}$$

Equation (3.149) can be further developed into

$$\left(\frac{\partial P}{\partial x}\right)^2+\left(\frac{\partial P}{\partial y}\right)^2+P\left(\frac{\partial^2}{\partial x^2}P+\frac{\partial^2}{\partial y^2}P\right)=\frac{12\mu}{h^3}\left(P\frac{dh}{dt}+h\frac{\partial P}{\partial t}\right). \tag{3.150}$$

Assuming that $h=h_0+\Delta h$ and $P=P_0+\Delta P$, for small motion distance of the plate, we have $\Delta h \ll h_0$ and $\Delta P \ll P_0$. Under these conditions, the equation can be approximated as

$$P_0\left(\frac{\partial^2\Delta P}{\partial x^2}+\frac{\partial^2\Delta P}{\partial y^2}\right)=\frac{12\mu}{h^3}P_0h_0\left(\frac{1}{h_0}\frac{d\Delta h}{dt}+\frac{1}{P_0}\frac{\partial\Delta P}{\partial t}\right). \tag{3.151}$$

If $\Delta P/P_0 \ll \Delta h/h_0$, the equation can be finally approximated to

$$\frac{\partial^2\Delta P}{\partial x^2}+\frac{\partial^2\Delta P}{\partial y^2}=\frac{12\mu}{h^3}\frac{d\Delta h}{dt}, \tag{3.152}$$

or

$$\frac{\partial^2 P}{\partial x^2}+\frac{\partial^2 P}{\partial y^2}=\frac{12\mu}{h^3}\frac{dh}{dt}. \tag{3.153}$$

With the boundary conditions

$$P(\pm a,y)=0,\ P(x,\pm b)=0, \tag{3.154}$$

the solution to Equation (3.153) can be derived into two parts: $P=p_1+p_2$, where p_1 is a specific solution to Equation (3.153), i.e., p_1 is a solution to equation

$$\frac{\partial^2 p_1}{\partial x^2}+\frac{\partial^2 p_1}{\partial y^2}=\frac{12\mu}{h^3}\dot{h}, \tag{3.155}$$

and p_2 is a general solution to the Laplace equation

$$\frac{\partial^2 p_2}{\partial x^2}+\frac{\partial^2 p_2}{\partial y^2}=0. \tag{3.156}$$

By assuming that $p_1=A+Bx+Cx^2$ and p_1 meets the boundary conditions of $p_1(\pm a)=0$, we find

$$p_1=-\frac{6\mu}{h^3}\frac{dh}{dt}(a^2-x^2). \tag{3.157}$$

From the definition of $P=p_1+p_2$ and the boundary conditions of $P(\pm a,y)=0$, we have

$$p_1(\pm a,y)+p_2(\pm a,y)=0. \tag{3.158}$$

According to Equation (3.157), the boundary conditions for p_2 at $x=\pm a$ can be shown to be

$$p_2(\pm a,y)=0. \tag{3.159}$$

According to Equation (3.154), the boundary conditions for P at $y=\pm b$ should be $P(x,\pm b)=0$, i.e.,

$$p_1(x)+p_2(x,\pm b)=0. \tag{3.160}$$

Therefore, the boundary conditions for p_2 at $y=\pm b$ are

$$p_2(x,\pm b)=-p_1(x)=\frac{6\mu}{h^3}\frac{dh}{dt}(a^2-x^2). \tag{3.161}$$

The complete boundary condition for p_2 are Equation (3.159) and (3.161).

With the boundary conditions, we can get the solution for p_2:

$$p_2(x,y)=\frac{192\mu a^2}{h^3\pi^3}\dot{h}\sum_{n=1,3,5,\dots}^{\infty}\frac{\sin\frac{n\pi}{2}}{n^3\cosh\frac{n\pi b}{2a}}\cosh\frac{n\pi y}{2a}\cos\frac{n\pi x}{2a}. \tag{3.162}$$

Therefore, the final solution to the problem is

$$P=p_1+p_2=-\frac{6\mu\dot{h}}{h^3}(a^2-x^2)+\frac{192\mu\dot{h}a^2}{h^3\pi^3}\sum_{n=1,3,5,\dots}^{\infty}\frac{\sin\frac{n\pi}{2}}{n^3\cosh\frac{n\pi b}{2a}}\cosh\frac{n\pi y}{2a}\cos\frac{n\pi x}{2a}. \tag{3.163}$$

The damping force on the rectangular plate is

$$F = \int_{-a}^{a} dx \int_{-b}^{b} P(x,y)dy = -\frac{\mu LB^3}{h^3}\dot{h}\beta\left(\frac{B}{L}\right). \tag{3.164}$$

where the factor $\beta(B/L)$ is

$$\beta\left(\frac{B}{L}\right) = 1 - \frac{192}{\pi^5}\left(\frac{B}{L}\right)\sum_{n=1,3,5,}^{\infty} \tanh\left(\frac{n\pi L}{2B}\right). \tag{3.165}$$

The dependence of β on B/L is shown by the curve in Figure 3.34. For a very long plate, $\beta = 1$, and for a square (i.e., $a = b$), $\beta = 0.42$. The coefficient of the damping force is

$$c = -\frac{\mu LB^3}{h^3}\beta\left(\frac{B}{L}\right). \tag{3.166}$$

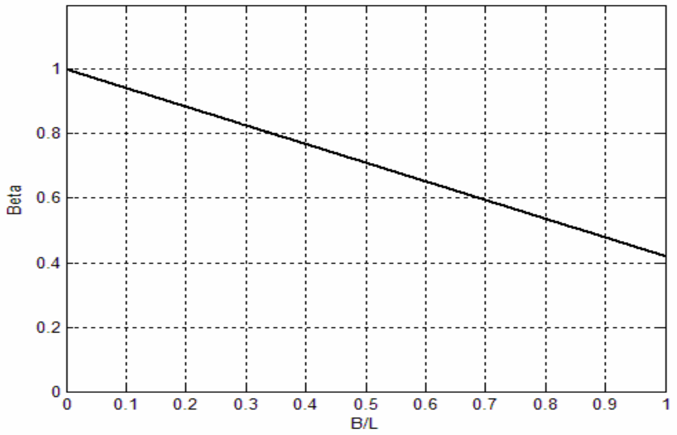

Figure 3.34 The dependence of factor β on the aspect ratio B/L

3.6.4 Damping in Rarefied Air

To achieve high quality factors in driving and sensing mode, and therefore achieve a high sensitivity, MEMS gyroscopes usually work in vacuum state to reduce the air damping effect.

Experiment results show that in an appropriate range, with the decrease in air pressure, the air damping force goes down, or the quality factor of the system goes up. However, the quality levels off when the vacuum is high enough. Figure 3.35 is the dependence of quality factor on air pressure from atmospheric pressure to high vacuum.

From the figure, we can see that the Q factor at high pressure is independent of pressure as shown by sector A of the curve. The Q factor in this region is determined by the geometries and the moving directions of the moving structure. The damping mechanism could be the squeeze-film damping, the slide-film damping, or a combination of the two.

When the pressure is pumped down to a certain extent (10^2~10^3 Pa), the Q factor starts to rise when the effect of rarefaction starts to play an important role. The Q factor is inversely proportional to the air pressure in this region as shown by sector B of the curve. The transition pressure from sector A to sector B is usually in the range of several hundreds Pa. The exact value is dependent on the geometries and vibration mode of the structure.

At high vacuum, when the air damping is very small, the effects of inertial friction and energy losses via the structure supports become dominate. If the vacuum is high enough, the Q factor becomes a constant as shown by sector C of the curve. The critical pressure from sector B to sector C is usually on the order of 1Pa.

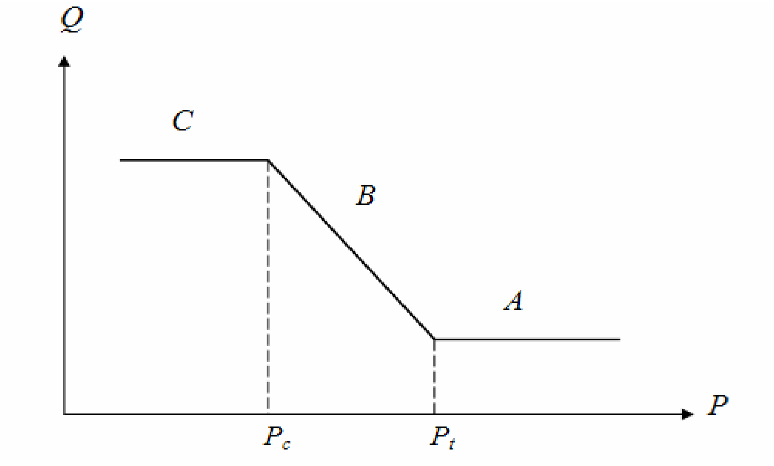

Figure 3.35 Dependence of Q factor on air pressure

CHAPTER IV. A NOVEL GYROSCOPE

4.1 Related Work

Among different kinds of MEMS gyroscopes, the electrostatic driving, capacitance sensing microgyroscope is a very attractive category [14]-[15]. These gyroscopes use electrostatic comb drive to activate the device in X direction. If there is an angular velocity along Y direction, the mass will vibrate along Z direction due to Coriolis force. By measuring the capacitance change between the moving mass and fixed electrode plate, the value of angular velocity can be known.

In vibrating gyroscopes, reducing the mismatch between the resonant frequencies of the driving and detection modes is important to attain high detection sensitivity. However, as the mismatch decreases, the mechanical coupling between the two modes makes operation more and more unstable. In [16]-[21], vibratory microgyroscopes with independent beams for driving and sensing are reported. With driving and sensing beams sensitive to vibrations along different directions, these microgyroscopes can significantly reduce mechanical coupling effect. Due to the small sensing mass and small size of the MEMS gyroscopes, the signal detection is always a very challenging issue. Z-axis vibratory gyroscopes [16]-[18] usually use comb fingers to sense the capacitance change, typically having device capacitance in the range of pF (10^{-12} F) and capacitance change in the range of fF (10^{-15} F). X/Y-axis vibratory gyroscopes [19]-[21] vibrate laterally through push-pull comb drive and detect the displacement of the mass vertically. These microgyroscopes have a lager capacitive overlap area than Z-axis vibratory gyroscopes, however, suffered from squeeze film air damping.

4.1.1 A Gyroscope of Comb-finger Diving and Parallel-plate Sensing

A vibratory microgyroscope with a thin polysilicon resonator fabricated by silicon surface micromachining is proposed in [14]. The resonator with comb fingers is driven in a lateral direction by electrostatic force. The angular rate is detected as the capacitance change in vertical direction between the resonator and its substrate. This surface micromachined vibratory gyroscope is shown in Figure 4.1.

In the gyroscope, a polysilicon resonator 400μm wide (including comb fingers on both sides), 800μm long (including beams on both sides) and 5μm thick is suspended by four beams floating on a single-crystal silicon substrate. The ends of the beams are anchored on the silicon substrate.

The driving direction is lateral (in x-direction) to obtain a large deflection amplitude. The resonator is driven by electrostatic force generated by an AC voltage applied across the comb fingers on both sides of the resonator. The Coriolis force produced by an angular rate around the y-axis causes the resonator to vibrate in the z-direction. This vibrated deflection is very small and can be detected from the change in the electrostatic capacitance of the gap between the resonator and the substrate. The gap was designed to be 1μm to detect the change with high sensitivity. The deformed shapes of this vibratory gyroscope in driving and sensing modes are shown in Figure 4.2.

The four beams supporting the mass are bent in the x-direction in the driving mode, and in the y-direction in sensing mode. Therefore, they work as both the driving beams and the sensing beams. The advantage of this design is that the frequency mismatch can be easily eliminated by setting the beam width and thickness to be the same. However, the disadvantage is that coupling between the two modes may arise if the beams are not completely symmetrical as a result of fabrication error during silicon micromachining.

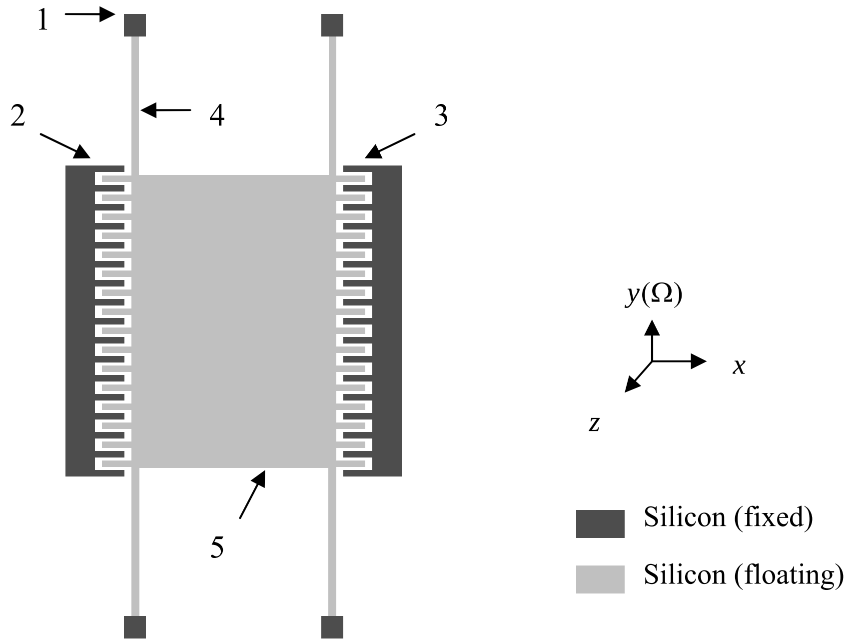

Figure 4.1 Structure of the vibratory gyroscope using comb-finger driving and parallel-plate sensing: 1. anchors 2. left fixed driving fingers 3. right fixed driving fingers 4. driving/sensing beams 5. central movable mass

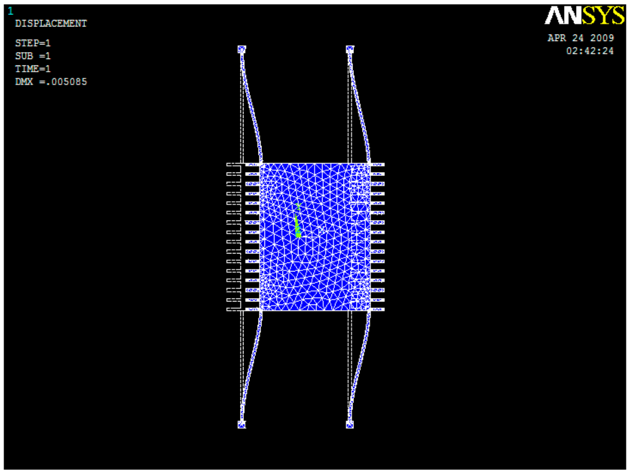

Figure 4.2(a) Deformed shape in driving mode of the gyroscope using comb-finger driving, parallel-plate sensing

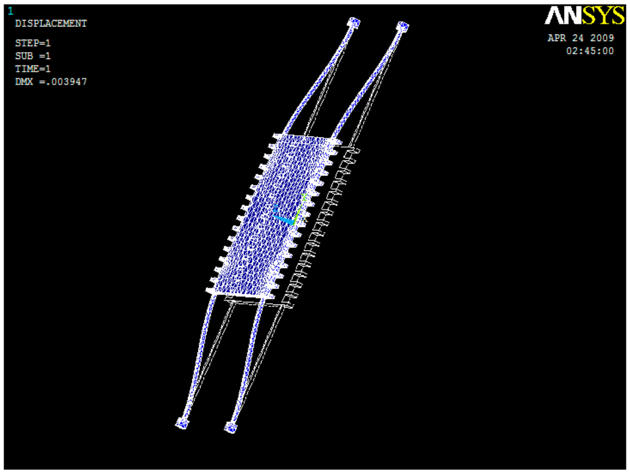

Figure 4.2(b) Deformed shape in sensing mode of the gyroscope using comb-finger driving, parallel-plate sensing

The plot in Figure 4.3 shows that Q factor of the device is a function of ambient pressure. The driving mode of the resonator can be induced in air, but the vibration amplitude is small due to the slide-film air damping. One the other hand, the sensing mode can not be induced above 50 Pa, because the squeeze-film air damping affects the vibration amplitude more strongly than the slide-film damping. As pressure decreases, the amplitudes and Q factors of both modes rise. Below 0.1 Pa, where the intrinsic Q factors of the structure and the material dominate, the Q factors saturate. The saturated values are approximately 2,800 for the driving mode and 16,000 for the sensing mode. This indicates that the vibratory gyroscope has to be packaged in a high vacuum state.

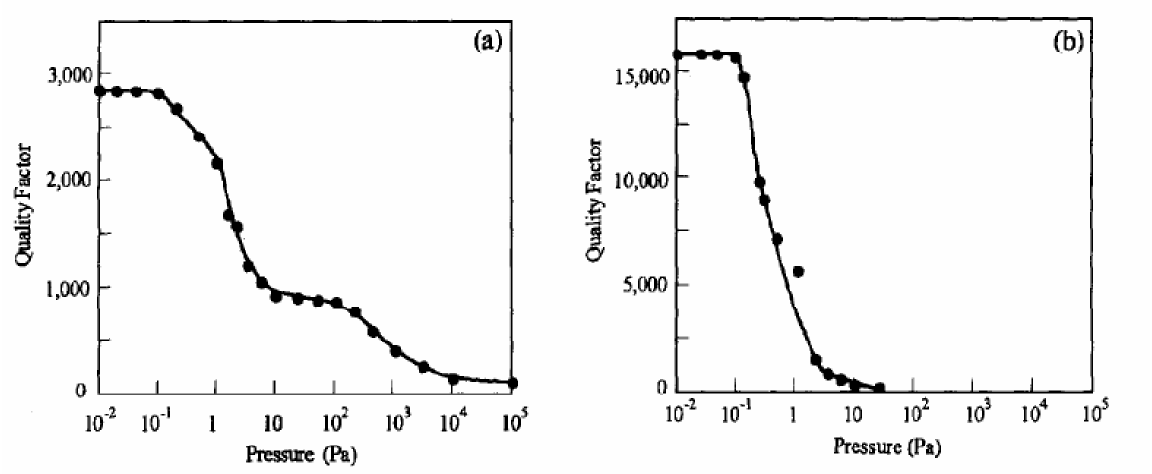

Figure 4.3 Q factors for: (a) the driving mode; (b) the sensing mode.

4.1.2 A Gyroscope with Independent Beams for Diving and Sensing

To reduce the mechanical coupling effect, a new structure of the gyroscope design is proposed in [19]. It features independent pairs of beams for the driving and sensing modes. The mass of the oscillator is connected to a frame supported by four driving beams which are anchored to the substrate. The central movable mass is connected to the frame through four sensing beams. The oscillator is 800μm×1200μm×50μm in size. The inner beams are 20μm wide and 10μm thick, and the outer beams are 5μm wide and 50μm thick. The device is driven by comb electrodes, and there is an electrode under the mass, just as in the first design. The structure of this independent-beam vibratory gyroscope is shown in Figure 4.4. The cross section views of the driving and sensing beams are shown in Figure 4.5.

In the driving mode, the outer beams are bent in the x-direction, but there is little deflection of the inner beams. In the sensing mode, the inner beams are bent in the z-direction, but there is little deflection of the outer beams. This indicates that the outer and inner beams are rigid respect to the z- and x-directions, respectively. That is to say, the two pairs of beams move independently in the two modes. Therefore, the coupling between the two modes is very weak because driving mode oscillations have little effect on the beams used in the sensing mode.

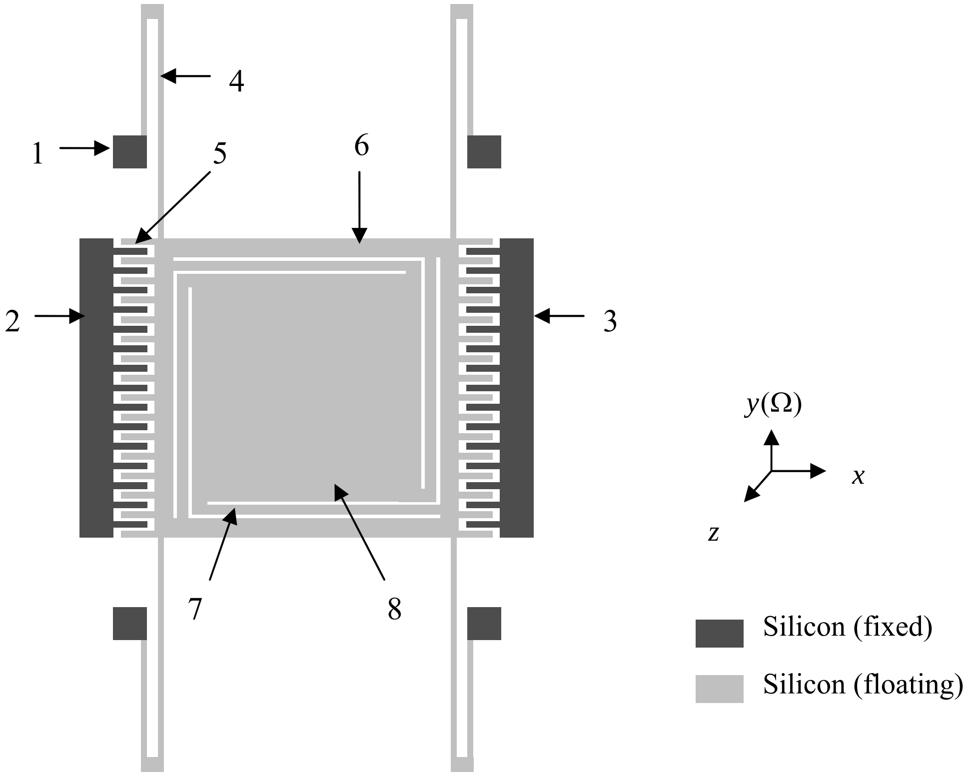

Figure 4.4 Structure of the vibratory gyroscope with independent beams for driving and sensing: 1. anchors 2. left fixed driving fingers 3. right fixed driving fingers 4. driving beams 5. movable driving fingers 6. frame 7. sensing beams 8. central movable mass

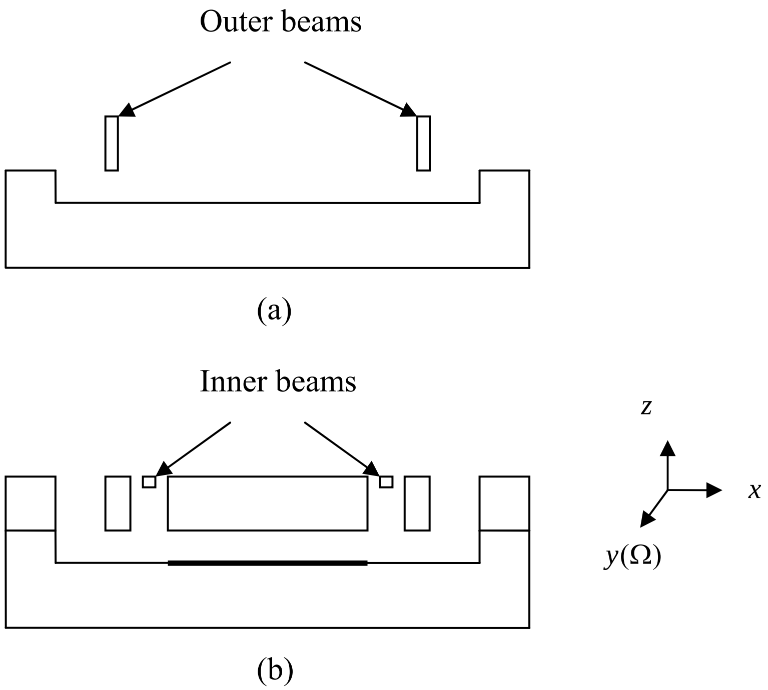

Figure 4.5 Cross-sectional view of the vibratory gyroscope with independent beams for driving and sensing: (a) outer beams; (b) inner beams.

The deformed shapes of this improved vibratory gyroscope in driving and sensing modes are shown in Figure 4.6.

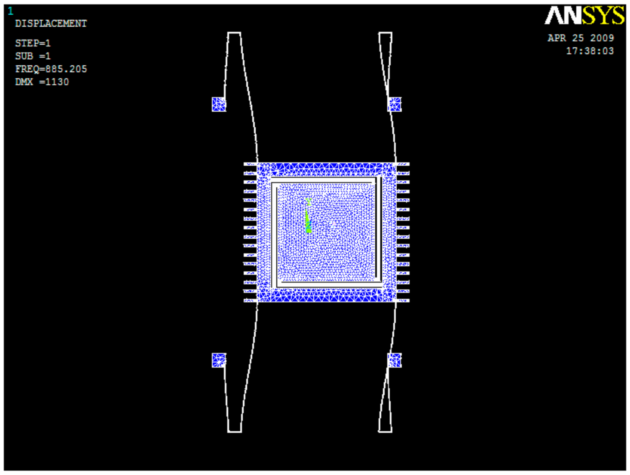

Figure 4.6 (a) Deformed shape in driving mode of the gyroscope with independent beams for driving and sensing

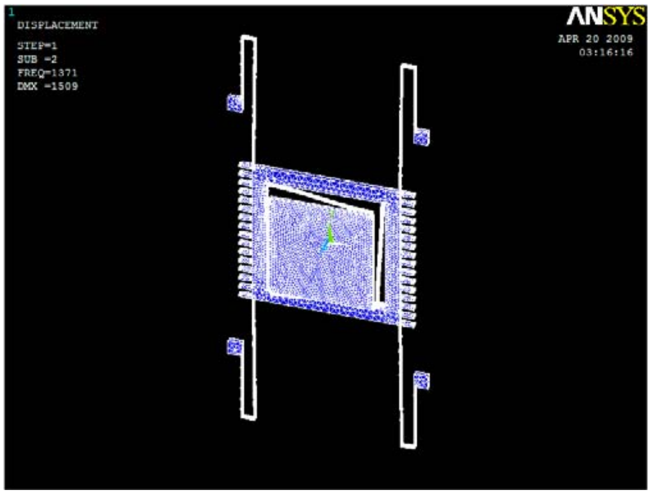

Figure 4.6(b) Deformed shape in sensing mode of the gyroscope with independent beams for driving and sensing

Oscillation amplitudes in both modes are measured with a two-dimensional laser displacement meter. Figure 4.7 shows the amplitude ratio, which is the ratio of the amplitude in sensing mode to the amplitude in driving mode, as a function of frequency mismatch. It is clear that the coupling of the gyroscope with independent driving and sensing beams is much smaller that that of the gyroscope with same beams for driving and sensing.

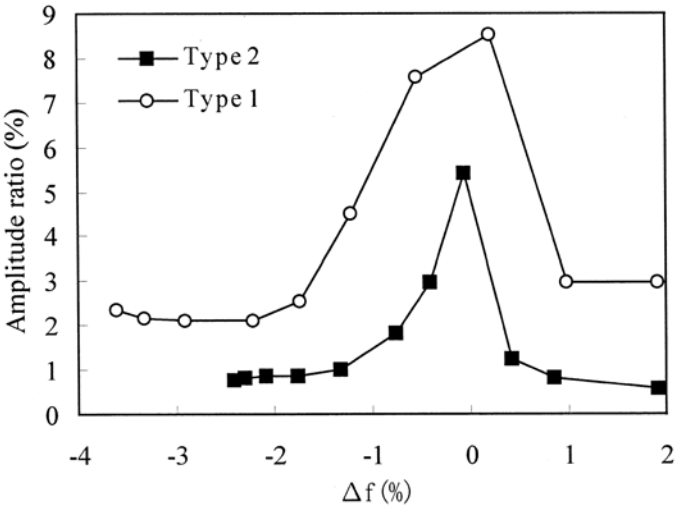

Figure 4.7 Amplitude ratio vs. frequency mismatch

4.1.3 A Gyroscope of Comb-finger Diving and Comb-finger Sensing

In [16], an electrostatic comb driving, comb capacitance sensing bulk micromachined microgyroscope design is proposed. The microgyroscope also uses independent beams for driving and sensing. The driving portion has large stiffness along the sensing vibration direction; similarly, the sensing portion has large stiffness along the driving vibration direction. Thus, it can help eliminate the mechanical coupling of driving vibration to the sensing mode.

The structure of this comb vibratory gyroscope is shown in Figure 4.8. The microgyroscope consists of both driving and sensing portions. The top and bottom movable driving fingers and the trusses are connected to the substrate through the driving beams, forming the driving portion. The movable driving fingers are activated by the electrostatic force applied on top and bottom fixed driving fingers. The movable central mass with the movable sensing fingers are connected to the trusses, forming the sensing portion. The movable sensing fingers constitute differential sensing capacitances with left and right sensing fingers.

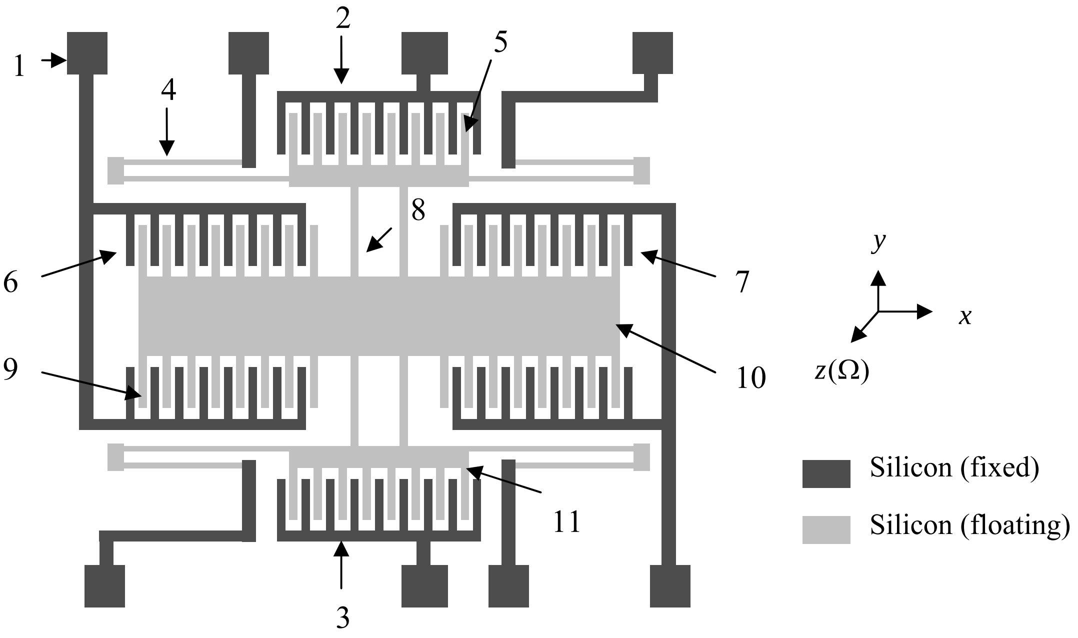

Figure 4.8 Structure of the vibratory gyroscope of comb-finger driving and comb-finger sensing: 1. anchors 2. top fixed driving fingers 3. bottom fixed driving fingers 4. driving beams 5. movable driving fingers 6. left fixed sensing fingers 7. right fixed sensing fingers 8. sensing beams 9. movable sensing fingers 10. central movable mass 11. truss

During operation, AC driving voltage is applied to the top and bottom fixed driving fingers. This induces alternating electrostatic forces on the movable driving fingers along y-direction in a push-pull mode. The central movable mass will vibrate along y-direction, which is the driving mode. The frequency of the driving voltage is chosen to activate the central mass in its resonant mode in order to achieve large vibration amplitude. If there is an angular velocity along the z-direction, the central mass will experience am alternating Coriolis force along x-direction. This in turn will activate the central mass to vibrate along x-diretion, which is the sensing mode. The sensing differential capacitance gaps will change due to the sensing vibration along x-direction. By measuring this differential capacitance change, we know the value of the angular velocity. This is the working principle of the comb vibratory microgyscope.

The deformed shapes of this comb vibratory gyroscope in driving and sensing modes are shown in Figure 4.9.

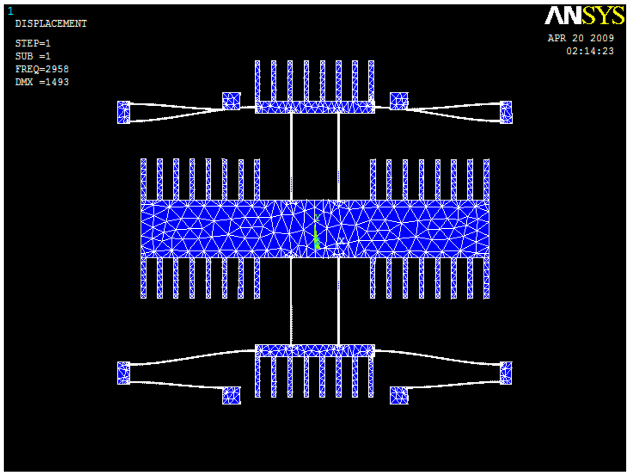

Figure 4.9 (a) Deformed shape in driving mode of the gyroscope using comb-finger driving and comb-finger sensing

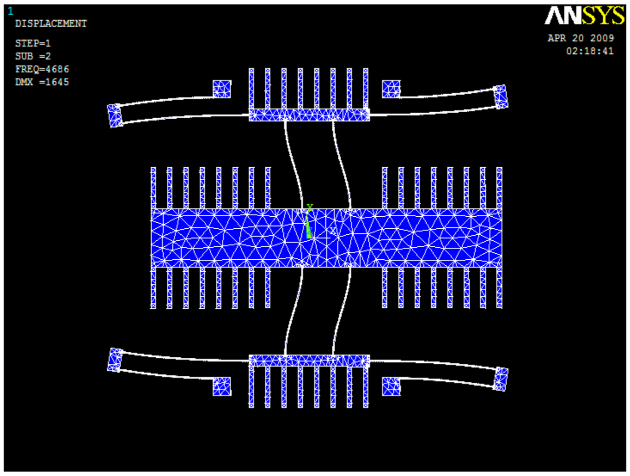

Figure 4.9(b) Deformed shape in sensing mode of the gyroscope using comb-finger driving and comb-finger sensing

Design parameters of this microgyroscope are then given in Table 4.1, and performance parameters are given in Table 4.2 on the condition that *Q* factors in both driving and sensing modes are 2000.

Table 4.1 Optimized design parameters of the gyroscope using comb-finger driving and comb-finger sensing

Design Parameters	**Values**
Device dimension	4.0mm×4.4mm
Device thickness	100μm
Driving beam width W_f	12μm
Sensing beam width W_b	10μm
Number of driving capacitance groups N_d	30×2
Driving capacitance gap d_d	3μm
Number of sensing capacitance pairs N_s	36
Sensing capacitance gap d_s	3μm
Gap between device and substrate	10μm

Table 4.2 Performance parameters of the gyroscope using comb-finger driving and comb-finger sensing

Performance Parameters	**Values**
Static capacitance C_s	7.2pF
Driving mass M_d	556μg
Sensing mass M_s	485μg
Driving mode resonant frequency f_d	9062Hz
Sensing mode resonant frequency f_s	9568Hz
Displacement sensitivity S_d	4nm/(°/sec)

4.2 A Novel Gyroscope Design

Based upon the above analysis, we can see that the gyroscope in [14] can easily eliminate the frequency mismatch between the driving and sensing modes; however, it suffers from mechanical coupling effect, which greatly degrades the device performance. The gyroscope in [19] has successfully solved the problem of coupling between two modes, but the vibration amplitude is small due to the short length of the driving and sensing beams. The gyroscope in [16] utilizes folded beams to increase the vibration amplitude, but still has the limitation in measuring the capacitance change because of the comb capacitance it uses, thus has a relative low capacitance sensitivity. Therefore, we think out a novel vibratory gyroscope design, having its unique advantages in eliminating mechanical coupling and improving capacitance sensitivity.

4.2.1 Device Structure

This novel microgyroscope is a comb driving, plate differential capacitance sensing vibratory gyroscope, as shown in Figure 4.10. The device is fabricated through bulk micromachining process and DRIE (Deep Reactive-Ion Etching) technique is used for comb finger etching, so that the device thickness can reach 100μm. Furthermore, the device is based on glass-silicon-glass compound structure through silicon-glass anodic bonding technique.

In the figure, the dark areas are anchored to the glass substrate, and the areas in light color are floating 10 um above the substrate and free for vibration. The microgyroscope consists of both driving and sensing portions. The left driving fingers, the right driving fingers and the truss are connected to the anchors through folded driving beams. The folded driving beam structure can help increase the amplitude of the driving vibration. The sensing portion consists of four sensing beams and a central mass. Similarly, the folded sensing beam structure can help increase the amplitude of the sensing vibration. The central movable mass constitutes differential sensing capacitances with top and bottom aluminum electrodes (which are not shown here) deposited on the glass substrates. The upper and lower bonding anchors offer protection for the movable parts.

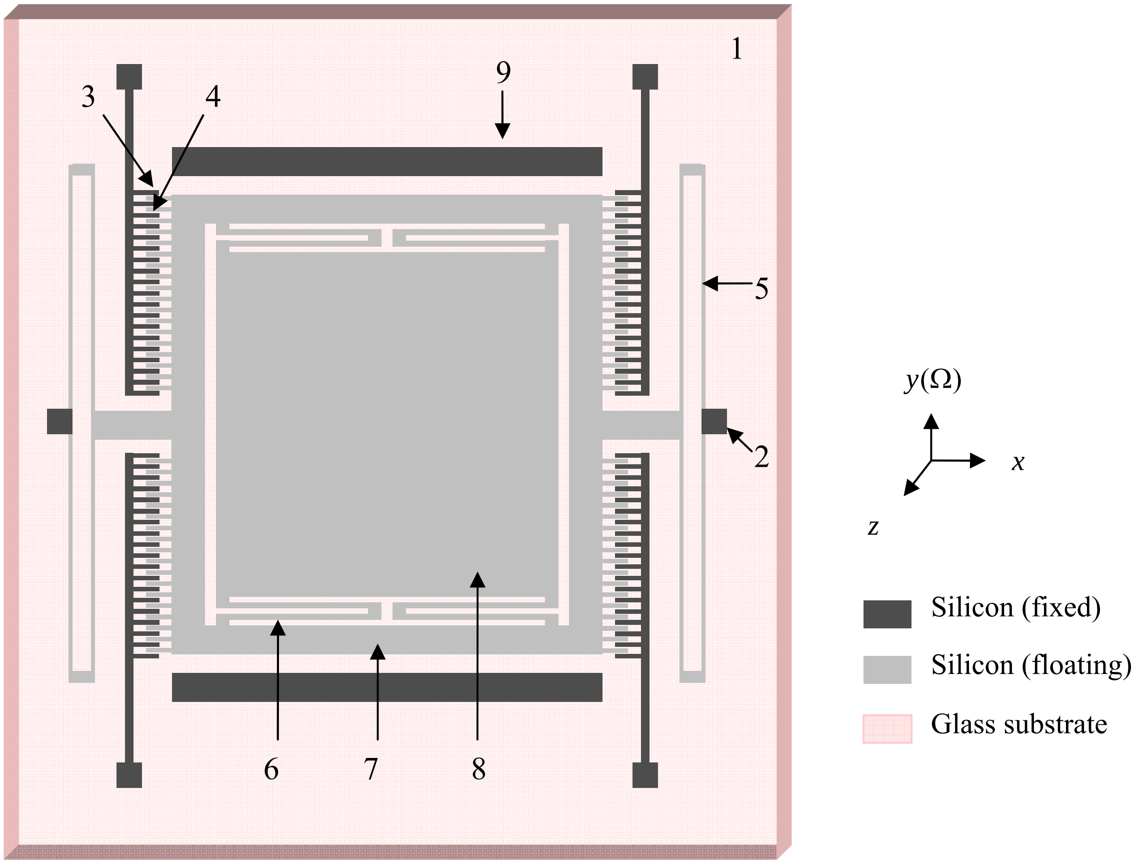

Figure 4.10 Structure of the novel comb-driving differential-capacitance-sensing vibratory gyroscope design: 1. glass substrate 2. anchors 3. fixed driving fingers 4. movable driving fingers 5. folded driving beams 6. folded sensing beams 7. truss 8. central movable mass 9. bonding anchors

This novel microgyroscope design has the following features: (1) The folded beam structures in driving portion help increase the amplitude of the driving vibration; similarly, the folded beam structures in sensing portion help increase the amplitude of the sensing vibration. They both help increase the device sensitivity. (2) In driving mode, the driving beams are bent in the x-direction, but there is little deflection of the sensing beams; similarly, in sensing mode, the sensing beams are bent in the z-direction, but there is little deflection of the driving beams. This indicates that the driving and sensing beams are rigid respect to the z- and x-directions, respectively. Thus, the coupling between the two modes is very weak. (3) The sensing beams are designed in the middle of the mass thickness, so that the lateral effect can be avoided. In light of this design, the central movable mass only responds to the angular velocity, but not to any lateral acceleration. (4) Due to DRIE technique, the device thickness can be increased to more than 100μm, or even the thickness of silicon wafer. This greatly increases the sensing mass, which can help increase the device sensitivity. The releasing gap for the movable parts is pre-etched in silicon, and due to the large thickness of the device, the stiction problem in surface micromachining is avoided. (5) The glass is used as substrate, so that parasitic capacitance can be minimized, which is helpful for the signal detection. The top and bottom glass covers also limit the maximum range of displacement of the sensing mass in case of z-axis overloading, which is helpful for shocking environment. (6) Using single-crystal silicon as structure can help achieve high quality factor for both driving and sensing modes of the gyroscope. Compared to poly-silicon material, there is no residual stress in it. (7) Furthermore, the device uses differential capacitance sensing instead of sensing a single capacitance change, this can further cancel the environment noise and improve the device capacitance sensitivity.

4.2.2 Working Principle

The working principle of the device is similar to the other microgyroscopes. During operation, AC driving voltages with same magnitude but 180º phase difference are applied to the left and right fixed driving fingers. This introduces alternating electrostatic forces on the movable driving fingers along x-direction. Because the driving beams are more sensitive to the excitation in x-direction, the truss along with central mass will vibrate along x-direction in a push-pull mode, which is the driving mode. The frequency of the driving voltages is carefully chosen to match the resonant frequency of the truss and central mass structure, in order to achieve large vibration amplitude.

If there is an angular velocity along y-direction, the central mass will experience an alternating Coriolis force along z-direction. Because the sensing beams are more sensitive to the excitation in z-direction, the central movable mass will be activated to vibrate along z-direction, which is the sensing mode. The sensing differential pair will change due to the sensing vibration along z-direction. By measuring this differential capacitance change, we know the value of the angular velocity.

4.2.3 Optimized Design Parameters

Based upon the dynamic analysis in Section 4.3, a set of optimized design parameters of this MEMS gyroscope can be achieved. From Table 4.3, the device has a dimension of

5.8mm×6.0mm×0.1mm.

Table 4.3 Optimized design parameters of the novel gyroscope

Design Parameters	**Values**
Device dimension	5.8mm×6.0mm
Device thickness	100μm
Driving beam length L_{bd}	1770μm
Driving beam width W_{bd}	12μm
Driving beam thickness t_{bd}	80μm
Sensing beam length L_{bs}	1200μm
Sensing beam width W_{bs}	60μm
Sensing beam thickness t_{bs}	8μm
Central mass length L_m	3000μm
Central mass width W_m	3000μm
Central mass thickness t_m	80μm
Comb finger length L_f	200μm
Comb finger width W_f	40μm
Comb finger thickness t_f	80μm
Total number of finger pairs N_f	80
Driving capacitance gap d_f	3μm
Sensing capacitance gap d_0	10μm
Truss width	250μm
Truss thickness	80μm
Anchor size	200μm×200μm
Aluminum electrode size	2.5mm×2.5mm
Bonding anchor length	3.7mm
Bonding anchor width	0.3mm
DC driving voltage	10V
AC driving voltage	2V

4.3 Dynamic Analysis

From the discussion in Section 3.1, we know that a MEMS gyroscope can be simplified as a vibrating system with two orthogonal vibration modes. The driving mode corresponds to the vibration of the driving mass in the x-direction. The sensing mode corresponds to the vibration of the sensing mass in the y-direction.

When the driving mass is driven along the x-direction by an electrostatic driving force ($F_d(t) = F_0 \cos \omega_d t$), and it is subjected to a constant angular velocity (Ω), a Coriolis force ($F_c(t) = 2M_s \Omega \frac{dx(t)}{dt}$) is introduced in y-direction (here we use y- instead of z- for simplicity, however, in our design, the sensing mass moves along z-direction) to the sensing mass. In this case, the equation of motion is

$$M_d \frac{d^2x(t)}{dt^2} + c_x \frac{dx(t)}{dt} + k_x x(t) = F_0 \cos w_d t\,, \tag{4.1}$$

$$M_s \frac{d^2y(t)}{dt^2} + c_y \frac{dy(t)}{dt} + k_y y(t) = 2M_s \Omega \frac{dx(t)}{dt}\,. \tag{4.2}$$

where M_d is the driving mass, which includes the mass of the movable driving fingers, the truss, the sensing beam and the sensing mass; M_s is the sensing mass; c_x and c_y are the resistances due to air damping effect on x- and y-direction, respectively; k_x and k_y are the total spring constants of the driving beam and the sensing beam on x- and y-direction, respectively; $x(t)$ and $y(t)$ are the displacement of the driving mass and the sensing mass on x- and y-direction, respectively.

4.3.1 Spring Constant and Resonant Frequency

In our design, four folded driving beams can be treated as four springs connected in parallel. For each folded beam, both sections of the beams can be treated as two springs connected in series. Each beam section can be applied to the double-clamped beam model.

Spring constant k_{b_d} of one section of the driving beams can be calculated using double-clamped beam spring constant equation

$$k_{b\_d} = \frac{12EI_{b\_d}}{L_{b\_d}{}^3}\,, \tag{4.3}$$

where I_{b_d} is the inertial momentum of the driving beams

$$I_{b\_d} = \frac{1}{12} t_{b\_d} W_{b\_d}{}^3\,. \tag{4.4}$$

Two sections in a folded driving beam are connected in series and have the same size. Thus, spring constant of one folded driving beam is

$$k_{fold\_d} = \frac{1}{2} k_{b\_d} = \frac{6EI_{b\_d}}{L_{b\_d}{}^3}\,. \tag{4.5}$$

Four folded driving beams are connected in parallel and have the same size. Thus, total spring constant in driving direction is

$$k_x = 4k_{fold\_d} = \frac{24EI_{b\_d}}{L_{b\_d}{}^3} = \frac{2Et_{b\_d} W_{b\_d}{}^3}{L_{b\_d}{}^3}\,. \tag{4.6}$$

Similarly, four folded driving beams can be treated as four springs connected in parallel. For each folded beam, both sections of the beams can be treated as two springs connected in series. Each beam section can be applied to the double-clamped beam model.

Spring constant k_{b_s} of one section of the driving beams can be calculated using double-clamped beam spring constant equation

$$k_{b\_s} = \frac{12EI_{b\_s}}{L_{b\_s}{}^{3}}, \tag{4.7}$$

where I_{b_s} is the inertial momentum of the driving beams

$$I_{b\_s} = \frac{1}{12} W_{b\_s} t_{b\_s}{}^{3}. \tag{4.8}$$

Note that term $t_{b\_d} W_{b\_d}{}^{3}$ in Equation (4.4) is replaced by $W_{b\_s} t_{b\_s}{}^{3}$ in Equation (4.8), because the sensing beams are deflected in the direction of thickness. Two sections in a folded driving beam are connected in series and have the same size. Thus, spring constant of one folded driving beam is

$$k_{fold\_s} = \frac{1}{2} k_{b\_s} = \frac{6EI_{b\_s}}{L_{b\_s}{}^{3}}. \tag{4.9}$$

Four folded driving beams are connected in parallel and have the same size. Thus, total spring constant in driving direction is

$$k_y = 4k_{fold\_s} = \frac{24EI_{b\_s}}{L_{b\_s}{}^{3}} = \frac{2EW_{b\_s} t_{b\_s}{}^{3}}{L_{b\_d}{}^{3}}. \tag{4.10}$$

According to the definition of resonant frequency, the resonant radial frequencies in x- and y-direction are

$$\omega_x = \sqrt{\frac{k_x}{M_d}} = \sqrt{\frac{2Et_{b\_d} W_{b\_d}{}^{3}}{M_d L_{b\_d}{}^{3}}}, \tag{4.11}$$

$$\omega_y = \sqrt{\frac{k_y}{M_s}} = \sqrt{\frac{2EW_{b\_s} t_{b\_s}{}^{3}}{M_s L_{b\_s}{}^{3}}}. \tag{4.12}$$

Then, the resonant frequencies in x- and y-direction are

$$f_x = \frac{1}{2\pi} \omega_x = \frac{1}{2\pi} \sqrt{\frac{2Et_{b\_d} W_{b\_d}{}^{3}}{M_d L_{b\_d}{}^{3}}}, \tag{4.13}$$

$$f_y = \frac{1}{2\pi} \omega_y = \frac{1}{2\pi} \sqrt{\frac{2EW_{b\_s} t_{b\_s}{}^{3}}{M_s L_{b\_s}{}^{3}}}. \tag{4.14}$$

From Equation (4.13) and (4.14), we can have these conclusions: (1) resonant frequency decrease as the beam length increase; (2) resonant frequency increase as the beam width increase; (3) resonant frequency increase as the beam thickness increase; (4) driving mode resonant frequency is more sensitive to beam length and width, less sensitive to beam thickness: $f_x \propto 1/L_{b\_d}{}^{3/2}$, $f_x \propto W_{b\_d}{}^{3/2}$, $f_x \propto t_{b\_d}{}^{1/2}$; (4) sensing mode frequency is more sensitive to beam length and thickness, less sensitive to beam width: $f_y \propto 1/L_{b\_s}{}^{3/2}$, $f_y \propto t_{b\_s}{}^{3/2}$, $f_y \propto W_{b\_s}{}^{1/2}$. Figure 4.11 shows the relationship between resonant frequencies in x- and y-direction and their beam sizes, respectively.

With the design parameters in Table 4.3, we can calculate the gyroscope spring constants

$$k_x = 8.476N/m \text{ and } k_y = 6.044N/m, \tag{4.15}$$

as well as resonant frequencies

$$f_x = 289.0Hz \text{ and } f_y = 302.1Hz. \tag{4.16}$$

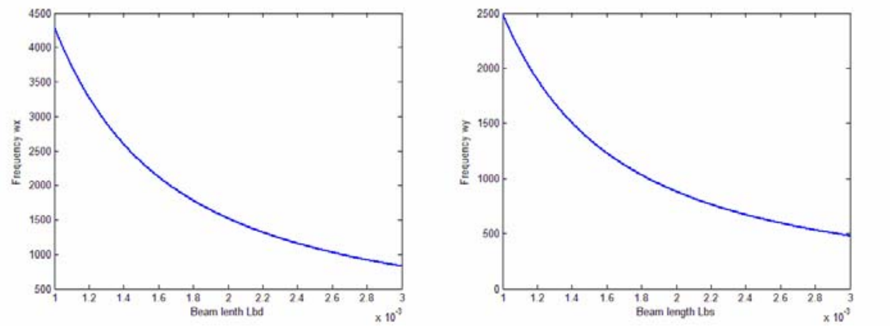

(a) f_x vs. L_{bd} (d) f_y vs. L_{bs}

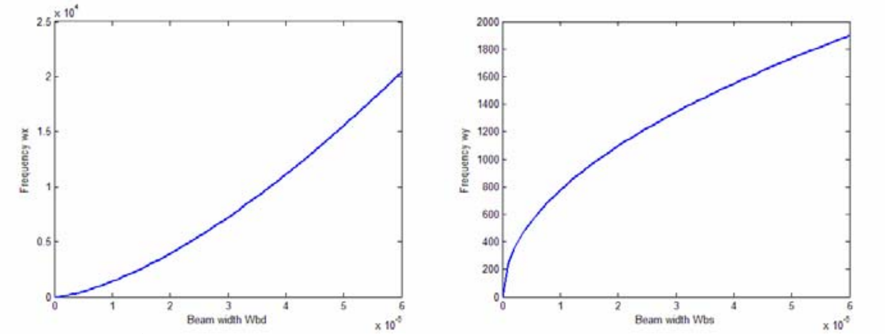

(b) f_x vs. W_{bd} (e) f_y vs. W_{bs}

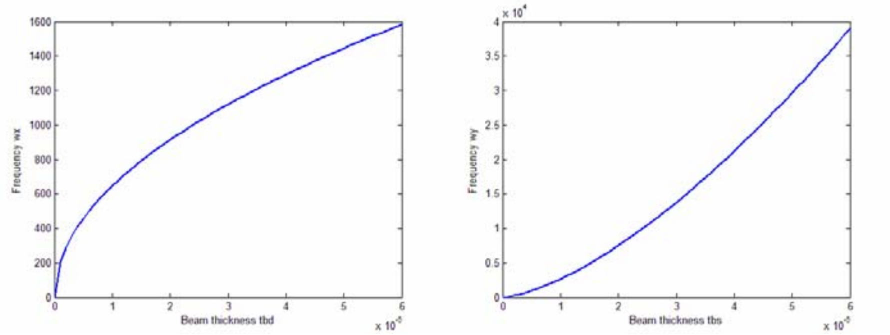

(c) f_x vs. t_{bd} (f) f_y vs. t_{bs}

Figure 4.11 Dependence of resonant frequency on beam size: (a)-(c) resonant frequency in driving mode vs. size of the driving beams; (d)-(f) resonant frequency in sensing mode vs. size of the sensing beams.

4.3.2 Air Damping Coefficient

In the driving mode, the driving mass moves along x-direction and the slide-film air damping is the main factor to be considered. According to the previous discussion,

$$c_x = -\frac{\mu A}{d_0}, \tag{4.17}$$

where μ is the coefficient of viscosity, and $\mu = 18.2\times10^{-6}\ \text{Pa}\cdot\text{sec}$ at room temperature; A is the area of the rectangular surface of the central moving mass; d_0 is the distant from the surface of the moving mass to the glass substrate.

In the sensing mode, the sensing mass moves along z-direction and the squeeze-film air damping is the main factor to be considered. According to the previous discussion,

$$c_y = -\frac{\mu L B^3}{d_0^{\ 3}}\beta\left(\frac{B}{L}\right), \tag{4.18}$$

where L and B are the length and width of the rectangular surface; $\beta\left(\frac{B}{L}\right)$ is a function of width-length ratio B/L. For a very long surface, $\beta = 1$; and for a square surface, $\beta = 0.42$.

With the design parameters in Table 4.3, we can calculate the gyroscope air damping coefficients

$$c_x = 2.302\times10^{-5} N.\text{sec}/m \text{ and } c_y = 0.619 N.\text{sec}/m, \tag{4.19}$$

and the damping ratios

$$\zeta_x = 2.483\times10^{-3} \text{ and } \zeta_y = 97.22. \tag{4.20}$$

Obviously, the damping ratio for the driving mode meets the requirement of light damping ($\zeta < 0.7$). But the damping ratio for the sensing mode is too large ($\zeta > 0.7$) because of the squeeze-film air damping. Therefore, we need to use vacuum package for the gyroscope to reduce the squeeze-film air damping effect.

4.3.3 Differential Equation Solving

To get the sensitivity of our device, we need to know the displacement in x- and y-direction under certain angular velocity. Therefore, we need to solve the differential equations (4.1) and (4.2).

Equation (4.1) is a second-order linear differential equation with one function $x(t)$ to be determined, whereas equation (4.2) is another second-order differential equation with two functions $x(t)$ and $y(t)$ to be determined. Therefore, it is easier for us to solve equation (4.1) first, and then substitute the solution $x(t)$ into equation (4.2) and solve it with a similar approach.

(1) Solution to Equation (4.1)

Equation (4.1) is a second-order non-homogeneous linear differential equation. The general solution of a non-homogeneous differential equation takes form

$$x(t) = x_1(t) + x_2(t), \tag{4.21}$$

where $x_1(t)$ is the general solution of the homogeneous linear differential equation by setting the right side of the original non-homogeneous linear differential equation to zero; and $x_2(t)$ is a particular solution of the non-homogeneous linear differential equation.

In our case, the homogeneous equation for $x_1(t)$ is

$$M_d \frac{d^2x(t)}{dt^2} + c_x \frac{dx(t)}{dt} + k_x x(t) = 0 . \tag{4.22}$$

We can write the characteristic equation of the differential equation (4.22) as

$$M_d r^2 + c_x r + k_x = 0 . \tag{4.23}$$

The roots r_1 and r_2 of this characteristic equation can be found by using the quadratic formula

$$r_{1,2} = \frac{-c_x \pm \sqrt{c_x{}^2 - 4M_d k_x}}{2M_d} . \tag{4.24}$$

We distinguish three cases according to the sign of the term $c_x{}^2 - 4M_d k_x$:

(a) Under-damping

If $c_x{}^2 < 4M_d k_x$, the roots r_1 and r_2 of this characteristic equation are a pair of conjugate complex numbers. And the solution of the differential equation can be written in the form of

$$x_1(t) = e^{\alpha t}(C_1 \cos\beta t + C_2 \sin\beta t) , \tag{4.25}$$

where $\alpha = -\frac{c_x}{2M_d}$ and $\beta = \frac{\sqrt{4M_d k_x - c_x{}^2}}{2M_d}$, which are derived from the roots of the differential equation; C_1 and C_2 are constants to be determined by the initial conditions.

Letting $C_1 = A\sin\varphi$ and $C_2 = A\cos\varphi$ ($0 \le \varphi < 2\pi$), we can have

$$\begin{aligned} x_1(t) &= e^{\alpha t}(A\sin\varphi\cos\beta t + A\cos\varphi\sin\beta t) \\ &= Ae^{\alpha t}\sin(\beta t + \varphi) . \end{aligned} \tag{4.26}$$

In under-damping condition, the mass will have an oscillation, but the amplitude of the vibration decays exponentially with time.

(b) Over-damping

If $c_x{}^2 > 4M_d k_x$, the roots r_1 and r_2 of this characteristic equation are real and distinct numbers. And the solution of the differential equation can be written in the form of

$$\begin{aligned} x_1(t) &= C_1 e^{r_1 t} + C_2 e^{r_2 t} \\ &= e^{\alpha t}(C_1 e^{\beta t} + C_2 e^{-\beta t}) , \end{aligned} \tag{4.27}$$

where $\alpha = -\frac{c_x}{2M_d}$ and $\beta = \frac{\sqrt{c_x{}^2 - 4M_d k_x}}{2M_d}$, which are derived from the roots of the differential equation; C_1 and C_2 are constants to be determined by the initial conditions.

In over-damping condition, there is no oscillation of the displacement, and the mass returns to its balanced position slowly.

(c) Critical-damping

If ${c_x}^2 = 4M_d k_x$, the roots r_1 and r_2 of this characteristic equation are real and equal numbers. Let's denote the common value of r_1 and r_2 by r. The solution of the differential equation can be written in the form of

$$\begin{aligned} x_1(t) &= C_1 e^{rt} + C_2 t e^{rt} \\ &= e^{\alpha t}(C_2 t + C_1)\,, \end{aligned} \tag{4.28}$$

where $\alpha = -\dfrac{c_x}{2M_d}$, which is derived from the roots of the differential equation; C_1 and C_2 are constant to be determined by the initial conditions.

In critical-damping, there is no oscillation of the displacement, but the time taken for the displacement to become zero is a minimum.

In all the above three cases, constants C_1 and C_2 are to be determined by the initial conditions. Because we assumed that the external force $F_d(t)$ is exerted to the system from time $t = 0$, the initial displacement and velocity of the driving mass on the x-direction at $t = 0$ are

$$\begin{aligned} x(t)\big|_{t=0} &= 0\,, \\ \left.\frac{dx(t)}{dt}\right|_{t=0} &= 0\,. \end{aligned} \tag{4.29}$$

To satisfy the initial conditions, the general solution $x_1(t)$ of the homogeneous linear differential equation (4.22) has to be zero.

In actual case, the general solution $x_1(t)$ contributes to the transient oscillations, which are usually short-lived and can be ignored in most of cases. We will only need to consider what happens when conditions are steady, which is determined by the particular solution $x_2(t)$.

Since the right side of the differential equation (4.1) is $F_d(t) = F_0 \cos w_d t$, we can try the particular solution as

$$x_2(t) = a\cos w_d t + b\sin w_d t\,, \tag{4.30}$$

where a and b are coefficients whose value can be determined by substituting the particular solution $x_2(t)$ in the differential equation. The left side of the differential equation is

$$\begin{aligned} & M_d \frac{d^2 x_2(t)}{dt^2} + c_x \frac{dx_2(t)}{dt} + k_x x_2(t) \\ &= M_d(-a{w_d}^2 \cos w_d t - b{w_d}^2 \sin w_d t) + c_x(-aw_d \sin w_d t + bw_d \sin w_d t) + k_x(a\cos w_d t + b\sin w_d t) \\ &= (-M_d {w_d}^2 a + c_x w_d b + k_x a)\cos w_d t + (-M_d {w_d}^2 b - c_x w_d a + k_x b)\sin w_d t\,. \end{aligned} \tag{4.31}$$

Comparing coefficients with the right side of the differential equation $F_0 \cos w_d t$, we have

$$\begin{aligned}&-M_d {w_d}^2 a + c_x w_d b + k_x a = F_0\,,\\&-M_d {w_d}^2 b - c_x w_d a + k_x b = 0\,.\end{aligned} \tag{4.32}$$

i.e.,

$$\begin{aligned}&(k_x - M_d {w_d}^2) a + c_x w_d b = F_0\,,\\&-c_x w_d a + (k_x - M_d {w_d}^2) b = 0\,.\end{aligned} \tag{4.33}$$

Solving the above set of equations, we get

$$\begin{aligned}a &= \frac{F_0 (k_x - M_d {w_d}^2)}{(k_x - M_d {w_d}^2)^2 + (c_x w_d)^2}\,,\\ b &= \frac{F_0 c_x w_d}{(k_x - M_d {w_d}^2)^2 + (c_x w_d)^2}\,.\end{aligned} \tag{4.34}$$

From what has been discussed above, we have the general solution of a non-homogeneous differential equation (4.1) as

$$\begin{aligned}x(t) &= x_1(t) + x_2(t)\\ &= a\cos w_d t + b\sin w_d t\,.\end{aligned} \tag{4.35}$$

In our vibrating model, we specially choose the driving frequency w_d to be equal to the resonant frequency along x-direction w_x in order to have the driving direction displacement of the mass reach the maximum value. According to the definition of resonant frequency $w_x = \sqrt{\frac{k_x}{M_d}}$, the coefficients

$$\begin{aligned}a &= \frac{F_0 (k_x / M_d - {w_d}^2)}{(k_x / M_d - {w_d}^2)^2 + (c_x w_d)^2 / M_d}\\ &= \frac{F_0 ({w_x}^2 - {w_d}^2)}{({w_x}^2 - {w_d}^2)^2 + (c_x w_d)^2 / M_d}\\ &= 0\,,\end{aligned} \tag{4.36}$$

$$\begin{aligned}b &= \frac{F_0 c_x w_d / M_d}{(k_x / M_d - {w_d}^2)^2 + (c_x w_d)^2 / M_d}\\ &= \frac{F_0 c_x w_d / M_d}{({w_x}^2 - {w_d}^2)^2 + (c_x w_d)^2 / M_d}\\ &= \frac{F_0}{c_x w_x}\,.\end{aligned} \tag{4.37}$$

Therefore, the solution of equation (4.1) can be simplified as

$$x(t) = \frac{F_0}{c_x w_x} \sin w_x t\,. \tag{4.38}$$

Let's denote the amplitude of x-direction motion by x_m. Then the solution of equation (4.1) can be written as

$$x(t) = x_m \sin w_x t\,. \tag{4.39}$$

(2) Solution to Equation (4.2)

Substituting the solution $x(t) = x_m \sin w_x t$ in to equation (4.2), we get

$$M_s \frac{d^2 y(t)}{dt^2} + c_y \frac{dy(t)}{dt} + k_y y(t) = 2M_s \Omega w_x x_m \cos w_x t \,. \tag{4.40}$$

It takes almost the same form with equation (4.1). In a very similar way, we can get the solution for equation (4.2):

$$y(t) = c \cos w_x t + d \sin w_x t \,, \tag{4.41}$$

where

$$\begin{aligned} c &= 2M_s \Omega w_x x_m \cdot \frac{(k_y - M_s w_x{}^2)}{(k_y - M_s w_x{}^2)^2 + (c_y w_x)^2} \,, \\ d &= 2M_s \Omega w_x x_m \cdot \frac{c_y w_x}{(k_y - M_s w_x{}^2)^2 + (c_y w_x)^2} \,. \end{aligned} \tag{4.42}$$

Letting $c = B\sin\theta$ and $d = B\cos\theta$ ($0 \le \theta < 2\pi$), we can have

$$\begin{aligned} y(t) &= B\sin\theta \cos w_x t + B\cos\theta \sin w_x t \\ &= B\sin(w_x t + \theta) \,. \end{aligned} \tag{4.43}$$

Because $c^2 + d^2 = (B\sin\theta)^2 + (B\cos\theta)^2 = B^2(\sin^2\theta + \cos^2\theta) = B^2$,

$$B = \sqrt{c^2 + d^2} = 2M_s \Omega w_x x_m \cdot \frac{1}{\sqrt{(k_y - M_s w_x{}^2)^2 + (c_y w_x)^2}} \,, \tag{4.44}$$

$$\theta = \arctan \frac{k_y - M_s w_x{}^2}{c_y w_x} \,. \tag{4.45}$$

According to the definition of resonant frequency $w_y = \sqrt{\dfrac{k_y}{M_s}}$,

$$\begin{aligned} B &= 2\Omega w_x x_m \cdot \frac{1}{\sqrt{(k_y / M_s - w_x{}^2)^2 + (c_y w_x / M_s)^2}} \\ &= 2\Omega w_x x_m \cdot \frac{1}{\sqrt{(w_y{}^2 - w_x{}^2)^2 + (c_y w_x / M_s)^2}} \\ &= \frac{2\Omega w_x x_m}{w_y{}^2} \cdot \frac{1}{\sqrt{[1 - (w_x / w_y)^2]^2 + (c_y w_x / M_s w_y{}^2)^2}} \,. \end{aligned} \tag{4.46}$$

According to the definition of quality factor $Q_y = \dfrac{M_s w_y}{c_y}$,

$$B = \frac{2\Omega w_x x_m}{w_y{}^2} \cdot \frac{1}{\sqrt{[1 - (w_x / w_y)^2]^2 + (w_x / w_y Q_y)^2}} \,. \tag{4.47}$$

Again, using the definition of resonant frequency $w_y{}^2 = \frac{k_y}{M_s}$,

$$B = \frac{2M_s\Omega w_x x_m}{k_y} \cdot \frac{1}{\sqrt{[1-(w_x/w_y)^2]^2 + (w_x/w_y Q_y)^2}} . \tag{4.48}$$

Again, using the definition of resonant frequency $w_y{}^2 = \frac{k_y}{M_s}$,

$$\begin{aligned} \theta &= \arctan \frac{k_y/M_s - w_x{}^2}{c_y w_x / M_s} \\ &= \arctan \frac{w_y{}^2 - w_x{}^2}{c_y w_x / M_s} \\ &= \arctan \frac{1-(w_x/w_y)^2}{c_y w_x / M_s w_y{}^2} . \end{aligned} \tag{4.49}$$

Again, using the definition of quality factor $Q_y = \frac{M_s w_y}{c_y}$,

$$\theta = \arctan \frac{1-(w_x/w_y)^2}{w_x/w_y Q_y} . \tag{4.50}$$

From what discussed above, the solution of equation (4.2) can be simplified as

$$y(t) = y_m \sin(w_x t + \theta), \tag{4.51}$$

where

$$y_m = \frac{2M_s\Omega w_x x_m}{k_y} \cdot \frac{1}{\sqrt{[1-(w_x/w_y)^2]^2 + (w_x/w_y Q_y)^2}} , \tag{4.52}$$

$$\theta = \arctan \frac{1-(w_x/w_y)^2}{w_x/w_y Q_y} . \tag{4.53}$$

According to Equation (4.51) and (4.53), when resonant frequencies in x- and y-direction are precisely matched ($w_x = w_y$), it gives $\theta = 0$ and $y(t) = y_m \sin(w_x t)$. At the same time, $x(t) = x_m \sin(w_x t)$. This means that the central movable mass will oscillate along a linear path at an angle to the x-axis, as shown in Figure 4.12.

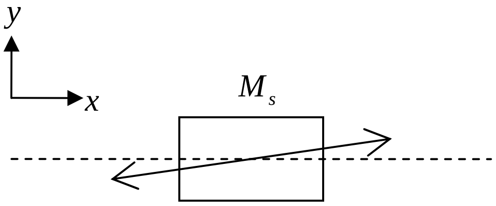

Figure 4.12 Oscillatory motion of the central mass for $\theta = 0$

4.3.4 Sensitivity

The gyroscope displacement sensitivity is defined as the sensing vibration amplitude of the central mass in response to unit angular velocity. It can be expressed as

$$S_d = \frac{dy_m}{d\Omega} = \frac{2x_m}{\omega_y} \cdot \frac{\omega_x / \omega_y}{\sqrt{\left[1-\left(\omega_x / \omega_y\right)^2\right]^2 + \frac{1}{Q_y^{\,2}}\left(\omega_x / \omega_y\right)^2}} \,. \tag{4.54}$$

Figure 4.13 shows the relationship between displacement sensitivity and the size of the driving and sensing beams.

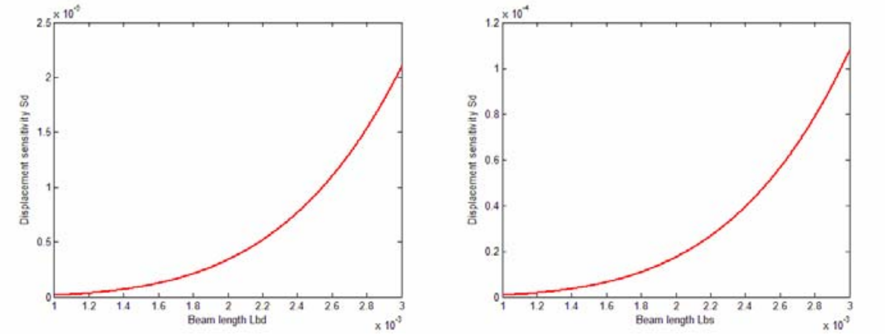

(a) S_d vs. L_{bd} (d) S_d vs. L_{bs}

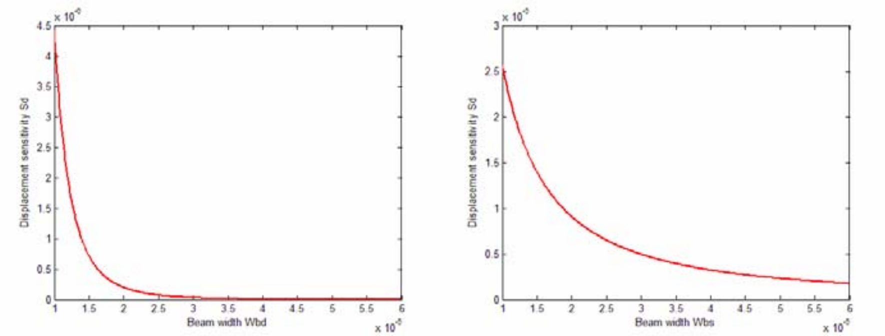

(b) S_d vs. W_{bd} (e) S_d vs. W_{bs}

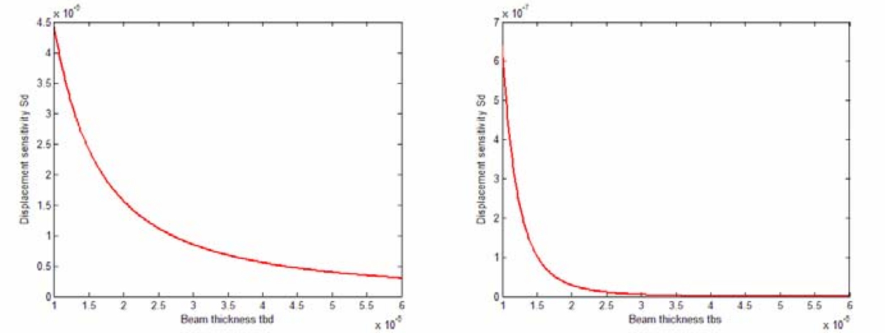

(c) S_d vs. t_{bd} (f) S_d vs. t_{bs}

Figure 4.13 Dependence of displacement sensitivity on beam size: (a)-(c) displacement sensitivity vs. size of the driving beams; (d)-(f) displacement sensitivity vs. size of the sensing beams.

From Figure 4.13, we can have the following conclusions: (1) displacement sensitivity increase as the beam length increase; (2) displacement sensitivity decrease as the beam width increase; (3) displacement sensitivity decrease as the beam thickness increase.

Theoretically, we can extend the beam length and shrink the beam width and thickness to achieve very high displacement. However, the device frequency may also be affected when the beam size is changed. Comparing Figure 4.11 and 4.13, we can see that the resonant frequency and the displacement sensitivity always increase in one, decrease in the other; or decrease in one, increase in the other. A very low frequency will make the system unstable. Therefore, there is a trade-off between device resonant frequency and sensitivity, and we may choose a moderate beam size to make both of them meet the minimum requirements.

We can express the displacement sensitivity in Equation (4.54) in a normalized way:

$$S_{dn} = \frac{\omega_y}{2x_m} \cdot S_d = \frac{\omega_x / \omega_y}{\sqrt{\left[1-\left(\omega_x / \omega_y\right)^2\right]^2 + \frac{1}{Q_y{}^2}\left(\omega_x / \omega_y\right)^2}}. \tag{4.55}$$

Figure 4.14 shows the relationship between the normalized sensitivity S_{dn} and (ω_x / ω_y) for different Q_y values. From the curves, we can see that the displacement sensitivity takes its peak value at $(\omega_x / \omega_y) = 1$. With the increase of Q_y, the peak will become narrower and sharper. For example, if $Q_y = 5000$, S_{dn} is 5000 when $(\omega_x / \omega_y) = 1$. However, if $(\omega_x / \omega_y) = 0.95$ or 1.05 (5% mismatch between ω_x and ω_y), S_{dn} drops rapidly to 10 (about 500 times smaller). This indicates that in order to ensure enough sensitivity, it is very important to precisely match the resonant frequencies of driving and sensing modes. Increase Q factors of vibration can also help improve the sensitivity.

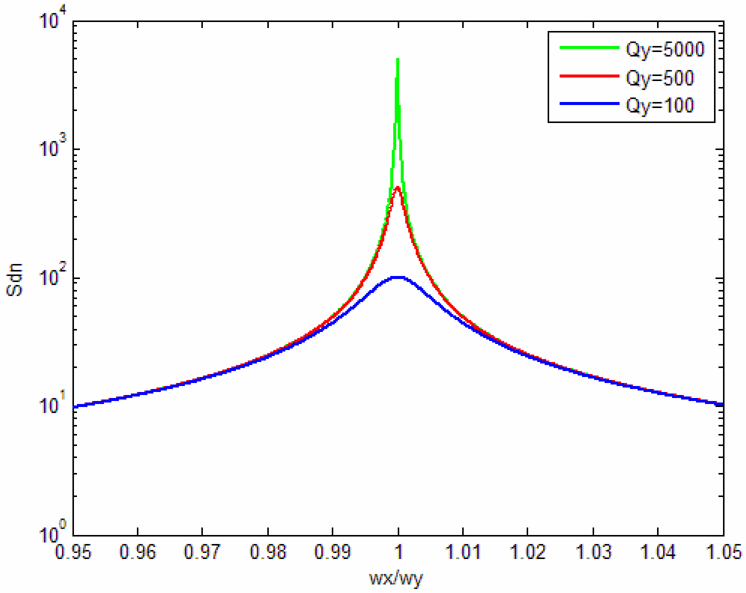

Figure 4.14. S_{dn} vs. (ω_x / ω_y) for different Q_y values

Based on the definition of differential capacitance in Section 3.3, $\Delta C = 2C_0(x/d_0)$, therefore, the capacitance sensitivity of the gyroscope can be expressed as

$$S_c = \frac{2C_0}{d_0} S_d \,, \tag{4.56}$$

where d_0 is the capacitance gap and C_0 is the static capacitance. According to the design parameters in Table 4.3,

$$d_0 = 10\mu m \text{ and } C_0 = 6.942 pF \,. \tag{4.57}$$

Figure 4.15 plots output capacitance change versus input angular velocity based on theoretical calculation. From the plot, we can see that the device truly works as an angular rate sensor.

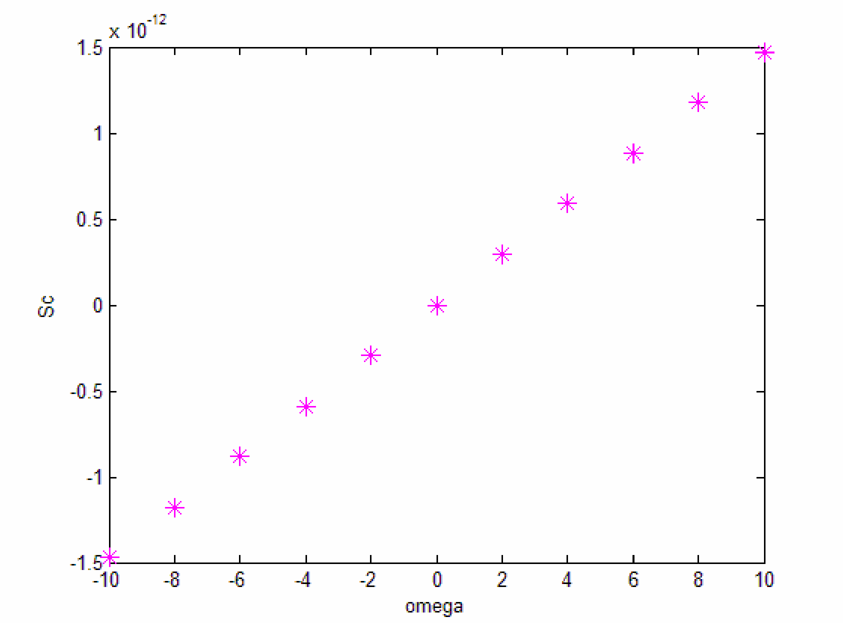

Figure 4.15 Capacitance change ΔC vs. angular velocity Ω

4.4 Electrostatic Tuning

Due to process variation, the fabrication may cause deviations in resonant frequencies of driving and sensing modes, even if we precisely match them in theoretical calculation. Hence here we intentionally set f_y to be a little larger than f_x. (From the previous discussion, we know that resonant frequency of the driving and sensing modes are chosen to be $f_x = 289.0Hz$ and $f_y = 302.1Hz$, and f_y is 3.8% larger than f_x). Then a DC biasing voltage can be used to tune down f_y in differential capacitance sensing to precisely match the value of f_x. This technique is called electrostatic tuning.

In our design, there are two electrodes deposited on each of the top and bottom glass substrate. One electrode is to detect the capacitance change; the other one is to tune down resonant frequency in sensing mode (see Figure 4.16).

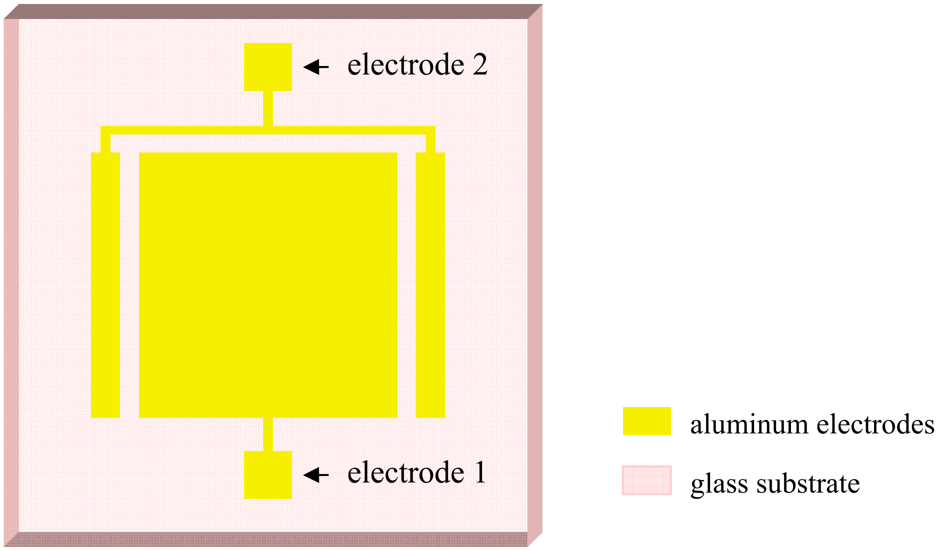

Figure 4.16 Electrodes on glass substrate: electrode 1 is for capacitance sensing; electrode 2 is for frequency tuning.

During electrostatic tuning, we apply to top and bottom frequency tuning electrodes with DC biasing voltage $\pm V_d$, which have the same magnitude but different polarity. So the electrostatic forces to the central mass from top and bottom frequency tuning electrodes are

$$F_{e1} = \frac{\varepsilon S V_d^{\,2}}{2(d_0 - x - \Delta x)^2}, \qquad F_{e2} = \frac{\varepsilon S V_d^{\,2}}{2(d_0 + x + \Delta x)^2}. \tag{4.58}$$

where S is the area of the frequency tuning electrode; d_0 is the static capacitance gap; x is the displacement of the central mass due to Coriolis force; and Δx is the displacement due to electrostatic tuning force.

When $x \ll d_0$ and $\Delta x \ll d_0$ (d_0 is in the scale of μm, x and Δx are in the scale of nm in our gyroscope design), the total electrostatic force experienced by the central mass is

$$F_e = F_{e1} - F_{e2} \approx \frac{2\varepsilon S V_d^{\,2}(x + \Delta x)}{d_0^{\,3}}. \tag{4.59}$$

The electrostatic force introduced to the system is equivalent to the effect of a negative spring constant:

$$\Delta k = -\frac{dF_e}{dx} = -\frac{2\varepsilon S V_d^{\,2}}{d_0^{\,3}}. \qquad (4.60)$$

If $\Delta k \ll k_y$, the effective resonant frequency in sensing mode after electrostatic tuning can be expressed as

$$f_e = \frac{1}{2\pi}\sqrt{\frac{k_y + \Delta k}{M_s}} = f_y\left(1 - \frac{\varepsilon S V_d^{\,2}}{k_y d_0^{\,3}}\right). \qquad (4.61)$$

Therefore, the change in resonant frequency in sensing mode after electrostatic tuning is

$$\Delta f = f_e - f_y = -\frac{\varepsilon S V_d^{\,2}}{k_y d_0^{\,3}} f_y. \qquad (4.62)$$

From the analysis above, we can plot the expected effective resonant frequency f_e of the gyroscope under a certain biasing DC voltage V_d, as shown in Figure 4.17. When there is no biasing voltage, $f_e = f_y = 302.1Hz$; when there is a 5V biasing voltage, f_e is tuned down to 215.4Hz, which is significantly decreased compared to the original value; when there is a 1.94V biasing voltage, we may achieve $f_e = f_x = 289.0Hz$, thus eliminating the frequency mismatch.

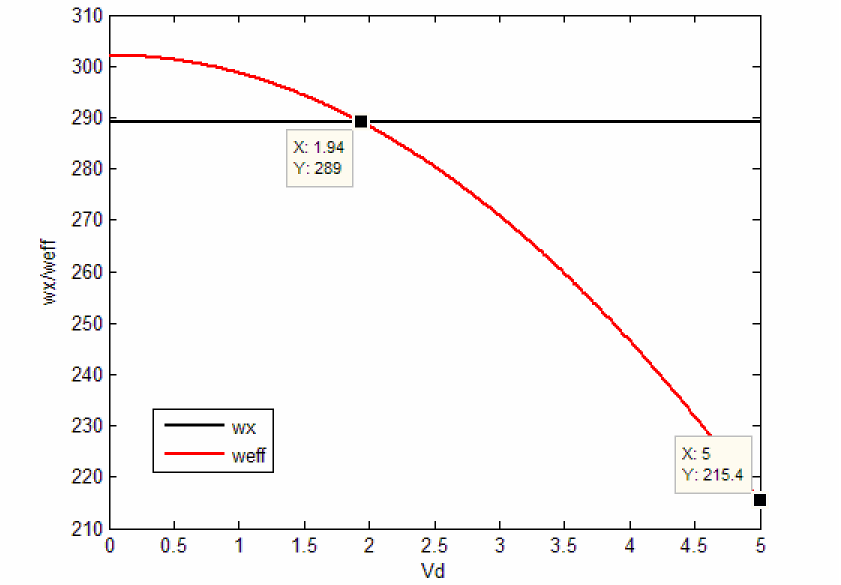

Figure 4.17 Effective resonant frequency by varying the DC tuning voltage

CHAPTER V. PERFORMANCE AND SIMULATION

5.1 Performance

If the microgyroscope is packaged in a vacuum state, and the air pressure is pumped down to is a certain extent (10^2~10^3 Pa), we believe we can achieve high quality factors in both driving and sensing mode for our device. Assume the quality factors $Q_x = 200$ and $Q_y = 200$, we can have the performance parameters of the microgyroscope, which are listed in Table 5.1.

From the table, we can see that the displacement sensitivity has a value of 105.9nm/(°/sec) and capacitance sensitivity has a value of 13.88 fF/(°/sec), which is a great improvement compared to the previous designs. The gyroscope is expected to have a wide application for its high sensitivity and good performance.

Table 5.1 Performance parameters of the novel gyroscope

Performance Parameters	**Values**
Static capacitance C_0	6.942pF
Driving mass M_d	1.678mg
Sensing mass M_s	2.570mg
Driving mode spring constant k_x	8.476N/m
Sensing mode spring constant k_y	6.044N/m
Driving mode resonant frequency f_x	289.0Hz
Sensing mode resonant frequency f_y	302.1Hz
Displacement sensitivity S_d	105.9nm/(°/sec)
Capacitance sensitivity S_c	13.88fF/(°/sec)

5.2 ANSYS Simulation

The dynamic analysis of this gyroscope in Section 4.3 predicts the relationship between device performance parameters (such as beam spring constant, device resonant frequency, air damping coefficient, displacement sensitivity and capacitance sensitivity) and various design parameters (such as beam length, beam width and beam thickness). However, the theoretical calculation is based on the simplified spring-mass model. In order for a more accurate analysis, ANSYS FEM simulation [31] is required to simulate the device resonant frequencies as well as other performance parameters, for example, displacement analysis and stress analysis.

ANSYS software is a general-purpose finite element modeling package for numerically solving mechanical problems, including static/dynamic structural analysis (both linear and non-linear), heat transfer and fluid problems, as well as acoustic and electro-magnetic problems. It has multidisciplinary applications, and can be used in civil engineering, electrical engineering, physics and chemistry field.

At the first step, we need to assign some parameters of silicon material (such as Young's modulus, Poisson's Ratio, density, etc.) to ANSYS. Then, a 3-dimentional model of the microgyroscope is built in the software (see Figure 5.1). After that, the complex structure is divided into basic geometric elements, and this step is called meshing (see Figure 5.2). Now the device is ready for simulation.

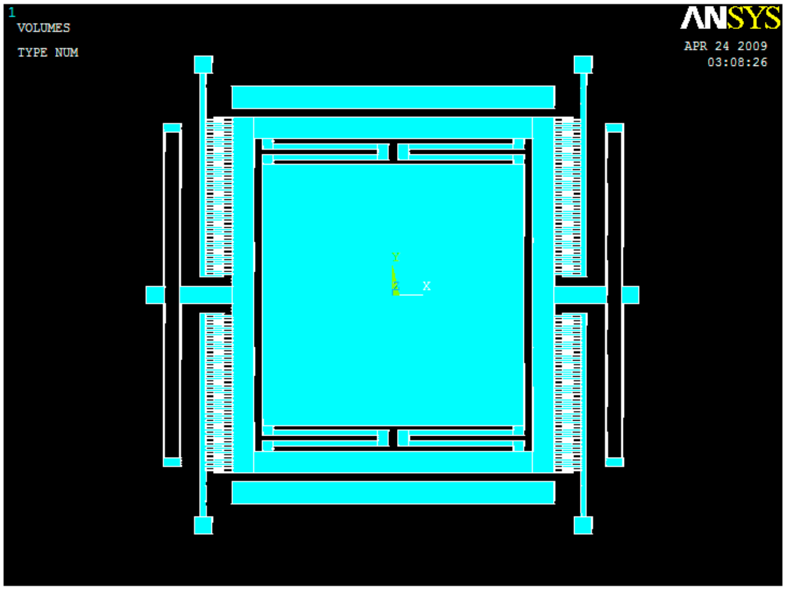

Figure 5.1 3D model of the novel microgyroscope built in ANSYS

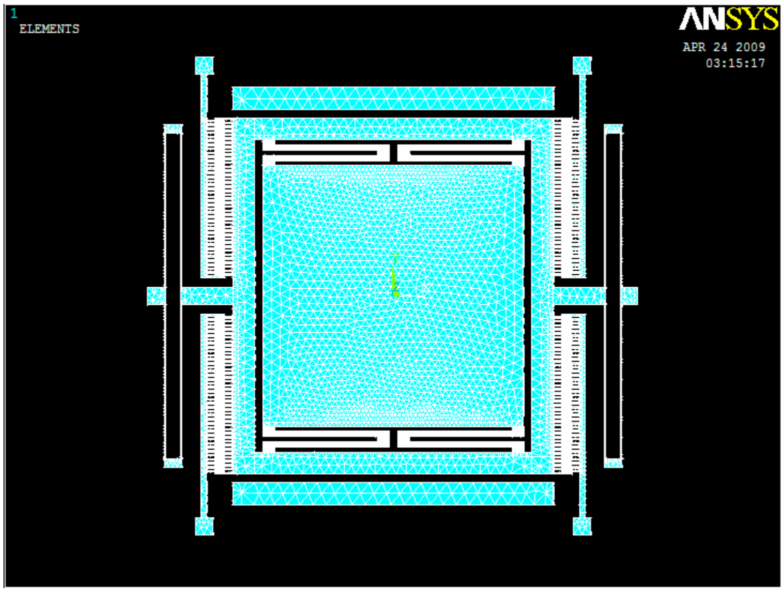

Figure 5.2 Gyroscope model in ANSYS after meshing

5.2.1 Frequency Simulation

By setting the displacement of anchors to be zero, we can do the resonant frequency simulation for the device. Here we extract the first 10 vibration modes of this gyroscope. To decide which two modes are the driving mode and sensing mode of the gyroscope, the deformed shapes of the first five modes are shown in Figure 5.3-5.7. Note that in the figures, only the movable parts and the anchors are displayed. The fixed comb fingers do not contribute to the resonant frequency of the movable parts, thus they are not shown in the simulation. The deformed shapes in the figures are exaggerated.

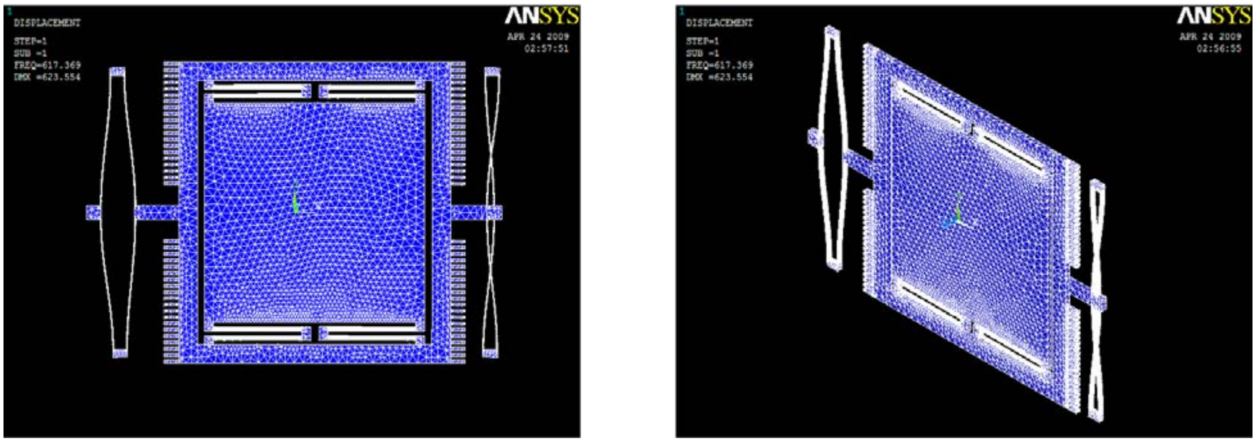

(a) (b)

Figure 5.3 Deformed shape of the gyroscope in the first vibration mode: (a) front view; (b) isometric view.

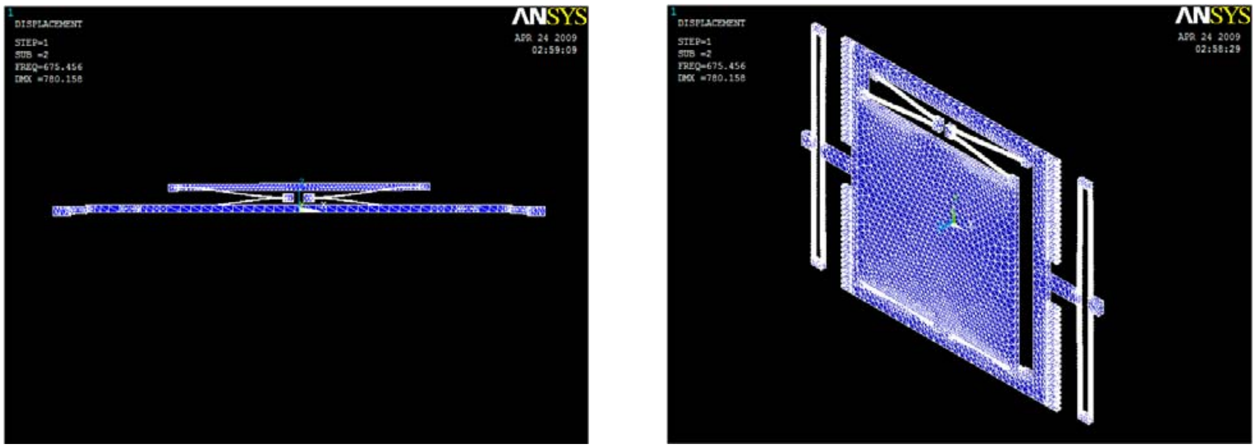

(a) (b)

Figure 5.4 Deformed shape of the gyroscope in the second vibration mode: (a) top view; (b) isometric view.

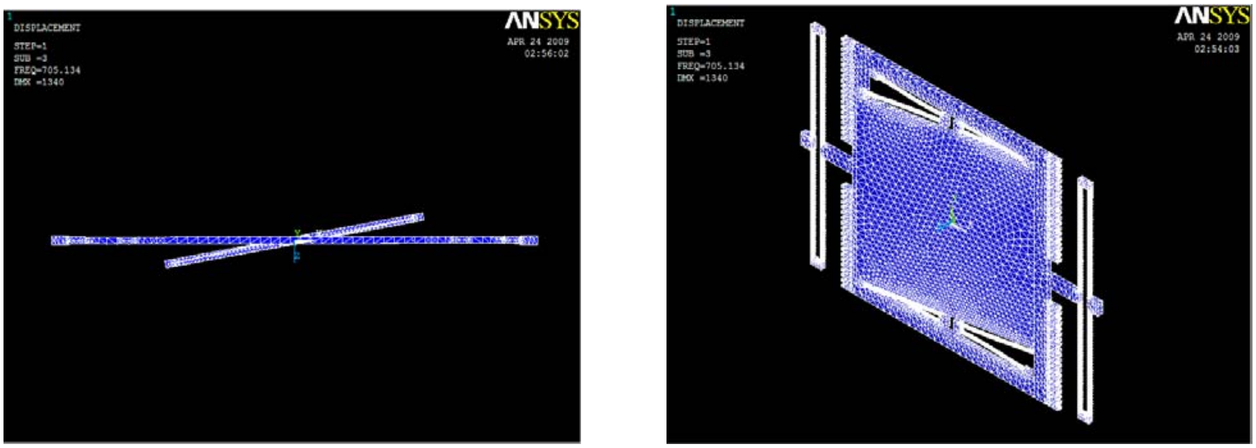

(a) (b)

Figure 5.5 Deformed shape of the gyroscope in the third vibration mode: (a) top view; (b) isometric view.

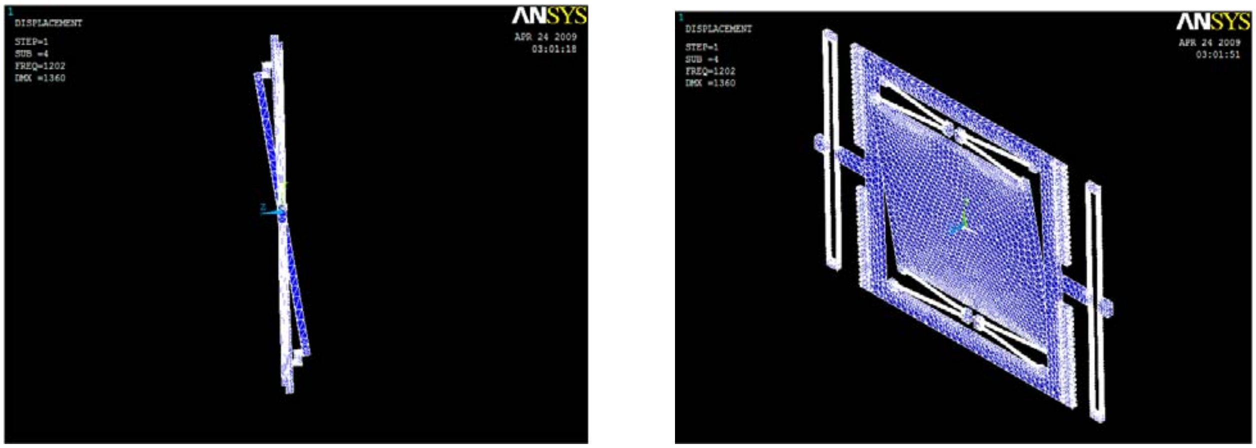

(a) (b)

Figure 5.6 Deformed shape of the gyroscope in the fourth vibration mode: (a) right view; (b) isometric view.

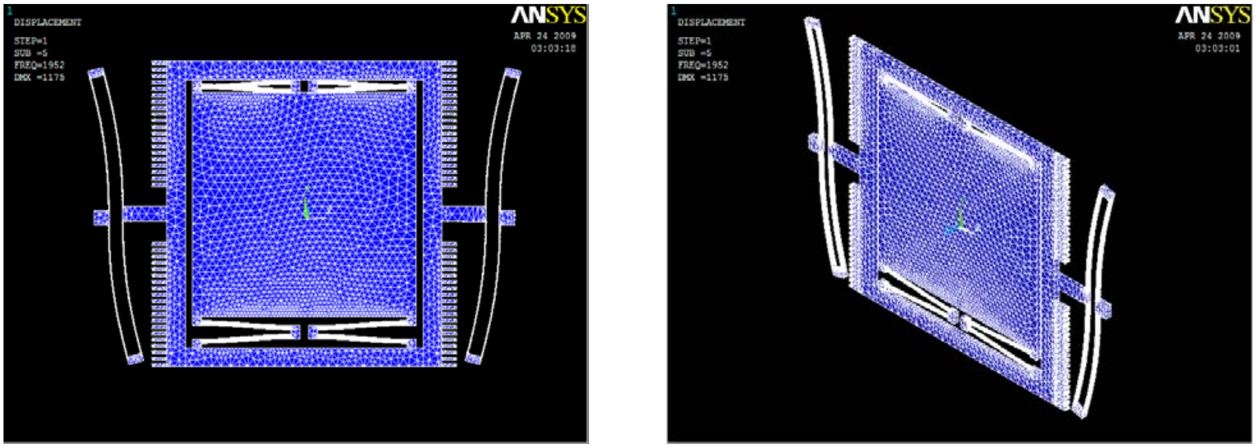

(a) (b)

Figure 5.7 Deformed shape of the gyroscope in the fifth vibration mode: (a) front view; (b) isometric view.

Frequencies of each vibration mode are also extracted from ANSYS, which is shown in Figure 5.8.

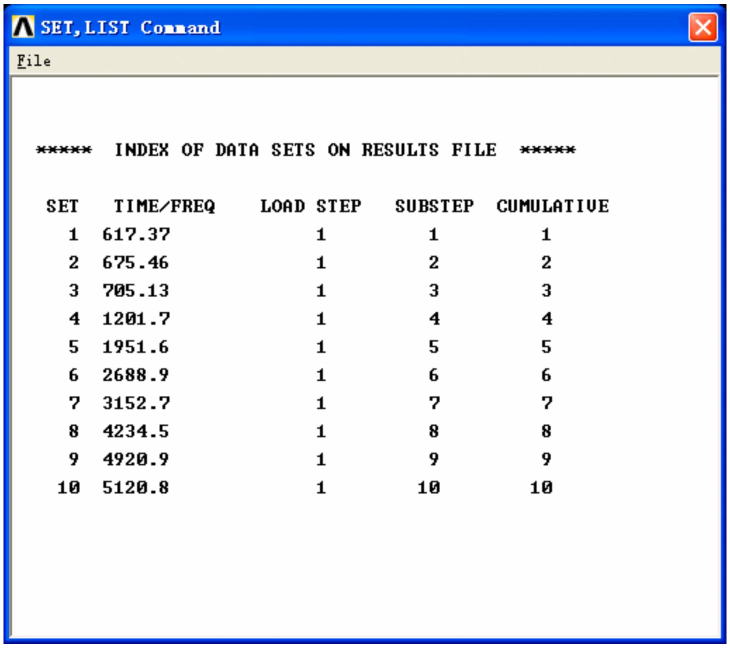

```
 *****  INDEX OF DATA SETS ON RESULTS FILE  *****

  SET   TIME/FREQ    LOAD STEP   SUBSTEP  CUMULATIVE
    1  617.37            1          1         1
    2  675.46            1          2         2
    3  705.13            1          3         3
    4  1201.7            1          4         4
    5  1951.6            1          5         5
    6  2688.9            1          6         6
    7  3152.7            1          7         7
    8  4234.5            1          8         8
    9  4920.9            1          9         9
   10  5120.8            1         10        10
```

Figure 5.8 Resonant frequencies of the first 10 vibration modes of the gyroscope

In Figure 5.3, the central mass and the truss have a great deflection along x-direction, but little deflection along z-direction. We can infer that the first vibration mode is the driving mode of the device. In Figure 5.4, the central mass has a great deflection along z-direction, but little deflection along x-direction. We can infer that the second vibration mode is the driving mode of the device. Therefore, only the first two vibration modes are the working modes of the device. The other vibration modes are the unwanted modes, and should be prevented.

From the simulated results of ANSYS in Figure 5.8, the first two set frequencies are 617.37Hz and 675.46Hz. Therefore, the resonant frequency of the driving mode is 617.37Hz; and the resonant frequency of the sensing mode is 675.46Hz. These results can be very helpful for guiding future research and microfabrication.

The simulated results have a considerable difference with the theoretical calculation fx=289.0Hz and fy=302.1Hz. We believe that ANSYS simulation gives more accurate results. Here are two possible reasons which may cause this mismatch: (1) In calculation, the beam and mass structure is simplified as an ideal spring-mass model, in which the geometric dimension of the mass and mass of the beams are neglected. However, in our device, the vibration system has a distributed mass. (2) ANSYS software takes residual stress, real anchor and plate compliance into consideration, therefore gives a result more close to experimental data [32].

5.2.2 Sensitivity Simulation

Displacement sensitivity of the gyroscope is simulated in ANSYS. Inertial forces are applied to the device in x-direction and z-direction. Different parts of the device with different displacement are displayed with different colors. Parts of the device in red color have a maximum displacement; parts of the device in blue color have a minimum displacement. Figure 5.9 shows the displacement of the gyroscope in driving mode. Figure 5.10 shows the displacement of the gyroscope in sensing mode.

From Figure 5.9 and 5.10, we can see that in the driving mode, the central mass and the truss both have the maximum displacement; in the sensing mode, the central mass has the maximum displacement. The sensing beams are rigid with respect to the x-direction; the driving beams are rigid with respect to the z-direction.

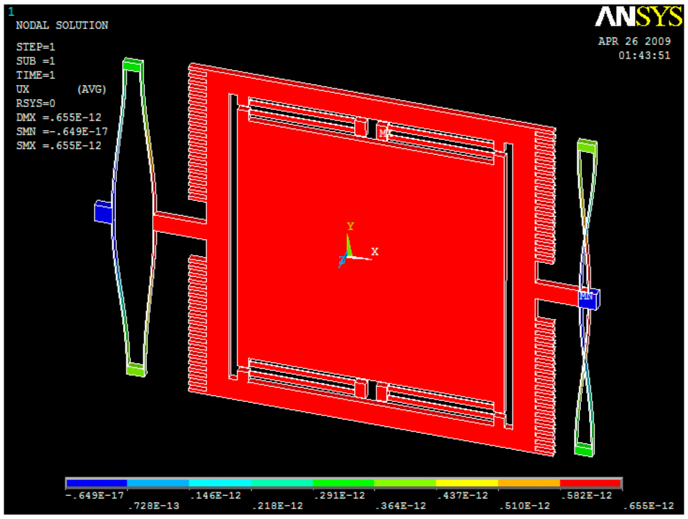

Figure 5.9 Displacement of the gyroscope in driving mode

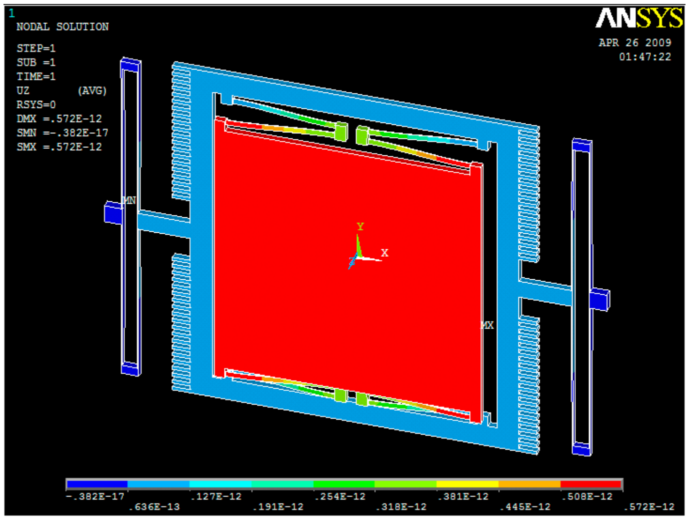

Figure 5.10 Displacement of the gyroscope in sensing mode

5.2.3 Stress Simulation

Stress of the gyroscope under the deflection in driving and sensing modes is simulated in ANSYS. Different parts of the device with different stress are displayed with different colors. Parts of the device in red color have a maximum stress; parts of the device in blue color have a minimum stress. Figure 5.11 shows the stress distribution of the gyroscope in driving mode. Figure 5.12 shows the stress distribution of the gyroscope in sensing mode.

From Figure 5.11 and 5.12, we can see that in the driving mode, the driving beams have the maximum stress; in the sensing mode, the sensing beams have the maximum stress. Inside the beams, the stress is lager at the position where it is close to the anchors or close to the connection of the two beam sections. Therefore, in future design, we may specially make these points strong to sustain more stress.

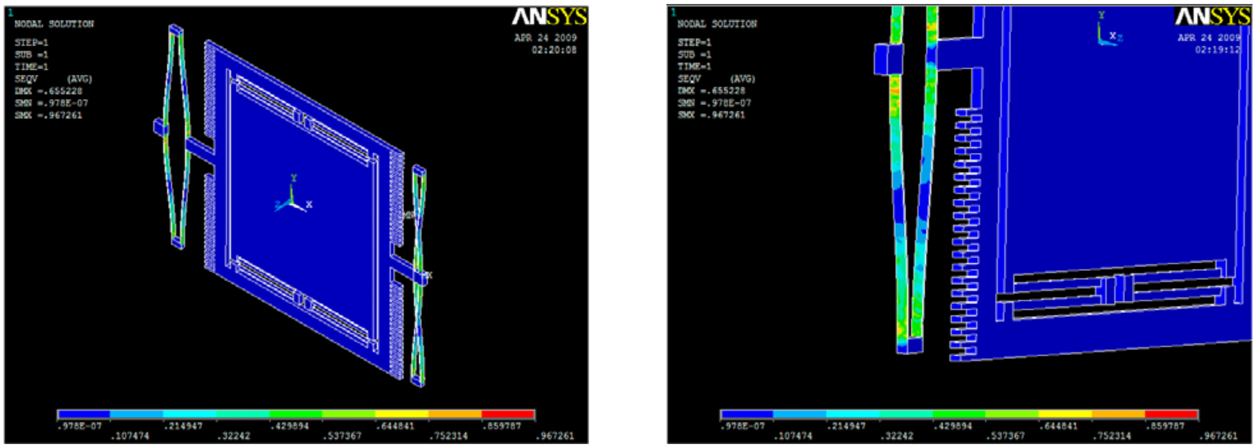

(a) (b)

Figure 5.11 Stress distribution of the gyroscope in driving mode: (a) over-all view; (b) zoom-in view

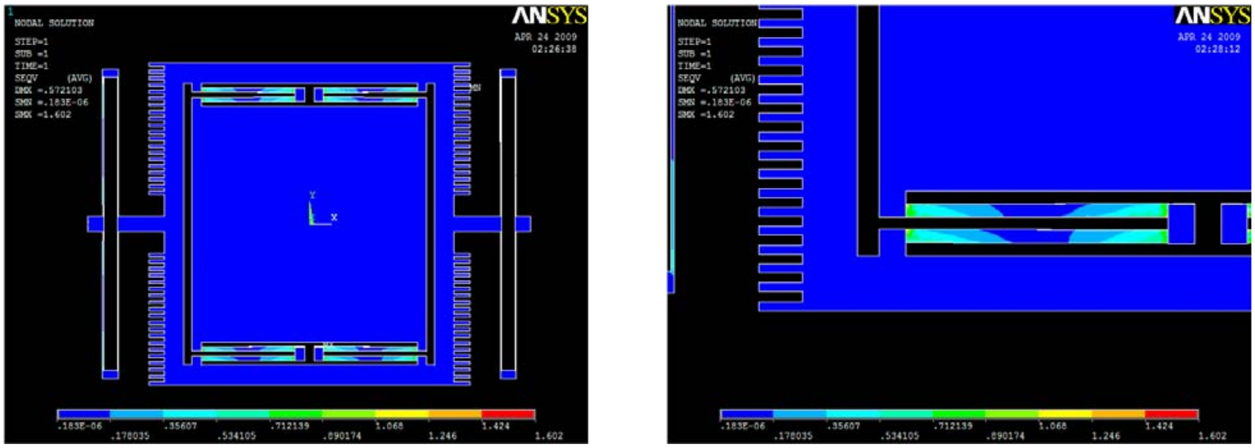

(a) (b)

Figure 5.12 Stress distribution of the gyroscope in sensing mode: (a) over-all view; (b) zoom-in view

CHAPTER VI. FABRICATION

6.1 Fabrication Process

Almost all MEMS process flows could be classified into two primary categories: bulk micromachining and surface micromachining. Bulk micromachining encompasses flows that exploit preferential etching of silicon, glass or other substrates to form micromechanical structures. Surface micromachining flows create microstructures out of thin films on the substrate surface. The MEMS vibratory gyroscope proposed in this research is a bulk micromachining gyroscope.

MEMS fabrication uses the same standard process steps used in integrated circuit manufacturing, including:

- Photolithography
- Oxidation
- Etching
- Diffusion
- Evaporation or sputtering
- Chemical vapor deposition
- Ion implantation
- Epitaxy
- Annealing
- Bonding

In this section, some of these processes used in the MEMS gyroscope fabrication are introduced.

6.1.1 Photolithography

Photolithography is an optical method for transferring patterns on the photolithography masks to the surface of the silicon wafer, which is widely used in MEMS fabrication. The patterns are first transferred from the photolithography mask to a light-sensitive material called photoresist. Chemical or plasma etching is then used to transfer the pattern from the photoresist to the barrier material on the surface of the silicon wafer. A photolithography process is shown in Figure 6.1.

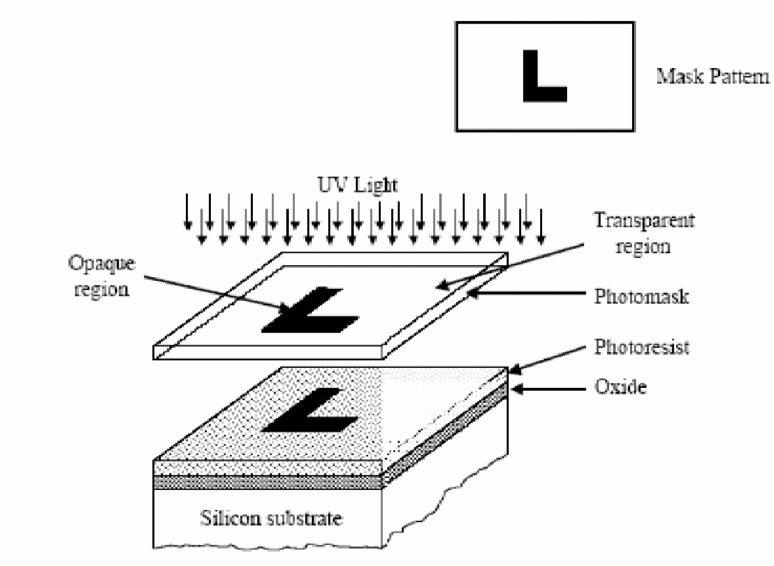

Figure 6.1 Photolithography process

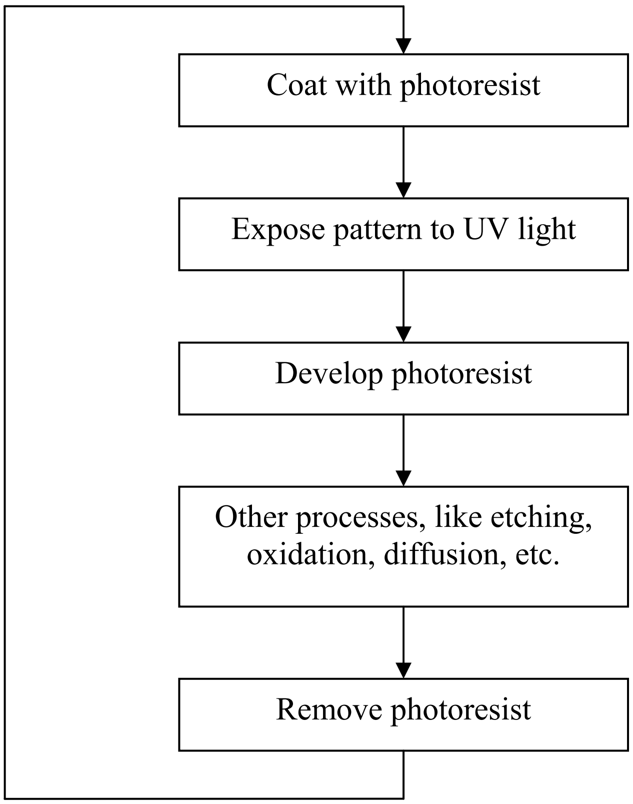

Figure 6.2 Steps in one cycle of photolithography process

Each photolithography cycle requires successful completion of numerous processing steps, for example, photoresist coating, exposure, developing, photoresist removal, and other processes between them. The complexity of MEMS fabrication process is often measured by the number of photolithography masks used during the fabrication. The steps in one cycle of photolithography process are shown in Figure 6.2.

There are two types of photoresist material: positive and negative photoresist. In positive photoresist, the areas that have been exposed to ultraviolet light will be washed away in developing process, leaving bare silicon dioxide in the exposed areas. The mask contains a copy of the pattern that will remain on the surface of the silicon wafer. Windows are opened wherever the exposing light passes through the mask. Reversely, in negative photoresist, the exposed areas will remain on the wafer surface, but the unexposed areas will be washed away. Figure 6.3 shows simple examples of the patterns transferred to a silicon dioxide barrier layer using positive and negative photoresists with the same mask.

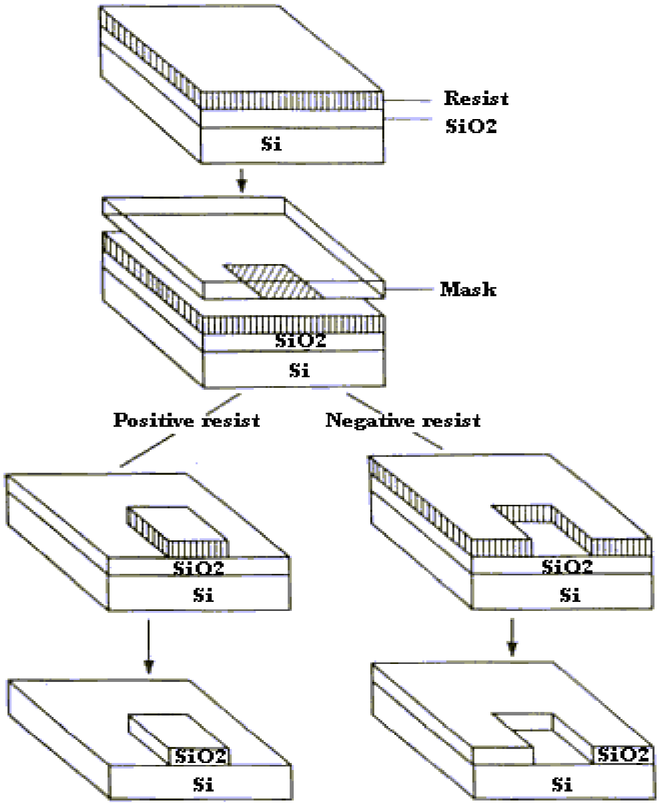

Figure 6.3 Photolithography for positive and negative photoresist materials

6.1.2 *DRIE Etching*

To make stenches in silicon with a high aspect ratio (ratio of geometric depth to width) and with nearly vertical sidewalls, DRIE (Deep Reactive-Ion Etching) is used in patterning the gyroscope structure. DRIE is a combination of plasma etching and ion milling etching. Plasma etching uses corrosive gases and plasma energy to cause chemical reaction. Ion milling uses ion-beam to bombard the wafer surface. Thus, it occurs through both chemical reaction and momentum transfer from the etching species, and is highly anisotropic.

In DRIE process, etch depths of hundreds of microns can be achieved with almost vertical sidewalls (see Figure 6.4). The primary technology is based on two different gas compositions are alternated in the reactor. The first gas composition creates a polymer on the surface of the substrate, and the second gas composition etches the substrate. The polymer is immediately sputtered away by the physical part of the etching, but only on the horizontal surfaces and not the sidewalls. Since the polymer only dissolves very slowly in the chemical part of the etching, it builds up on the sidewalls and protects them from etching. As a result, etching aspect ratios of 50 to 1 can be achieved. The process can easily be used to etch completely through a silicon substrate.

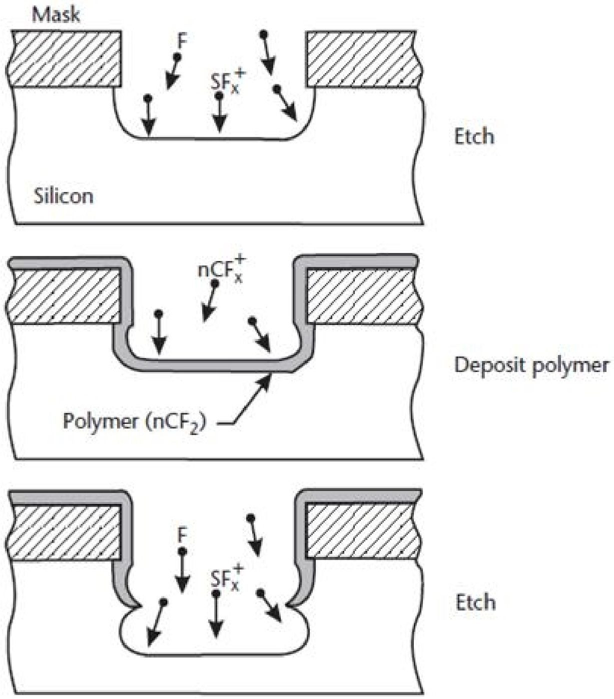

Figure 6.4 Photolithography process. The process cycles between an etch step using SF_6 gas and a polymer deposition step using C_4F_8.

6.1.3 Diffusion

Diffusion is the primary method of introducing impurity atoms (dopants) into silicon wafer to control the number of majority carrier in silicon, and therefore the resistivity of layers formed in the wafer. The most common impurities used as dopants are boron (p-type) and phosphorous (n-type), which can be effectively masked by silicon dioxide layers.

The rate at which dopants diffuse in silicon is a strong function of temperature. At high temperatures (900 to 1200 °C), the impurity atoms move from the surface into the silicon crystal very fast. Therefore, the diffusion process is performed in furnaces, as shown in Figure 6.5.

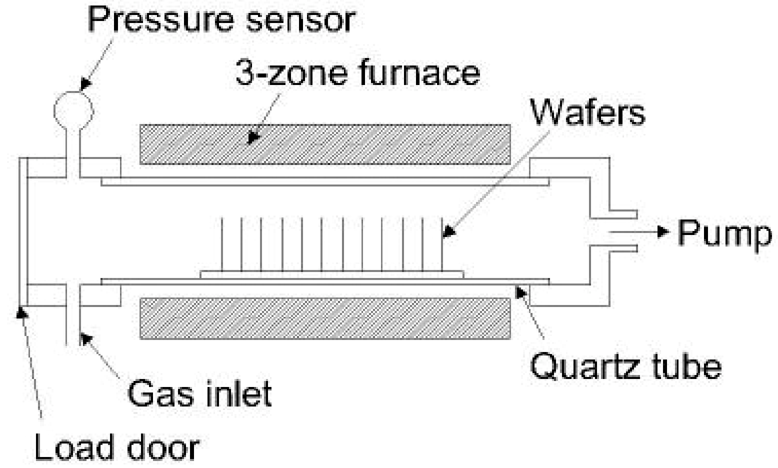

Figure 6.5 Open-furnace-tube diffusion system

6.1.4 Physical Vapor Deposition

Physical vapor deposition (PVD) is a popular method of depositing metal films. Aluminum or gold are heated to the point of vaporization, and then evaporate to form a thin film covering the surface of the silicon wafer. To control the composition of the deposited material, evaporation is performed under vacuum conditions. Figure 6.6 shows a basic vacuum vapor deposition system.

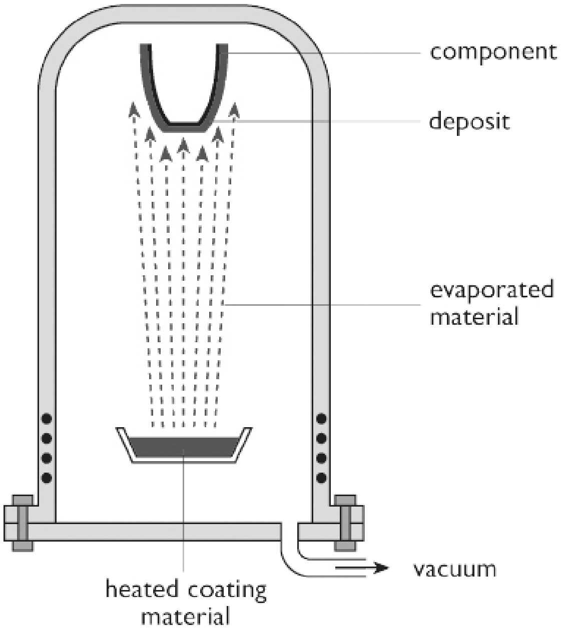

Figure 6.6 Vapor deposition system

6.1.5 Anodic Bonding

Silicon (as well as metals) can be bonded to glass using a low-temperature field assisted anodic bonding process as depicted in Figure 6.7.

The silicon wafer is biased as the electrical anode and the glass substrate as the cathode with an applied voltage as high as 1200V. The sandwich is heated to 300-400°C, and mobile sodium ions in the glass migrate to the cathode leaving fixed charge and a high electric field at the glass-silicon interface supported by image charges in the silicon. The combination of elevated temperature and high field causes chemical bonds to form between the silicon wafer and glass substrate. Glasses with thermal expansion coefficients similar to silicon are utilized to minimize thermal stresses.

Anodic bonding can also be used to join silicon wafers. A thin (a few μm) intermediate layer of glass is sputtered on one of the silicon wafers. The second wafer is brought into contact with the glass layer, and the two wafers are anodically bonded.

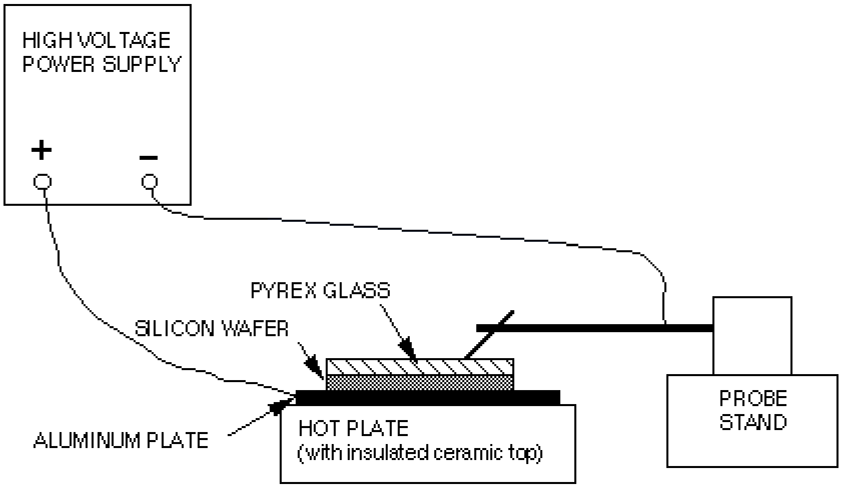

Figure 6.7 Silicon-glass anodic bonding process

6.2 Fabrication Flow

The MEMS gyroscope proposed in this research is to be fabricated with bulk-micromachining process. The fabrication flow of the device is shown in Figure 6.8.

First, the silicon wafer is chemically cleaned to remove particulate matter on the surface, as well as any trace of organic, ionic, and metallic impurities. Hydrofluoric acid is used to remove any oxide that may have formed on the wafer surface. Deionized water is used to remove all traces of ionic, particulate and bacterial contamination.

Then the silicon wafer surface is coated with a photoresist layer. To achieve a uniform thickness, the photoresist is spin coated on to the wafer surface. After that, the silicon wafer is exposed through a photolithography mask to high intensity ultraviolet light. Photoresist is exposed wherever silicon is to be removed. With a properly designed mask, the photoresist areas which cover the movable parts of the gyroscope are exposed.

DRIE technique is used to etch down the silicon layer where there is not cover by photoresist, thus forms the gap between movable parts and the substrate. Due to the symmetrical structure of the device, the patterning and etching are performed on both sides of the wafer simultaneously and precise alignment is required. After DRIE etching, the remaining photoresist material is removed.

Then one more photolithography and DRIE etching is used to release the device gap area. So far, the middle silicon structure of the gyroscope is fabricated.

Diffusion process is used to introduce impurities in the silicon layer, thus the conductivity of the surface layer of silicon structure is increased. Physical vapor deposition method is used to pattern aluminum electrodes on the glass substrates. These two steps are to form the differential capacitance pair of the gyroscope.

Finally, silicon-glass anodic bonding technique is used to bond the silicon structure and the glass substrates together. Now, the whole device is fabricated.

(a) Clean the silicon wafer

(b) Deposit a layer of photoresist material by spin coating

(c) Use photolithography method to pattern the photoresist material

(d) Use DRIE (Deep Reactive- Ion Etching) method to etch down the gap of movable parts

(e) Remove photoresist layer and clean the wafer

(f) Deposit and pattern another photoresist layer by photolithography method

(g) Use DRIE (Deep Reactive- Ion Etching) method to release device gap area

(h) Move away photoresist material

(i) Use Silicon-Glass Anodic Bonding technique to bond silicon structure and glass plates together

Figure 6.8 Fabrication flow of the MEMS gyroscope

6.3 Photolithography Mask

A photolithography mask is usually a glass plate with chrome patterns made by e-beam lithography or projection printing. The areas on the glass without chrome pattern are transparent to UV light, whereas the areas with chrome patterns do not allow light to travel through, thus work as the mask.

The fabrication steps for this MEMS gyroscope are simple, and only three photolithography masks are needed. Figure 6.9 shows the photolithography masks designed for positive photoresist material. Figure 6.10 shows the photolithography masks designed for negative photoresist material. These figures are drawn in Mentor Graphics, the dark area is glass, and the area in red color is the chrome pattern.

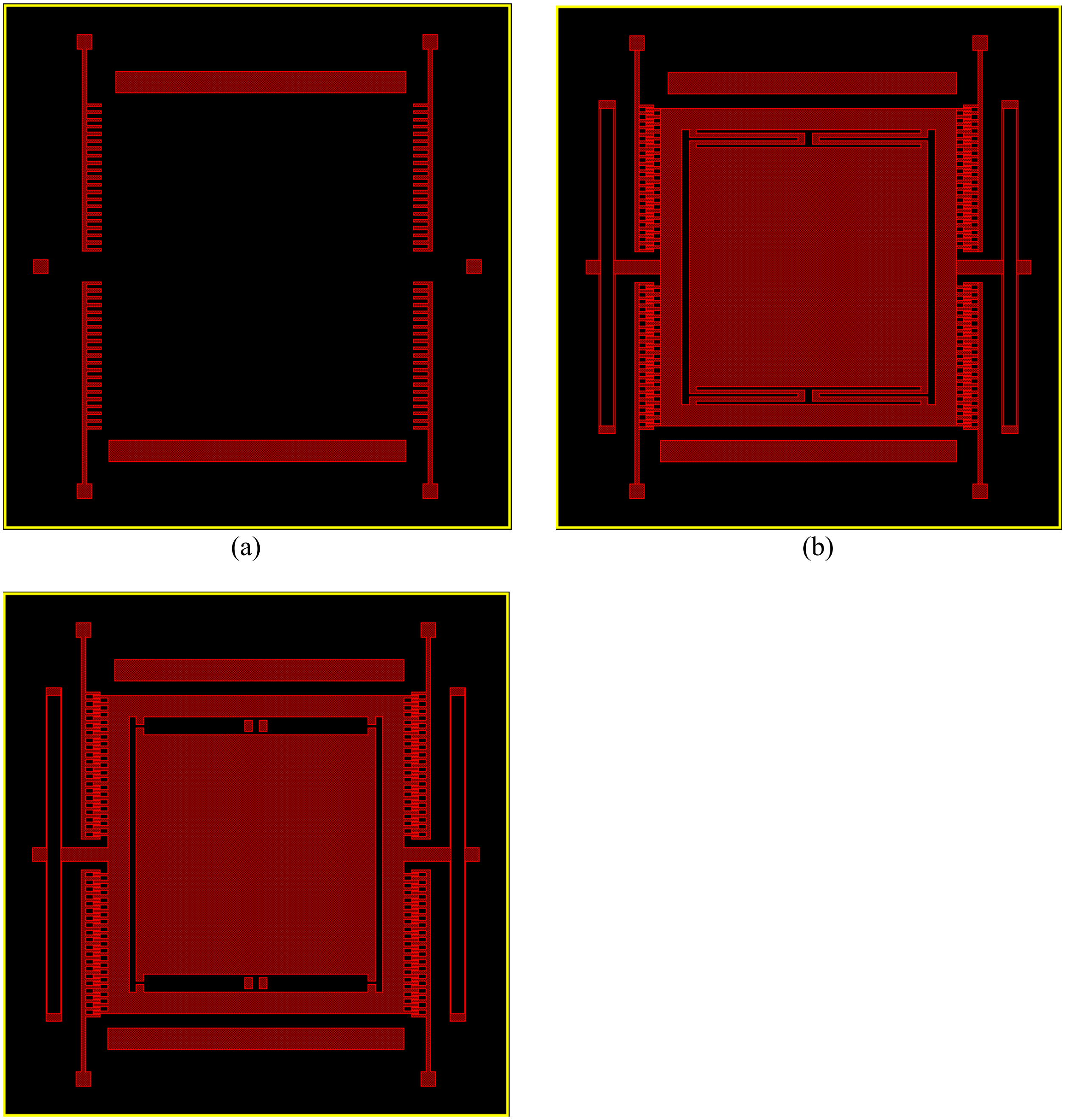

(a) (b)

(c)

Figure 4.9 Photolithography masks designed for positive photoresist material: (a) photolithography mask to etch down the gap between the movable mass and the substrate; (b) photolithography mask to etch down the gap difference between the sensing beam area and the etched-through area; (c) photolithography mask to etch through the device gap area.

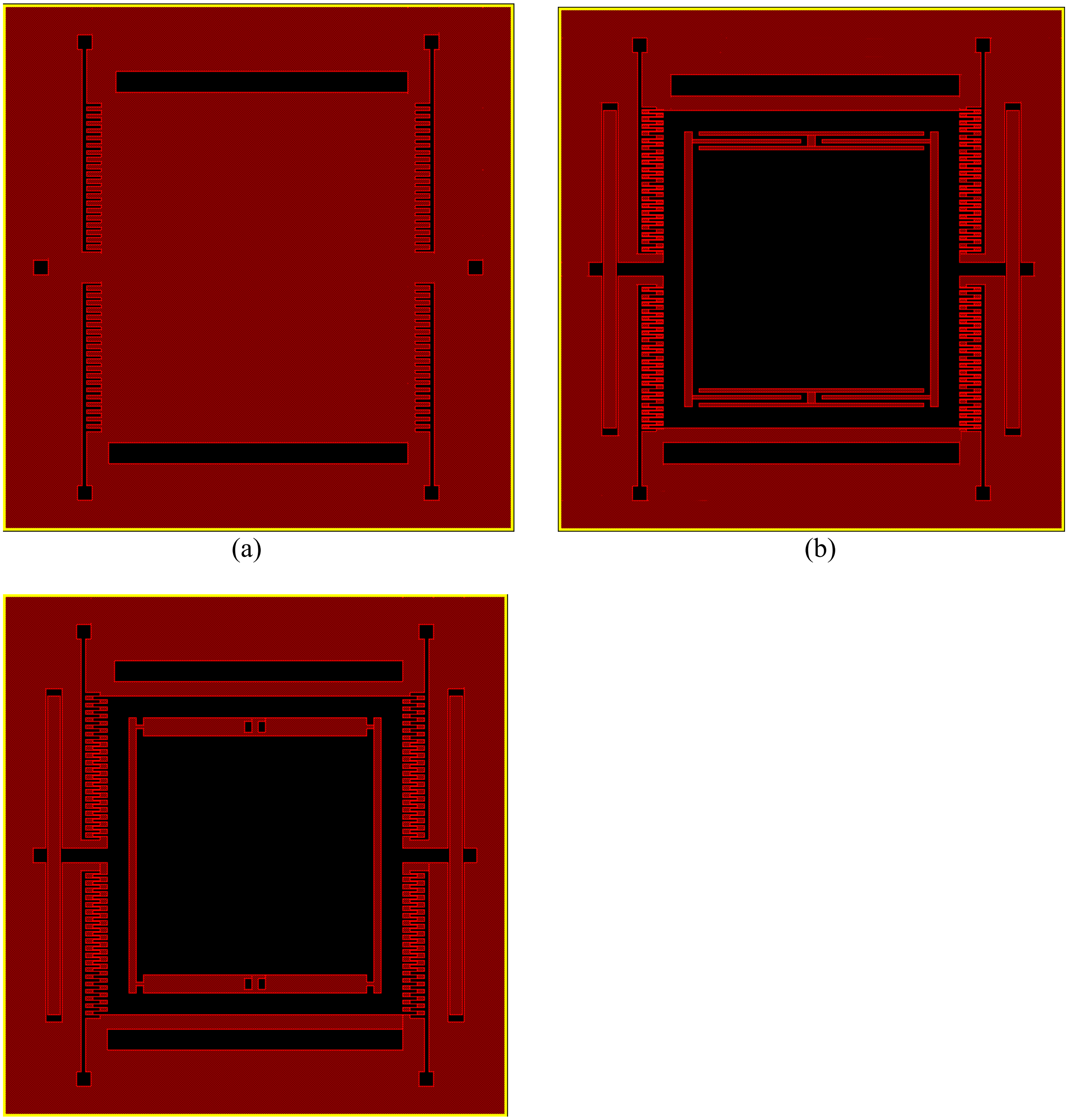

(a)

(b)

(c)

Figure 4.10 Photolithography masks designed for negative photoresist material: (a) photolithography mask to etch down the gap between the movable mass and the substrate; (b) photolithography mask to etch down the gap difference between the sensing beam area and the etched-through area; (c) photolithography mask to etch through the device gap area.

CHAPTER VII. CONCLUSIONS AND FUTURE WORK

In this research, we focus on the MEMS gyroscopes study. Working principle and design strategy of MEMS gyroscopes are introduced. Several available MEMS gyroscopes are analyzed from performance point of view. Based upon the analysis, a novel bulk-micromachined comb vibratory gyroscope design is proposed. The gyroscope uses electrostatic comb driving and differential capacitance sensing. The device is based on a silicon-on-glass structure. DRIE technique is used to increase the device thickness to 100um. The working principle and performance of the microgyroscope are analyzed in detail. Based upon the analysis, an optimized microgyroscope design is proposed. Simulation results demonstrate the gyroscope has the resonant frequency of 617.37Hz and 675.46Hz in driving and sensing mode. Theoretical calculation shows that the device has the displacement sensitivity of 105.9nm/(°/sec) and capacitance sensitivity of 13.88fF/(°/sec). The microgyroscope is very attractive for its good performance and ease for fabrication.

My work in this research can be summarized as:

- Design the structure of a novel vibratory MEMS gyroscope based on a detailed analysis of previous works.
- Solve differential motion equations of the gyroscope and find the expressions for device displacement in two directions.
- Analyze the performance parameters of the gyroscope in MathCAD and draw different curves, for example, resonant frequency vs. beam size, displacement sensitivity vs. beam size, sensitivity vs. frequency mismatch, capacitance change vs. angular velocity, etc.
- Derive a set of optimized design parameters of the gyroscope according to results of the dynamic analysis.
- Simulate the device in ANSYS software for some important design parameters, such as resonant frequency, displacement sensitivity and stress distribution, and compare them with theoretical calculation results.
- Design fabrication processes of this gyroscope and draw photolithography masks in Mentor Graphics.

The future work is to simulate the capacitance sensitivity of this microgyroscope in ANSYS software using electrostatic field coupling analysis, and see how it is matched with the theoretical calculation. Also, we will try to further improve the performance of this proposed microgyroscope by using novel design structure (e.g. four-fold beams). We will look into how to achieve optimized design with these design improvements.

REFERENCES

[1] URL: http://www.spectrum.ieee.org/

[2] URL: http://www.isuppli.com/

[3] URL: http://www.i-micronews.com/

[4] N. Maluf and K. Williams, "An Introduction to Microelectromechanical Systems Engineering", 2nd ed., *Artech House, Inc.*, Norwood, MA, 2004, pp.104-114.

[5] C. Emiliani, "The Scientific Companion", 2nd ed., *Wiley*, NY, 1995, pp.204-205,.

[6] F. Beer, and E. Johnston, Jr., "Vector Mechanics for Engineers: Dynamics", 3rd ed., *McGraw_Hill*, NY, 1977, pp.716-719.

[7] J. Söderkvist, "Micromachined Gyroscopes", *Sensors & Actuators*, Vol. A43, 1994, pp.65-71.

[8] S. Chang, et al., "An Electroformed CMOS Integrated Angular Rate Sensor", *Sensors & Actuators*, Vol. A66, 1998, pp.138-143.

[9] R. Langdon, "The Vibrating Cylinder Gyroscope", *The Marconi Review*, Fourth Quarter, 1982, pp.231-249.

[10] R. Voss, et al., "Silicon Angular Rate Sensor for Automotive Applications with Piezoelectric Drive and Piezoresistive Read-Out", *Proc. 1997 Int. Conf. on Solid-State Sensors and Actuators*, Chicago, IL, 1997, Vol. 2, pp.879-882.

[11] M. Lutz, et al., "A Precision Yaw Rate Sensor in Silicon Micromachining", *Proc. 1997 Int. Conf. on Solid-State Sensors and Actuators,* Chicago, IL, 1997, Vol. 2, pp.847-850.

[12] S. Beeby, G. Ensell, M. Kraft and N. White, "MEMS Mechanical Sensors", *Artech House, Inc.*, Norwood, MA, 2004, pp.195-206.

[13] S. Nasiri, "A Critical Review of MEMS Gyroscopes Technology and Commercialization Status", *Inven. Sense*, CA, 2005.

[14] K. Tanaka, Y. Mochida, M. Sugimoto, K. Moriya, T. Hasegawa, K. Atsuchi and K. Ohwada, "A Micromachined Vibrating Gyroscope", *Sensors & Actuators A: physical*, Vol. 50, 1995, pp.111-115.

[15] Y. Oh, B. Lee, S. Baek, H. Kim, J. Kim, S. Kang, C. Song, "A Tunable Vibratory Microgyroscope", *Sensors & Actuators A: physical*, Vol. 64, 1998, pp.51-56.

[16] X. Xiong, D. Lu and W. Wang, "A Bulk-micromachined Comb Vibrating Microgyroscope Design", *the 48th IEEE International Midwest Symposium on Circuits & Systems*, Vol.1, Cincinnati, Ohio, USA, Aug 7-10, 2005, pp. 151-154.

[17] Y. Liang, T. Zhao, Y. Xu and S. Boh, "A CMOS Fully-integrated Low-voltage Vibratory Microgyroscope", *IEEE Region 10 International Conference on Electrical and Electronic Technology*, Vol. 2, 2001, pp.825-828.

[18] B. Yeh and Y. Liang, "Modeling and Compensation of Quadrature Error for Silicon MEMS Microgyroscope", *the 4th IEEE International Conference on Power Electronics and Drive Systems*, Vol. 2, 2001, pp.871-876.

[19] Y. Mochida, M. Tamura and K. Ohwada, "A Micromachined Vibrating Rate Gyroscope with independent beams for the drive and detection modes", *Sensors & Actuators A: physical*, Vol. 80, 2000, pp.170-178.

[20] S. Bhave, J. Seeger, X, Jiang, B. Boser, B. Roger, T. Howe and J. Yasaitis, "An Integrated, Vertical-drive, In-plane-sense Microgyroscope", *the 12th International Conference on Transducers, Solid-state Sensors, Actuators and Microsystems*, Vol. 1, 2003, pp.171-174.

[21] H. Song, Y. Oh, I. Song, S. Kang, S. Choi, H. Kim, B. Ha, S. Baek and C. Song, "Wafer Level Vacuum Packaged De-coupled Vertical Gyroscope by a New Fabrication Process", *the 15th Annual International Conference on Micro Electro Mechanical Systems*, 2000, pp.520-524.

[22] J. Bernstein, S. Cho, A. King, A. Kourepenis, P. Maciel, and M. Weinberg, "A micromachined comb-drive tuning fork gyroscope", *Proceedings of IEEE on Micro Electro Mechanical Systems*, *(MEMS'93),* Feb. 7-10, 1993, FL, USA, pp. 143-148.

[23] H. Xie and G. Fedder, "Fabrication, Characterization, and Analysis of a DRIE CMOS-MEMS Gyroscope," *IEEE Sensors Journal,* Vol. 3, No. 5, Oct. 2003, pp. 622-631.

[24] W. Clark, R. Howe, and R. Horowitz, "Surface Micromachined Z-axis Vibratory Rate Gyroscope", *IEEE Proceedings on Solid-state Sensors and Actuators,* Hilton Head Island, SC, USA, Jun. 2-6, 1996, pp. 283-287.

[25] B. Xiong, L. Che, and Y. Wang, "A Novel Bulk Micromachined Gyroscope with Slots Structure Working at Atmosphere," *Sensors and Actuators A: Physical,* Vol. 107, 2003, pp. 137-145.

[26] K. Maenaka, Y. Konishi, T. Fujita, M. Maeda, "Analysis and Design Concept Of Highly Sensitive Silicon Gyroscope", *The 8th International Conference on Solid-State Sensors*

and Actuators, 1995 and Eurosensors IX. Transducers '95, Vol. 2, June 25-29, 1995, pp. 612-615.

[27] Maenaka, T. Fujita, Y. Konish, and M. Maeda, "Analysis of Highly Sensitive Silicon Gyroscope with Cantilever Beam as Vibrating Mass," *Sensors and Actuators A: Physical,* Vol. 54, 1996, pp.568-573.

[28] K. Park, C. Lee, Y. Oh, and Y. Cho, "Laterally Oscillated and Force-balanced Micro Vibratory Rate Gyroscope Supported by Fish-hook-shaped Springs", *Sensors and Actuators A: Physical,* Vol. 64, 1998, pp.69-76.

[29] A. Sharma, F. Zaman, B. Amini and F. Ayazi, "A High-Q In-Plane SOI Tuning Fork Gyroscope", Proceedings of IEEE Volume , Sensors, Vol.1 Oct. 24-27, 2004 PP. 467-470.

[30] M. Bao, "Analysis and Design Principles of MEMS Devices", *Elsevier Inc.*, San Diego, CA, USA, 2005.

[31] URL: http://www.ansys.com

[32] M. Lishchynska, N. Cordero, O. Slattery and C. O'Mahony, "Spring Constant Models for Analysis and Design of MEMS Plates on Straight or Meander Tethers", *Sensor Letters*, Vol. 4, 2006, pp.200-205.

[33] R. Jaeger, "Introduction to Microelectronic Fabrication", *Prentice Hall*, New Jersey, 2002, pp. 17-38.

[34] K. Sharma, I. Macwan, L. Zhang, L. Hmurcik, X. Xiong, "Design Optimization of MEMS Comb Accelerometer", *American Society for Engineering Education Zone 1 Conference*, Mar. 28-29, 2008, West Point, NY.

[35] H. Dong, X. Xiong, "Design and Analysis of a MEMS Comb Vibratory Gyroscope", *American Society for Engineering Education Northeast Conference*, Apr. 3-4, 2009, Bridgeport, CT.

VITA

Haifeng Dong was born on January 4, 1983 in Datong, Shanxi, China. He attended high school in Datong, where he grew up. He received his Bachelor of Science degree in Electrics and Information Engineering at Tongji University in Shanghai, China in 2005. From 2006, Haifeng has been studying for his Master of Science degree at University of Bridgeport, CT. His research interest is in MEMS and VLSI circuit design.

During his graduate work at University of Bridgeport, Haifeng has served as a Teaching Assistant in the Department of Electrical Engineering, working on a number of classes related to MEMS and Digital Signal Processing. He also attended ASEE (American Society for Engineering Education) Conference in April 2008 and was selected as the third place winner in poster competition.